
Electronic Thesis and Dissertation Repository

10-10-2019 10:30 AM

Modal Analysis And Analytical Modeling Of Tornado-Like Vortices

Mohammad Karami, *The University of Western Ontario*

Supervisor: Dr. Hangan, Horia, *The University of Western Ontario*

A thesis submitted in partial fulfillment of the requirements for the Doctor of Philosophy degree in Civil and Environmental Engineering

© Mohammad Karami 2019

Follow this and additional works at: <https://ir.lib.uwo.ca/etd>



Part of the [Aerodynamics and Fluid Mechanics Commons](#), and the [Environmental Engineering Commons](#)

Recommended Citation

Karami, Mohammad, "Modal Analysis And Analytical Modeling Of Tornado-Like Vortices" (2019).
Electronic Thesis and Dissertation Repository. 6591.
<https://ir.lib.uwo.ca/etd/6591>

This Dissertation/Thesis is brought to you for free and open access by Scholarship@Western. It has been accepted for inclusion in Electronic Thesis and Dissertation Repository by an authorized administrator of Scholarship@Western. For more information, please contact wlsadmin@uwo.ca.

Abstract

Regardless of the type of vortex chamber, many tornado simulators generate flows that reveal similar flow patterns and a general agreement on the variations of the flow structures with swirl ratio (the ratio of tangential velocity to radial velocity) was achieved. However, very little is known about the underlying physics of the flow, mostly of the fluctuating one, as the previous studies have mainly focused on qualitative flow visualization and the quantitative description of the mean flow.

Herein, coherent structures in tornado-like vortices are extracted using modal decomposition techniques. Modal analysis helps us to better understand the complex vortex dynamics including vortex wandering, vortex breakdown and sub-vortex dynamics. Proper orthogonal decomposition (POD) is applied on the fluctuating velocity field to investigate the prominent mechanisms for a range of swirl ratios ($0.22 \leq S \leq 0.96$). Moreover, another technique dynamic POD is used to provide the time evolutions of coherent structures. Based on the results of the fluctuating velocity field, the three-dimensional vortex structure is revealed.

Despite the accepted measurement techniques for surface pressure, the choice of processing tools for interpretation of the data is challenging. Here, a comparison between some common statistical techniques and modal analysis is provided. Since POD method sometimes results in non-physical modes, another technique, called independent component analysis (ICA), is used. Based on the results of surface pressure fluctuations, statistical properties of coherent structures in tornado-like vortices, including their spectral characteristics, are provided. The discussions of modal analysis presented here is applicable to a large class of swirling flows, regardless of the reference to tornado-like vortices.

By identifying a reduced number of modes representative of tornado-like turbulent velocity field, one can construct simplified but physically meaningful analytical models. Here, both mean and, for the first time, the fluctuating flow fields are analytically modeled. The mean flow field is modeled using a combination of Burgers-Rott model and stagnation flow. The fluctuations attributed to random motion of the vortex (wandering phenomenon) are modeled by solving

deconvolution integral through assuming a Gaussian PDF for wandering motions, and the fluctuations attributed to sub-vortex dynamics are modeled using POD.

Keywords

Tornado-like vortex, coherent structures, modal analysis, proper orthogonal decomposition (POD), independent component analysis (ICA), analytical modeling

Summary for Lay Audience

Due to the increase in tornado wind damage during the last decades, the research related to tornado-like vortices have become a major subject in wind engineering society. While tornadoes can produce extreme wind speeds, the associated extreme destructions may also be linked by factors other than wind speed alone. Thus, there is strong motivation to understand the associated vortex dynamics which may be responsible for extreme negative pressures and therefore damage.

Analytical models derive the variations of wind speed across the tornado path which is a key factor in risk analysis. However, due to the complexities involved in the governing equations, there are very few analytical models for tornado vortices. Moreover, no analytical model considers the fluctuating flow field in tornado vortices.

Large-scale fluctuation in tornado-like vortices are attributed to well-correlated regions, referred to as coherent structures. The choice of mathematical tools for detection and extraction of the coherent structures is a challenging task. These mathematical tools are based on statistical properties and modal analysis.

Herein, we first used four different modal decomposition techniques to extract the coherent structures in tornado-like vortices. The coherent structures help us to better understand the associated vortex dynamics which might be responsible for structural damages. Statistical properties of these coherent structures are also provided. Finally, we provided an analytical model which implements both mean and fluctuating flow fields in tornado vortices.

Co-Authorship Statement

Chapter 2 is a journal article published in the journal of Physics of Fluids. It is co-authored by M. Karami, H. Hangan, L. Carassale and H. Peerhossaini.

Chapter 3 is a journal article and will be submitted for publication under the co-authorship of M. Karami, L. Carassale and H. Hangan.

Chapter 4 is a journal article submitted to Journal of Wind Engineering and Industrial Aerodynamics. It is co-authored by M. Karami and H. Hangan.

Acknowledgement

I want to begin by expressing my sincere appreciation to Dr. Horia Hangan for his excellent supervision and feedback during the last four years. He gave me the time, resources and freedom to grow as a researcher. This work would not have been possible without his priceless guidance.

I would like to extend my thanks to co-authors on my publications: Dr. Luigi Carassale and Dr. Hassan Peerhossaini. Thank you for helping me during my research and providing invaluable feedback on my manuscripts.

I am also grateful to Dr. Hassan Peerhossaini, Dr. Mojtaba Jarrahi as well as Dr. Ebrahim Shirani for recommending me to my supervisor Dr. Horia Hangan.

I would like to also thank Dr. Jubayer Chowdhury and Dr. Djordje Romanic as well as Adrian Costache, Gerry Dafoe and Priscilla De Luca at the WindEEE Research Institute.

My officemates and friends have also been amazing during my PhD. Special thanks to Mahdi, Nima, Mostafa, Arash, Hessam, Junayed, Anant, Mahbub, Aya, Marilena, Daniel and Kamran.

At last but not the least, I would like to thank my family: my parents (Fereshteh and Abdolhassan), my wife (Zahra Habibi), and my sisters (Narges and Nastaran), for all their love and support.

Table of Contents

Abstract	i
Summary for Lay Audience	iii
Co-Authorship Statement.....	iv
Acknowledgement	v
Table of Contents	vi
List of Tables	viii
List of Figures	ix
1 Introduction.....	1
1.1 General introduction.....	1
1.2 Motivation and objectives	3
1.3 Organization of the thesis.....	6
2 Coherent structures in tornado-like vortices	10
2.1 Introduction	10
2.2 Experimental setup.....	13
2.3 Modal representation.....	15
2.4 Analysis of a simulated synthetic vortex	19
2.5 Analysis of experimental flow field.....	26
2.6 Summary and tornado-like vortex structure.....	37
2.7 Conclusions	41
3 Statistical and modal analysis of surface pressure fluctuations in tornado-like vortices	46
3.1 Introduction	46
3.2 Experimental setup.....	49

3.3	Mathematical description of modal decomposition techniques	51
3.4	Modal representation of a simulated synthetic vortex	54
3.5	Analysis of experimental flow field.....	57
3.6	Concluding remarks	72
4	Analytical model for tornado-like vortices: mean and fluctuating flow fields	77
4.1	Introduction	77
4.2	Experimental setup of Mini-WindEEE Dome	78
4.3	Analytical model for the vortex flow	80
4.4	Results and comparisons	89
4.5	Concluding remarks	96
5	Conclusions and recommendations.....	99
5.1	Summary	99
5.2	Conclusions.....	100
5.3	Recommendation and future work.....	103
	Appendix A.....	105
	Curriculum Vitae	107

List of Tables

Table 1. 1. Six categories of Fujita scale for tornado intensity.....	3
---	---

List of Figures

Figure 1. 1: Locations of tornadoes occurrences in Canada between the years of 1980-2009. Image from [13]. 2

Figure 2. 1: Photograph of tornado-like vortex for (a) small swirl ratio, $S=0.22$, with vortex tilting, (b) moderate swirl ratio, $S=0.57$, with recirculation bubble of vortex breakdown and (c) a single spiral developed behind the bubble, and (d) high swirl ratio, $S=0.96$, with double spiral developed behind the bubble. Double spiral pattern refers also to as double-cell structure. Reproduced with permission from J. Atmos. Sci. (1979)[32]. Copyright 1979 American Meteorological Society. 11

Figure 2. 2: Schematic drawing of Mini-WindEEE Dome. © Elsevier. Used with permission from Ref. [25]. 13

Figure 2. 3: A snapshot of the vorticity field of the idealized (synthetic) vortex (a) with Gaussian random wandering and/or variation in size, (b) with a single spiral rotating around the vortex and (c) with a double spiral rotating around the vortex..... 20

Figure 2. 4: Time history of fluctuating vorticity field of the simulated vortex with only Gaussian random wandering. Positive (negative) values of vorticity are shown in red (blue) color. 20

Figure 2. 5: The first five POD modes of the idealized (synthetic) vortex with only Gaussian random wandering. 21

Figure 2. 6: Time history of fluctuating vorticity field of the simulated vortex with Gaussian random wandering plus a size variation. Positive (negative) values of vorticity are shown in red (blue) color..... 22

Figure 2. 7: The first five POD modes of the idealized (synthetic) vortex with Gaussian random wandering and variation in size. 22

Figure 2. 8: Time history of the vorticity field of (a) single and (b) double spiral rotating around the vortex. 24

Figure 2. 9: The first two POD modes of the idealized (synthetic vortex) with (a) single and (b) double spiral rotating around the vortex (see Figures 3-b and 3-c). 25

Figure 2. 10: Energy of POD modes of the idealized (synthetic) vortex with four different simulation cases: (I) vortex with only wandering, (II) vortex with wandering plus size variation, (III) vortex with single spiral and (IV) vortex with double spiral. 25

Figure 2. 11: Time histories of experimental vorticity fields at height of 3.5 cm above the surface for (a) $S = 0.22$, (b) $S = 0.57$, and (c) $S = 0.96$. (Time step size is 0.067 s). 27

Figure 2. 12: Mean tangential velocity (m/s) contours for $S = 0.22$ at different heights for (a) un-removed wandering and (b) removed wandering. 28

Figure 2. 13: Mean radial velocity (m/s) contours for $S = 0.22$ at different heights for (a) un-removed wandering and (b) removed wandering. Convergent and divergent radial flow are shown respectively in blue and red colors. 29

Figure 2. 14: Mean tangential velocity (m/s) contours for $S = 0.57$ at different heights for (a) un-removed wandering and (b) removed wandering. 30

Figure 2. 15: Mean radial velocity (m/s) contours for $S = 0.57$ at different heights for (a) un-removed wandering and (b) removed wandering. Convergent and divergent radial flow are shown respectively in blue and red colors. 31

Figure 2. 16: Mean tangential velocity (m/s) contours for $S = 0.96$ at different heights for (a) un-removed wandering and (b) removed wandering. 31

Figure 2. 17: Mean radial velocity (m/s) contours for $S = 0.96$ at different heights for (a) un-removed wandering and (b) removed wandering. Convergent and divergent radial flow are shown respectively in blue and red colors. 32

Figure 2. 18: First five POD modes of the vorticity field with un-removed wandering for $S = 0.22$ at $h = 3.5$ cm. Positive (negative) values of vorticity are shown in red (blue) color. 33

Figure 2. 19: D-POD mode 1 with un-removed wandering, for $S = 0.22$ and $h = 3.5$ cm at six different phase shifts (α), representing time-lag. Positive (negative) values of vorticity are shown in red (blue) color. 34

Figure 2. 20: First five POD modes of vorticity field with un-removed wandering for $S = 0.57$ at $h = 3.5$ cm. Positive (negative) values of vorticity are shown in red (blue) color. 34

Figure 2. 21: D-POD mode 3, with un-removed wandering, for $S = 0.57$ and $h = 3.5\text{ cm}$ at six different phase shifts (α), representing time-lag. Positive (negative) values of vorticity are shown in red (blue) color..... 35

Figure 2. 22: First five POD modes of vorticity field with un-removed wandering for $S = 0.96$ at $h = 3.5\text{ cm}$. Positive (negative) values of vorticity are shown in red (blue) color. 36

Figure 2. 23: The first POD mode of the vorticity field with removed wandering effects at $h = 3.5\text{ cm}$ for (a) $S = 0.22$ and (b) $S = 0.57$. Positive (negative) values of vorticity are shown in red (blue) color..... 36

Figure 2. 24: Streamlines in a snapshot of the horizontal PIV plane at $h = 3.5\text{ cm}$ for revealing (a) single-cell structure for $S = 0.22$, (b) double-cell structure for $S = 0.57$, and (c) double-cell structure for $S = 0.96$. Note that double-cell structure includes two co-rotating sub-vortices that are embedded in the fluctuating flow field. 39

Figure 2. 25: First POD mode of vorticity field with un-removed wandering at the different heights for (a) $S = 0.22$, (b) $S = 0.57$ and (c) $S = 0.96$. Positive (negative) values of vorticity are shown in red (blue) color..... 40

Figure 2. 26: Time-frequency analysis (spectrogram) of the first POD mode of the surface pressure fluctuation for (a) $S = 0.22$, (b) $S = 0.57$ and (c) $S = 0.96$ 40

Figure 2. 27: Schematic of the mean flow observed for the three swirl ratios (a) $S = 0.22$, (b) $S = 0.57$ and (c) $S = 0.96$ 40

Figure 2. 28: Three-dimensional schematic of coherent structures inferred from modal analysis. (a) For $S = 0.22$, a single vortex with tilting at low heights (this structure refers to as single-cell), (b) for $S = 0.57$, a recirculation bubble (shown in yellow) with a single spiral behind the bubble, which still refers to as single-cell structure, and (c) for $S = 0.96$, a recirculation bubble with a double spiral behind the bubble, referring to as two-cell structure..... 41

Figure 3. 1: (a) Schematic drawing of Mini-WindEEE Dome (MWD) and (b) schematic of pressure taps arrangement over the surface panel. Obtained from Ref. [29]. 49

Figure 3. 2: A bivariate Gaussian synthetic vortex with variation in size and random wandering around the geometric center..... 54

Figure 3. 3: The first five POD modes of the idealized (synthetic) vortex with Gaussian random wandering motion.	55
Figure 3. 4: The ICA modes extracted from the data space defined from the first six POD modes applied on the synthetic vortex. Positive (negative) values of pressure are shown in red (blue).	55
Figure 3. 5: Time history of fluctuating pressure field of the simulated vortex with Gaussian random wandering plus a size variation. Positive (negative) values of pressure are shown in red (blue) color.	56
Figure 3. 6: The first five POD modes of the idealized (synthetic) vortex with Gaussian random wandering motion.	56
Figure 3. 7: Streamlines in two different snapshots of horizontal PIV plane for $S = 0.96$ revealing the presence of both (a) single-cell structure and (b) double-cell structure. Obtained from Ref. [36].	57
Figure 3. 8: (a) Mean and (b) standard deviation of surface pressure field. Wandering effects are not removed.	58
Figure 3. 9: Radial profile of mean surface pressure deficit for removed (corrected) and un-removed (uncorrected) wandering effects, (a) $S = 0.22$, (b) $S = 0.57$ and (c) $S = 0.96$. Radius (r) is normalized with updraft radius.	59
Figure 3. 10: Power spectral density along the radius for (a) $S = 0.22$, (b) $S = 0.57$ and (c) $S = 0.96$. Wandering effects are not removed. r is normalized with updraft radius. Note that the core radius (rc) for the three swirl ratios (a-c) are respectively $rc = 0.14, 0.32$, and 0.45	60
Figure 3. 11: Cumulated energy of POD modes.	61
Figure 3. 12: The first five POD modes of surface pressure for $S = 0.22$. Positive (negative) values of surface pressure are shown in red (blue). Wandering effects are not removed.	63
Figure 3. 13: ICA modes extracted from the data space defined from the first five POD modes for $S = 0.22$. Positive (negative) values of surface pressure are shown in red (blue). Wandering effects are not removed.	63
Figure 3. 14: Power spectral density of (a) PCs and (b) ICs for $S = 0.22$	64

Figure 3. 15: (a) Absolute value of the coherence, and (b) phase angle of coherence of PCs for $S = 0.22$.	64
Figure 3. 16: D-ICA \mathbf{a}_2 for $S = 0.22$ at $f_c = 3.3 \text{ Hz}$ with $\Delta f = 2.9 \text{ Hz}$ at six different phase shifts (α). Positive (negative) values of surface pressure are shown in red (blue). The Figure scale is doubled. Wandering effects are not removed.	65
Figure 3. 17: The first five POD modes of surface pressure for $S = 0.57$. Negative (positive) values of surface pressure are shown in red (blue). Wandering effects are not removed.	65
Figure 3. 18: ICA modes extracted from the data space defined from the first five POD modes for $S = 0.57$. Positive (negative) values of surface pressure are shown in red (blue). Wandering effects are not removed.	66
Figure 3. 19: D-ICA (a) \mathbf{a}_1 and (b) \mathbf{a}_2 for $S = 0.57$ at $f_c = 3.3 \text{ Hz}$ with $\Delta f = 2.9 \text{ Hz}$ at six different phase shifts (α). Positive (negative) values of surface pressure are shown in red (blue). Wandering effects are not removed.	67
Figure 3. 20: Power spectral density of (a) PCs and (b) ICs for $S = 0.57$.	69
Figure 3. 21: (a) Absolute value of the coherence, and (b) phase angle of coherence of PCs for $S = 0.57$.	69
Figure 3. 22: The first five POD modes for $S = 0.96$. Positive (negative) values of surface pressure are shown in red (blue). Wandering effects are not removed.	71
Figure 3. 23: ICA modes extracted from the data space defined from the first seven POD modes for $S = 0.96$. Positive (negative) values of surface pressure are shown in red (blue). Wandering effects are not removed.	71
Figure 3. 24: Power spectral density of (a) PCs and (b) ICs for $S = 0.96$.	72
Figure 3. 25: (a) Absolute value of the coherence, and (b) phase angle of coherence of PCs for $S = 0.96$.	72
Figure 4. 1: Schematic drawing of WindEEE Dome [12].	79

Figure 4. 2: Schematic representation of vorticity field of coherent structures. (a) $S = 0.22$, a single vortex subjected to random wandering motion. (b) $S = 0.57$, a recirculation bubble vortex at the center and a spiral vortex rotating around the bubble. (c) $S = 0.96$, a recirculation bubble vortex at the center and a double spiral vortex rotating around the bubble. 86

Figure 4. 3: The energy of POD modes for the three swirl ratios of MWD experiment. Wandering is included. 86

Figure 4. 4: Mean tangential velocity profile of MWD experiment for removed (corrected) and un-removed (uncorrected) wandering effects, (a) $S = 0.22$, (b) $S = 0.57$ and (c) $S = 0.96$ 90

Figure 4. 5: The radial profile of normalized tangential velocity and its comparison with existing models for (a) $S = 0.22$ at $z = rc$, (b) $S = 0.57$ at $z = 0.6 rc$, and (c) $S = 0.96$ at $z = 0.4 rc$ 92

Figure 4. 6: The vertical profile of normalized tangential velocity and its comparison with existing models at $r = rc$ for (a) $S = 0.22$, (b) $S = 0.57$, and (c) $S = 0.96$ 93

Figure 4. 7: The radial (a-b) and vertical (c-d) profiles of normalized radial and axial velocity components and their comparison with existing models for $S = 0.22$ ($z = rc$ and $r = rc$). 94

Figure 4. 8: The radial and vertical profiles of mean radial and axial velocity components (Eqs. 4.3 and 4.4) at $r = rc$ for (a) $S = 0.57$ at $z = 0.6 rc$, and (b) $S = 0.96$ at $z = 0.4 rc$ 95

Figure 4. 9: Radial profile of the fluctuating tangential velocity based on wandering motion and its comparison with MWD experiment at $z = rc$ for $S = 0.22$ 96

Figure 4. 10: Radial profile of the fluctuating tangential velocity based on sub-vortex dynamics and its comparison with MWD experiment for (a) $S = 0.57$ at $z = 0.6 rc$ and (b) $S = 0.96$ at $z = 0.4 rc$ 96

Chapter 1

1 Introduction

1.1 General introduction

Tornadoes are referred to as a violent rotating column of air which is in contact with both ground and cloud. They can last for hours and produce wind speeds more than 100 m/s close to the earth surface, and thus are a serious threat to many regions around the world. For instance, tornadoes resulted in about 10 billion dollars damage in the United States in 2011 [1].

Over half of tornadoes have peak wind speeds smaller than 165 km/hr and over 80% of tornadoes have peak wind speeds of smaller than 217 km/hr [2]. This means that, although severe tornadoes produce extreme wind speeds, the associated extreme destructions may also be linked by factors other than wind speed alone. Thus, there is strong motivation to (i) understand the associated vortex dynamics which may be responsible for extreme negative pressures and therefore damage and (ii) to create a wind field model which would be a key factor in risk analysis application [3-4]. These are the two main objectives of the present thesis.

However, due to the complexities involved in the governing equations, there are very few analytical models for tornado vortices. Moreover, no analytical model considers the fluctuating flow field in tornado vortices.

Large-scale fluctuation in tornado-like vortices are attributed to well-correlated regions, referred to as coherent structures. The concept of coherent structures is still not consolidated and development of mathematical tools for their detection and extraction is difficult [5]. These mathematical tools are based on statistical properties and modal analysis. The most popular and probably the oldest technique for modal representation is proper orthogonal decomposition (POD) [6]. Sometimes the results are promising [7-9], but the general opinion is that POD method fails to provide meaningful modes [10-12].

The overall objective of this study is to introduce a new tornado wind field for both mean and fluctuating flow fields of tornado-like vortices based on the modal analysis of tornado vortices

simulated experimentally in a model of WindEEE Dome (MWD). To model the fluctuating field, we first try to characterize the dominant turbulent flow by extracting coherent structures out of both velocity and surface pressure fields. Since there is no general accepted technique for extracting coherent structures, we used four different modal decomposition techniques: proper orthogonal decomposition (POD), independent component analysis (ICA), dynamic POD, and dynamic ICA. A comparison between modal analysis and some common statistical techniques is also provided. Finally, based on these results, the vortex structure is inferred for the range of Swirl ratios ($0.22 \leq S \leq 0.96$). This vortex structure is further employed to generate an analytical model for the large-scale fluctuating flow field in tornado-like vortices. Note that the main governing parameter in simulated tornado-like vortices is the swirl ratio which is defined as the ratio of tangential to radial velocity components at the inlet, $S = (1/2a) (V_{tan}/V_{rad}) = (1/2a) \tan\theta$, where θ is the vane angle with the normal direction to the sidewall.

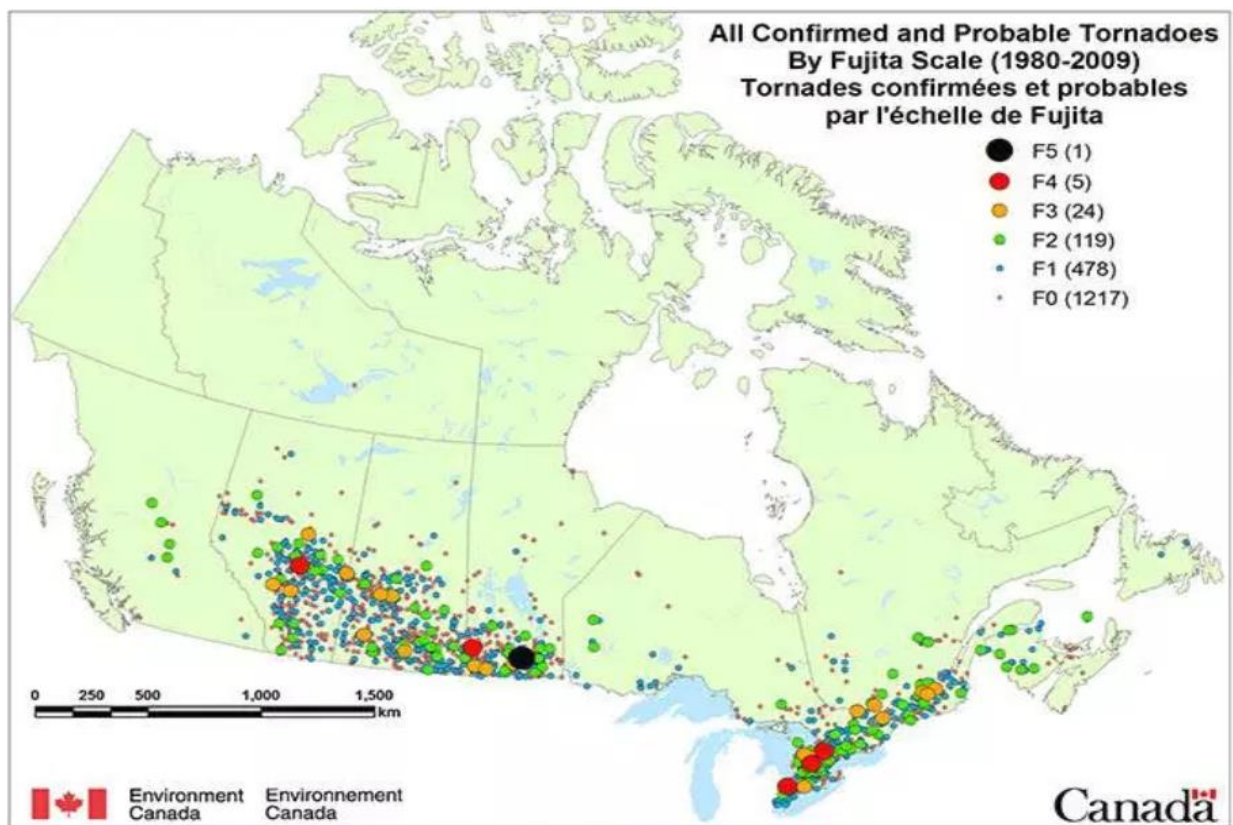


Figure 1. 1: Locations of tornadoes occurrences in Canada between the years of 1980-2009. Image from [13].

1.2 Motivation and objectives

Tornadoes can happen in different regions of the world. In Canada, they mostly occur in southern Ontario, Quebec, Manitoba, Saskatchewan and Alberta. A map of locations of tornadoes occurrences between the years of 1980-2009 is shown in Figure 1.1. [13].

Table 1. 1. Six categories of Fujita scale for tornado intensity.

Scale	Wind speed range(km/hr)	Potential damage
F0	64-116	Light damage, e.g. chimneys and tree branches
F1	117-180	Moderate damage, e.g. peels surface off roofs
F2	181-253	Significant damage, e.g. roofs torn off frame houses
F3	254-332	Severe damage, e.g. roofs/walls torn off houses
F4	333-418	Devastating damage, e.g. well-constructed houses leveled
F5	419-512	Incredible damage, strong frame houses lifted off foundations

Intensity of tornadoes is rated by Fujita scale, which is based on damages of tornadoes on structures or vegetations. The six categories of Fujita scale based on order of intensity is shown in Table 1.1. However, Fujita scale is based on damage and not real wind speed or pressure. Thus, Enhanced Fujita (EF) scale replaced Fujita scale in United States and more recently in Canada [13]. The new scale still uses F0-F5 rating, but it is based on a new wind speed range for each category: 105-137 (km/hr) for EF0, 138-177 (km/hr) for EF1, 178-217 (km/hr) for EF2, 218-266 (km/hr) for EF3, 267-322 (km/hr) for EF4, >322 (km/hr) for EF5.

Most of building structures would not survive these peak winds. Thus, it is often stated that it is not worth to consider tornado wind forces in the building codes as the added cost is not justifiable. However, more than half of tornadoes have maximum wind speed smaller than 165 km/hr and 80% of tornadoes falls in the category EF2 [2-3]. Moreover, the area which is subjected to the peak winds is much smaller than the damage path of tornado [3]. Wind speed changes significantly across tornado damage path. Thus, it is important to have wind characteristics for an accurate

assessment of tornado hazard and have an analytical model which implements both mean and fluctuating flow fields. The fluctuating flow field can be obtained by modal decomposition techniques.

1.2.1 Modal decomposition techniques

Turbulent vortex flows present two types of fluctuations: (i) large-scale fluctuations due to the coherent structures, and (ii) small scale fluctuations. Large-scale fluctuations can be identified and extracted by modal decomposition techniques. Modal representation is an efficient way to express the complex spatial and temporal variations of turbulent flow as a combination of time-invariant distributions, called modes, modulated by scalar coefficients.

The most popular and probably the oldest technique for modal representation is proper orthogonal decomposition (POD), introduced by Lumely [6]. Arndt et. al. [28] applied space time approach to pressure fluctuations surrounding an axisymmetric jet. J. Delville [29] and Ukeiley et. al. [30] initially applied the space time approach to hot wire rake data which was available at only one streamwise location. Then, they used Taylor's Hypothesis to map from frequency domain to the streamwise wavenumber domain and then proceeded to use such eigenfunction in a dynamical system approach. Herein, time stationary form of POD is referred to as Dynamic POD, or Spectral POD. W. K. George [31] provided a comprehensive review on this subject.

POD as a feature-recognition tool sometimes provides non-physical patterns. This failure is mainly attributed to two problems: (i) ranking modes by their own energy might not be relevant in cases where weak or intermittent coherent structures exist [7-9], and (ii) mode shapes are likely to be determined by the orthogonality constraint and thus may not be physically meaningful [5].

Another technique is independent component analysis (ICA) which mitigates the problems of POD method [24-27]. Its main difference with POD is that ICA exploits non-Gaussian structures and make them as independent as possible. Despite its widespread in several fields such as image recognition and signal processing, its application in fluid dynamics research area is very limited and its potentials are still unexplored.

In other words, POD can be seen as a mathematical tool to reveal physical phenomena embedded in data. POD splits the flow into two functions of time and space, and the space function is referred

to as POD modes. To extract physical features, POD maximizes the energy projection of modes. This results in an eigenvalue problem, meaning that POD modes are sorted by their eigenvalue from maximum to minimum. Since eigenvalues can be associated to energy of the flow (turbulent kinetic energy), the first few POD modes have the highest energy. However, POD modes are constraint to orthogonal spaces, which results in non-physical modes. ICA mitigates this condition by searching for independent modes. Both POD and ICA can be applied in frequency domain and provide modes with complex values which helps us to visualize the modes in animation.

The above literature review shows that POD and ICA have not been applied on tornado-like vortices. This flow is complex since different physical phenomena (wandering, vortex breakdown and transition from single-cell to double-cell) can be observed. Here, POD and ICA are used to identify and extract coherent structures out of tornado-like vortices which can be used further to generate an analytical model for the fluctuating flow field.

1.2.2 Analytical models of tornado-like vortices

A brief review of analytical models of tornado vortices is presented herein. A detailed review is presented in Chapter 4.

The most well-known and probably the oldest analytical model is Rankine model in which only the radial variation of tangential velocity component (U_θ) is considered. Note that Rankine model presents in two versions, refers to as combined or modified models, for which modified model gives a smoother variation at the core radius.

Vatistas [14] proposed an empirical model for tangential velocity assuming that tangential velocity is only function of radius and vortex has solid-body rotation at the core. In this model, the radial and vertical components are smaller than the tangential component. While this model works for single-cell vortex, it does not capture the downdraft by the vortex breakdown.

Wood and White [15,16] modified the Vatistas model and proposed a model in which three empirical constants are implemented to control the shape of tangential velocity profile in the core radius and outer core area.

Kuo-Wen [17,18] presented analytical model which considers the effects of boundary layer. In this model, there are two sets of equations for the three velocity components (radial, vertical and

tangential components) for within and out of boundary layer. This is the only model that considers the effects of boundary layer.

Burgers [19] and Rott [20] suggested a model as a solution of Navier-Stokes equations for the three velocity components. In this model, the axial velocity remains constant at the different radial distance from vortex center, which is not realistic.

Xu and Hangan [21] presented a vortex model by combining a jet model with the modified Rankine vortex. In their approach, the jet model characterizes the radial and axial motions, and the Rankine vortex describes the tangential component. They successfully compared the analytical model with experimental data at small values of Swirl ratio ($S = 0.28$).

Recently, Baker and Sterling [22] proposed a vortex model for which the velocity components are normalized by maximum radial velocity $U_{r,max}$. r and z are normalized r_m and z_m as the radius and height for which maximum radial velocity occurs. This model is more suitable for calculating debris trajectory [23].

The above-mentioned literature review on the analytical modeling of tornado vortices shows that no analytical model considers the fluctuating flow fields, despite of its importance in the wind field [23]. Large scale wind fluctuations can be extracted and reconstructed using modal analysis.

1.3 Organization of the thesis

This thesis follows the “integrated article” format as per thesis submission requirement of Western University. The thesis contains three articles described in Chapter 2, Chapter 3 and Chapter 4, respectively.

Chapter 1 provides a brief introduction to tornado research and defines the main objectives of the thesis: (i) the modal decomposition analysis of the velocity and surface pressure fields of experimental tornado vortices and (ii) the definition of a mean and novel fluctuating flow field analytical model for tornado vortices. It also summarises modal analysis techniques applicable to tornado vortices and includes a brief review of related analytical models.

Chapter 2 investigates the coherent structure of the tornado vortices using two different decomposition methods: (i) proper orthogonal decomposition (POD), also referred to as principle

component analysis (PCA) and (ii) dynamic proper orthogonal decomposition (D-POD) to provide time evolutions of the POD modes. To foster the physical interpretation of these POD modes, a modal decomposition on a simulated synthetic vortex is also applied.

Chapter 3 presents statistical analysis of surface pressure fluctuations in tornado-like vortices. A comparison between modal decomposition techniques (POD and ICA) and some common statistical techniques is also provided. This part of the thesis is fundamental in future understanding and modeling of the impact of tornado vortices on buildings and structures.

Chapter 4 provides an analytical model for the velocity field of tornado-like vortices with single-cell and double-cell structures. Both the mean and fluctuating flow fields are considered. The analytical model of fluctuating flow field is entirely novel and based on the results of modal analysis discussed in Chapter 2 and Chapter 3.

Chapter 5 provides a summary of the work and conclusions. This Chapter provides also recommendations for the scope of future work.

References

- [1] M. Refan, H. Hangan, J. Wurman, Reproducing tornadoes in laboratory using proper scaling, *J. Wind Eng. Ind. Aerodyn.* 135(2014)136–148.
- [2] L. A. Twisdale, *Tornado Missile Simulation and Design Methodology*, EPRI NP-2005, Electric Power Research Institute, Palo Alto, Calif., Aug., 1981.
- [3] L. A. Twisdale, W. L. Dunn, Probabilistic analysis of tornado wind risks, *Journal of Structural Engineering*, 109 (1983) 468-488.
- [4] L. A. Twisdale, W. L. Dunn, Wind loading risks from multivortex tornadoes, *Journal of Structural Engineering* 109 (1983) 2016-2022.
- [5] L. Carassale, M. Marre-Brunenghi, Statistical analysis of wind-induced pressure fields: A methodological perspective, *J. Wind Eng. Ind. Aerodyn.* 99 (2011) 700–710.
- [6] J.L., Lumley, *Stochastic Tools in Turbulence*. Academic Press, New York 1970.
- [7] B. Bienkiewicz, Y. Tamura, H.J. Ham, H. Ueda, K. Hibi, Proper orthogonal decomposition and reconstruction of multi-channel roof pressure, *J. Wind Eng. Ind. Aerodyn.* 54-55 (1995) 369-381.

- [8] Y. Tamura, H. Ueda, H. Kikuchi, K. Hibi, S. Suganuma, B. Bienkiewicz, Proper orthogonal decomposition study of approach wind-building pressure correlation, *J. Wind Eng. Ind. Aerodyn.* 72 (1997) 421-432.
- [9] A. Kareem, J.E. Cermak, Pressure fluctuations on a square building model in boundary-layer flows, *J. Wind Eng. Ind. Aerodyn.* 16 (1984) 17-41.
- [10] M. Sieber, C. O. Paschereit, K. Oberleithner, Advanced identification of coherent structures in swirl-stabilized combustors, *J. of Eng. for Gas Turbines and Power* 139 (2017) 021503-1.
- [11] J.D. Holmes, R. Sankaran, K.C.S. Kwok, M.J. Syme, Eigenvector modes of fluctuating pressures on low-rise building models, *J. Wind Eng. Ind. Aerodyn.* 69-71 (1997) 697-707.
- [12] Y. Tamura, S. Suganuma, H. Kikuchi, K. Hibi, Proper orthogonal decomposition of random wind pressure field, *J. Fluids Struct.* 13 (1999) 1069-1095.
- [13] Canada, Government of Canada, Environment and Climate Change. "Environment and Climate Change Canada - Weather and Meteorology - Enhanced Fujita Scale". ec.gc.ca. Retrieved February 9, 2017.
- [14] G. H. Vatistas, V. Kozel, W. C. Mih, A simpler model for concentrated vortices. *Exp. Fluid* 11 (1991) 73–76.
- [15] V. T. Wood, L. W. White, A new parametric model of vortex tangential-wind profiles: development, testing and verification. *J. Atmos. Sci.* 68 (2011) 990–1006.
- [16] V. T. Wood, L. W. White, A parametric wind-pressure relationship for Rankine versus non-Rankine cyclostrophic vortices. *J. Atmos. Ocean. Technol.* 30 (2013) 2850–2867.
- [17] Y. K. Wen, A. H. Ang, 1975, Tornado risk and wind effect on structures. In: *Proceedings of the Fourth International Conference on Wind Effects on Buildings and Structures* (1975) 63–74.
- [18] Y. K. Wen, 1975. Dynamic tornadic wind loads on tall buildings. *J. Struct. Div.* 101 (1975), 169–185.
- [19] J. M. Burgers, A mathematical model illustrating the theory of turbulence. *Adv. Appl. Mech.* 1 (1948) 171–199.
- [20] N. Rott, On the viscous core of a line vortex. *Z. für Angew. Math. Phys.* 9 (1958) 543–553.

- [21] Z. Xu and H. Hangan, An Inviscid Solution for Modeling of Tornado-Like Vortices. *Journal of Applied Mechanics* 76 (2009) 03011-5.
- [22] C. J. Baker and M Sterling, Modelling wind fields and debris flight in tornadoes, *Journal of Wind Engineering and Industrial Aerodynamics* 168 (2017) 312-321.
- [23] Y. C. Kim, M. Mastsui, Analytical and empirical models of tornado vortices: A comparative study, *Journal of Wind Engineering & Industrial Aerodynamics* 171 (2017) 230–247.
- [24] L. Carassale, M. Brunenghi, Identification of meaningful coherent structures in the wind-induced pressure on a prismatic body, *J. Wind Eng. Ind. Aerodyn.* 104–106 (2012) 216–226.
- [25] L. Carassale, Analysis of aerodynamic pressure measurements by dynamic coherent structures, *Probabilistic Engineering Mechanics* 28 (2012) 66–74.
- [26] X. Gilliam, J. P. Dunyak, D. A. Smith, F. Wu, Using projection pursuit and proper orthogonal decomposition to identify independent flow mechanisms. *J. Wind Eng. Ind Aerodyn* 92 (2004) 53–69.
- [27] H. He, D. Ruan, K. C. Metha, X. Gilliam, F. Wu, Nonparametric independent component analysis for detecting pressure fluctuation induced by roof corner vortex. *J Wind Eng. Ind Aerodyn* 95 (2007) 429–43.
- [28] R. E. A. Arndt, D. F. Long, M. N. Glauser, The proper orthogonal decomposition of pressure fluctuations surrounding a turbulent jet, *J. Fluid Mechanics* 340 (1997) 1-33.
- [29] J. Delville, L. Ukeiley, L. Cordier, J. P. Bonnet, M. Glauser, Examination of large-scale structures in a turbulent plane mixing layer. Part 1. Proper orthogonal decomposition, *J. Fluid Mechanics* 391 (1999) 91-122.
- [30] L. Ukeiley, L. Cordier, R. Manceau (a3), J. Dellvile, M. Glauser and J. P. Bonnet, Examination of large-scale structures in a turbulent plane mixing layer. Part 2. Dynamical systems model, *J. Fluid Mechanics* 441 (2001) 67-108.
- [31] W. K. George, A 50-Year Retrospective and the Future. In *Whither Turbulence and Big Data in the 21st century?* Springer (2017) 13-43.

Chapter 2

2 Coherent structures in tornado-like vortices

The dynamics of tornado-like vortices is investigated through a set of novel physical experiments and modal analyses for a wide range of swirl ratios ($0.22 \leq S \leq 0.96$). Various physical phenomena such as wandering, vortex breakdown or transition from one-cell to two-cell structures are observed. To investigate the coherent structure of the tornado vortices, two different decomposition methods are applied: (i) proper orthogonal decomposition (POD), also referred to as principle component analysis (PCA) and (ii) dynamic proper orthogonal decomposition (D-POD) to provide time evolutions of the POD modes. To foster the physical interpretation of these POD modes, we also applied modal decomposition on a simulated synthetic vortex.

The results show that at low swirl ratios before vortex break down, the flow is characterized by a single vortex which is tilted at lower heights. For intermediate swirls, before vortex touch down, the flow is characterized by a recirculation bubble with a single spiral rotating around it. By further increasing the swirl ratio, transition from single spiral to double spiral (one-cell to two-cell structures) occurs. Based on these observations, a simple vortex structure of tornado-like vortex is put forward which can be used to generate a low order, large scale turbulence model for these type of flows.

2.1 Introduction

With the raise in tornado wind damage during the last decades, the research on tornado-like vortices has been revived. While mean flow fields have been put forward, [1-4], there remains a fundamental lack in understanding and experimental modeling of the turbulent flow dynamics. Regardless of the type of vortex chamber, many tornado simulators generate flows that reveal similar flow patterns and agree in general on the variations of the flow structures with swirl ratio (the ratio of tangential velocity to radial velocity) [3]. However, very little is known about the underlying physics of the flow as the previous studies have mainly focused on qualitative flow visualization and the quantitative description of the mean flow and some statistical turbulence

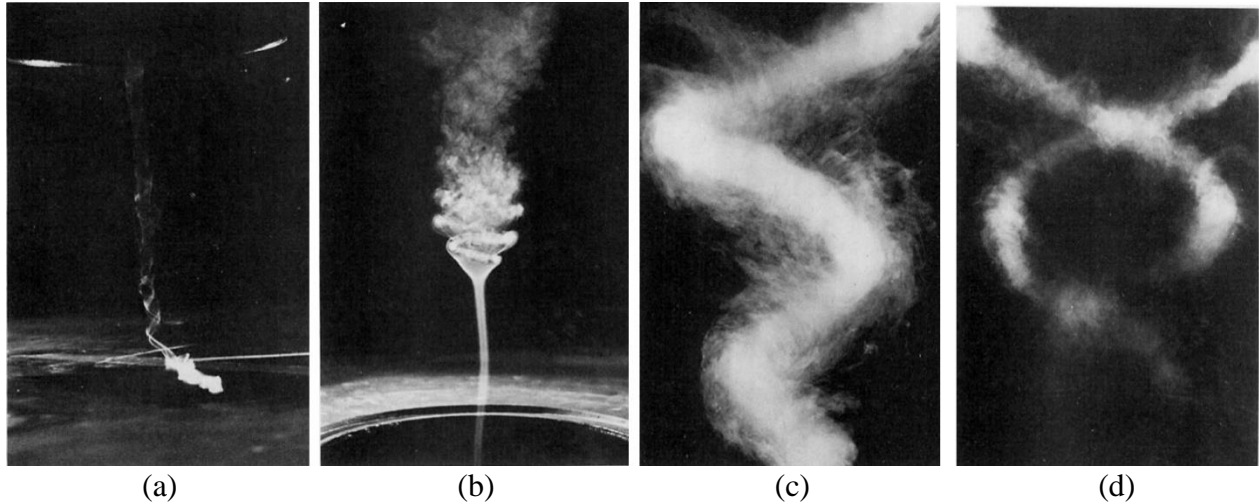


Figure 2. 1: Photograph of tornado-like vortex for (a) small swirl ratio, $S=0.22$, with vortex tilting, (b) moderate swirl ratio, $S=0.57$, with recirculation bubble of vortex breakdown and (c) a single spiral developed behind the bubble, and (d) high swirl ratio, $S=0.96$, with double spiral developed behind the bubble. Double spiral pattern refers also to as double-cell structure. Reproduced with permission from J. Atmos. Sci. (1979), [12]. Copyright 1979 American Meteorological Society.

characteristics [1, 2, 5-9, 14]. This lack of in-depth knowledge about the prominent mechanisms of the tornado-like vortices is attributed to several problems.

The first problem is the vortex wandering (meandering) phenomenon. Mostly for small swirl ratios, the vortex core is displaced in a random fashion around the mean center of the vortex (see Figure 2.1-a) [1, 2]. Wandering has an important impact on the accuracy of flow field measurements and should therefore be also accounted for. Ashton et al. [10] showed that this motion can lead to large errors in estimation of the core radius and maximum tangential velocity. They also showed that high fluctuations in the vortex core are the consequences of wandering motion. While the underlying mechanism of wandering in tornado vortices was not yet discussed, Edstrand et al. [11] suggested the vortex instability effects as the main source of wandering in wing-tip vortices, which is rather similar to what is observed in our case.

The second problem is the vortex breakdown (VBD) phenomenon. When the swirl ratio increases ($S \cong 0.4$), it is observed that the vortex core expands into a recirculation bubble aloft (see Figure 2.1-b) [2,12,13]. This phenomenon is termed vortex break down which is highly turbulent in

nature. By further increasing swirl ratio ($0.7 \leq S \leq 1$), VBD moves upstream and reaches the surface (vortex touch down), which leads to the break of the vortex structure into a double-cell structure [12]. This complex structure contains two intertwined helical vortices orbiting around the geometric center (see Figure 2.1-d). These two vortices mutually interact with each other and generate turbulence [14]. It's not clear if the longevity of these vertical structures is dominated by large-scale instabilities or by turbulent diffusion. Understanding the decay mechanism is important due to its close correlation with variation of vortex circulation. Such a variation would lead to changes in maximum tangential velocity, which is of interest in engineering applications.

To develop a better understanding of the above-mentioned effects for tornado-like vortices, modal analysis can be employed to reveal the dominant turbulent flow characteristics. The main objective of modal analysis is the representation of the relevant flow features using a small number of modes. The classical method for extraction of the dominant features (coherent structures) is proper orthogonal decomposition (POD) method. POD was introduced in fluid dynamics by Lumely [15] for extraction of coherent structures in turbulent flows. Sirovich [16] also introduced snapshot-POD to minimize the computational time involved in the conventional POD. This method, which, in other fields, is often referred to as principal component analysis (PCA), has been experimented by several researchers as a feature-recognition tool [17-20]. However, the general opinion is that POD modes do not necessarily represent coherent structures, or that they do not necessarily have a physical meaning [16, 21-23]. This is mostly due to two factors: (1) POD modes are mutually orthogonal, thus modes higher than the first one may be conditioned by this constraint that has no physical reason; (2) POD modes are static shapes, thus are suited to represent coherent structures that migrate in space [32]. Dealing with turbulent flow field, the orthogonality issue was circumvented by replacing POD with the Independent Component Analysis (ICA), while the identification of time-variant coherent structures was achieved by extending POD and ICA to their dynamic formulations D-POD and D-ICA [33-34]. A recent application of D-POD in fluid mechanics has been presented in [23], where D-POD restricted to stationary signals is called spectral POD.

To date, there has been no crucial examination of the coherent structures of tornado-like vortices using modal analysis partly because of the difficulties involved in laboratory experiments and partly because of the complex nature of the flow. By applying modal analysis to tornado-like

vortices, one can better understand the complex vortex dynamics including vortex wandering, vortex breakdown and sub-vortex dynamics. At the same time, by identifying a reduced number of modes representative of tornado-like turbulent velocity field, one can construct simplified but physically meaningful models. It is hoped that the present investigation may also help in the interpretation of the underlying mechanisms in swirling flows in general.

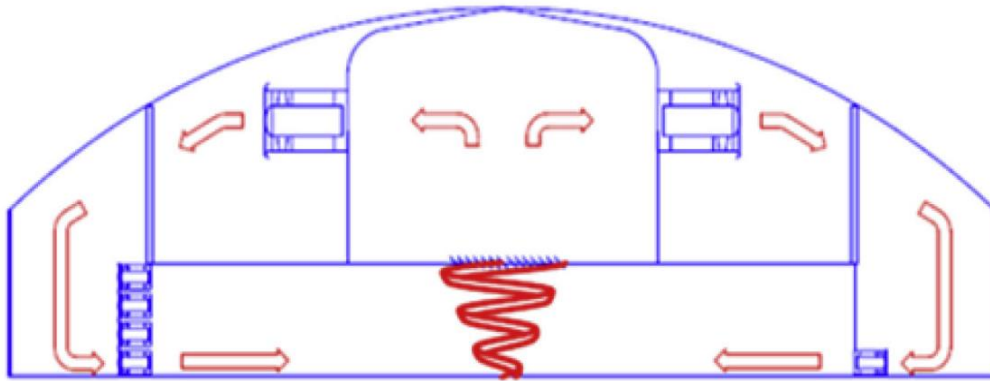


Figure 2. 2: Schematic drawing of Mini-WindEEE Dome. © Elsevier. Used with permission from Ref. [25].

2.2 Experimental setup

The Wind Engineering, Energy and Environment (WindEEE) Dome at Western University is the world's first 3D and time dependent wind testing chamber that provides a novel technique to physically simulate various types of flow fields including tornadoes [25]. A 1/11 scaled model of WindEEE Dome (MWD) was built to reproduce and verify the characteristics of WindEEE Dome. The MWD testing chamber is hexagonal in shape having 8 fans at the base of five walls out of six peripheral walls. The six walls are instrumented with an array of 60 fans distributed into 4 rows \times 15 columns fans. Above the testing chamber and communicating with it through a bell mouth opening, there is another top pressure chamber with 18 top fans distributed on its periphery walls. A schematic drawing of the chamber is shown in Figure 2.2. [25].

In order to produce tornado vortices in the MWD, top fans are used to pull the air out of the hexagonal chamber which afterwards recirculates through the peripheral walls of the main lower chamber. The inflow in the lower chamber passes through vanes (installed at the base of each of

the six walls) whose angles control the radial and tangential inflow velocity components. As the inlet flow moves towards the chamber's center, it is tilted in upward direction by the top fans. Then, the flow recirculates through the bell mouth instrumented with a honeycomb in order to straighten the flow and thus eliminate the effects of fans swirl. A detailed description of the MWD is provided in [2].

In MWD, the geometric aspect ratio a , defined as the ratio of inflow height to the updraft radius, is fixed at 0.35. Moreover, the radial Reynolds number (Re_r) for the present study was 6.7×10^4 . It was shown that the results in MWD and the full scale WinDEE Dome are quasi-independent of Reynolds number when $Re_r \geq 6.7 \times 10^4$ [2]. The main governing parameter is the swirl ratio which is defined as the ratio of tangential to radial velocity components at the inlet, $S = (1/2a) (V_{tan}/V_{rad}) = (1/2a) \tan\theta$, where θ is the vane angle with the normal direction to the sidewall.

Particle image velocimetry (PIV) method was used to measure the velocity field in a horizontal plane at different heights above the surface ($h = 3.5, 4.5, \text{ and } 7 \text{ cm}$). A pulsed Nd:YAG laser generator with a wavelength of 532 nm was used as a source of illumination. The laser run at pulse repetition rates of up to 30 Hz with 120 mJ/pulse output energy. A CCD camera (VA-4M32, Vieworks) with a spatial resolution of 2336×1752 pixels was used to capture images. Using a calibration board, the field of view of the camera was set to 23.4 cm by 17.5 cm and pixel to meter conversion ratio was determined. A cylindrical lens was used to obtain a light sheet with a uniform thickness of 2 mm. The tornado chamber was seeded with Di-Ethyl-Hexyl-Sebacate (C₂₆H₅₀O₄) particles, with an average diameter of 1 μm . These particles have a response time of 2.55×10^{-6} s which is 2 to 4 orders of magnitude smaller than Kolmogorov time scale of the simulated tornado (Kolmogorov time scale varies between 3.06×10^{-4} s and 1.2×10^{-2} s depending on the swirl ratio). A maximum error of 7.2% is estimated for velocity measurements in horizontal planes. A detailed description of the experimental setup is provided in [1, 2].

Due to low sampling frequency of the PIV system (15 Hz), surface pressure measurements have been also performed. 413 static pressure taps were distributed concentrically on a floor panel with a diameter of 56 cm. The frequency of pressure signal collector was 700 Hz and the data were collected for a period of 60 s. Here, the pressure coefficients are normalized by the dynamic

pressure calculated by average updraft velocity at the outlet. The surface pressure measurements are used here only to perform time-frequency analysis in order to emphasize the interpretations resulting from the velocity field analysis. A complete accompanying paper on the surface pressure measurements analysis is to follow. A maximum error of 1.17% is estimated for surface panel measurements.

The random motion of the vortex (wandering phenomenon) can lead to large errors in evaluating the flow field. Thus, it is necessary to remove the effects of wandering from the flow field data. Herein, we used two different algorithms to achieve this goal.

For $S = 0.22$, the vortex center is detected via finding minimum vorticity magnitude since the flow looks laminar. Then, the vortex domain is shifted to the mean center of the vortex using an interpolation procedure [26]. Finally, as a second filter, we removed the PIV snapshots in which vortex displacement is higher than 10^{-3} cm.

For $S = 0.57$ and $S = 0.96$, wandering removal is more challenging since the flow is highly turbulent. We use the following steps to remove wandering effects: (i) the vortex domain is re-centered by detecting the vortex center as the minimum velocity magnitude, (ii) PIV snapshots, in which vortex displacement is higher than 10^{-1} cm, are removed, (iii) a new grid with high resolution in the vortex core is created, and then the velocity field is interpolated in the new grid, and (iv) the vortex domain is re-centered again by detecting the vortex center using the method introduced by Jiang et al. [27]. This algorithm successfully worked for $S = 0.57$, but it was not able to completely remove the wandering effects at $S = 0.96$ for modal analysis purposes.

It is worth noting that vortex wandering is a phenomenon which occurs in a large class of vortex flows, e.g. wing-tip vortices [28, 29], wind turbine vortices [30] and ground vortices [31]. Thus, the present investigation is helpful in the interpretation of the underlying mechanisms in vortex flows in general.

2.3 Modal representation

This section briefly presents the formulations of POD and D-POD for the extraction of the coherent structures from the velocity field [24, 32]. Let us consider a fixed Cartesian reference system x, y, z with origin on the floor at the center of the test chamber and its z -axis vertical directed

upwards. Let $V(p,t)$ be the velocity measured at the point p and time t . Due to the experimental setup, the measurement points p_j ($j=1\dots N$) are organized in a grid on a horizontal plane and only the horizontal components of the velocity are measured. For processing purpose, the measurements are organized in the vector $\mathbf{q}(t)$ defined as:

$$\mathbf{q}(t) = \begin{bmatrix} v_x(p_1, t) \\ v_y(p_1, t) \\ \vdots \\ v_x(p_N, t) \\ v_y(p_N, t) \end{bmatrix} \quad (2.1)$$

where $t = 1\dots N_t$ is the discretized time t (N_t is the number of snapshots), while v_x and v_y are the zero-mean fluctuation of the two horizontal components of the velocity.

2.3.1 Proper Orthogonal Decomposition (POD)

Let $\mathbf{C}_{\mathbf{q}\mathbf{q}}$ be the zero-time-lag covariance matrix estimated from the data as:

$$\mathbf{C}_{\mathbf{q}\mathbf{q}} = \mathbb{E}[\mathbf{q}(t)\mathbf{q}(t)^*] \cong \frac{1}{N_t} \sum_{t=1}^{N_t} \mathbf{q}(t)\mathbf{q}(t)^* \quad (2.2)$$

in which the statistical expectation $\mathbb{E}[\cdot]$ is implemented as a temporal average, assuming that $\mathbf{q}(t)$ is an ergodic random process and the superscript $*$ indicates the conjugate transpose. According to POD, $\mathbf{q}(t)$ is represented by the modal expansion [24,32,33]:

$$\mathbf{q}(t) = \sum_{k=1}^N \boldsymbol{\phi}_k x_k(t) = \boldsymbol{\Phi} \mathbf{x} \quad (2.3)$$

where the vectors $\boldsymbol{\phi}_k \in \mathbb{R}^N$ ($k = 1, \dots, N$) are the eigenvectors of $\mathbf{C}_{\mathbf{q}\mathbf{q}}$, i.e. the solutions of the eigenvalue problem:

$$\mathbf{C}_{\mathbf{q}\mathbf{q}} \boldsymbol{\phi}_k = \lambda_k \boldsymbol{\phi}_k \quad (k = 1, \dots, N) \quad (2.4)$$

The eigenvectors, or the columns in the matrix $\boldsymbol{\Phi}$, are conventionally normalized to unit norm and are assembled column-wise to build the matrix $\boldsymbol{\Phi}$. The coefficients x_k are the Principal Components (PC) of the process and are assembled in the vector $\mathbf{x} = [x_1, x_2, \dots, x_N]^T$. Due to this definition, the eigenvectors are mutually orthogonal, and the PCs are mutually uncorrelated for zero time lag [e.g. 17]. The eigenvectors and the PCs are enumerated in such a way that their

corresponding eigenvalues λ_k are sorted in decreasing order. Since the eigenvalues represent the variance of the PCs, the importance of the terms in Eq. (2.3) tends to decrease as their order increases. The energy of each mode can be defined as: $E_k = \lambda_k / \sum_{k=1}^N \lambda_k$. In practical applications, the first few terms of the summation provide a good representation of the observed phenomenon, while neglecting high-order terms leads to a noise cancellation [13].

2.3.2 Dynamic Proper Orthogonal Decomposition (D-POD)

A limitation of POD is implicit in their definition, which is based on a static mixing. The modes are constant in time, thus if a coherent structure has a time evolution, more than one mode may be necessary for its representation. It is the case, for example, of coherent pressure distribution that translate due to the advection produced by the main flow. A general way to overcome this limitation is to generalize the static mixture represented by Eq. (2.3) into a convolutive mixture

$$\mathbf{q}(p, t) = \int_0^t \mathbf{\Phi}(p, \tau) \mathbf{x}(t - \tau) d\tau \quad (2.5)$$

in which the mixing matrix $\mathbf{\Phi}$ depends on the time lag τ and has the role of impulse response function. In Eq. (2.5), $\mathbf{\Phi}$ is defined according to D-POD, the PC $x_j(t)$ are mutually uncorrelated for any time lag τ [24].

If the modal representation is exploited to extract coherent structures, the use of Eq. (2.5) is not practical and it is preferred to translate it in the frequency domain as:

$$\hat{\mathbf{q}}(p, \omega) = \hat{\mathbf{\Phi}}(p, \omega) \hat{\mathbf{x}}(\omega) \quad (2.6)$$

where the symbol $\hat{\cdot}$ represents the Fourier transform and ω is the circular frequency.

In the frequency domain, D-POD is formally a static mixing (different for each frequency) and the mixing matrix $\hat{\mathbf{\Phi}}$ may be interpreted as a frequency response function. The estimation of $\hat{\mathbf{\Phi}}$ from data can be obtained through the following procedure:

1. Samples of $\hat{\mathbf{q}}(\omega)$ are obtained by calculating the Fourier transform of time portions of the given signal $\mathbf{q}(t)$ through the algorithm FFT preceded by a proper windowing. Let $\hat{\mathbf{q}}^{(h)}(\omega)$ ($h=1, \dots, N_w$) be the Fourier transform calculated for the h^{th} time window.

2. The covariance matrix of $\hat{\mathbf{q}}(\omega)$ is computed by averaging on the available time windows as

$$\mathbf{C}_{\hat{\mathbf{q}}\hat{\mathbf{q}}}(p, \omega) = E[\hat{\mathbf{q}}(p, \omega)\hat{\mathbf{q}}(p, \omega)^*] \cong \frac{1}{N_w} \sum_{h=1}^{N_w} \hat{\mathbf{q}}^{(h)}(p, \omega)\hat{\mathbf{q}}^{(h)*}(p, \omega) \quad (2.7)$$

where the symbol $*$ represent the conjugate transpose

3. The mixing matrix is calculated by solving the eigenvalue problem

$$\mathbf{C}_{\hat{\mathbf{q}}\hat{\mathbf{q}}}(\omega)\hat{\Phi}_k(p, \omega) = \gamma_k(\omega)\hat{\Phi}_k(p, \omega) \quad (k = 1, \dots, N) \quad (2.8)$$

The application of D-POD as specified above requires some observations:

1. The number N_w of time windows extracted from the dataset should be large enough to obtain a correct estimation of the expectation in Eq. (2.7); on the other hand, the length of the time windows determines the discretization of the frequency values obtained from the Fourier transform.
2. If D-POD is used to extract coherent structures, Eqs. (2.7) and (2.8) must be solved only for some (usually a few) frequencies of interest for which the observed phenomenon is relevant.
3. The covariance of $\hat{\mathbf{q}}(p, \omega)$ is, apart from a normalization constant, equal to the Power Spectral Density function (PSD) of $\mathbf{q}(p, t)$ and Eq. (2.7) corresponds to the Welch's estimation method.
4. Since $\mathbf{C}_{\hat{\mathbf{q}}\hat{\mathbf{q}}}(\omega)$ is Hermitian symmetric, the D-POD modes $\hat{\Phi}_k$ are mutually orthogonal in \mathbb{C}^N .
5. Modes obtained by D-POD are complex valued, thus represent distributions characterized by amplitude and phase. To overcome the difficulty of visualization and physical interpretation, the complex modes can be represented as a sequence of real modes defined as [24,34]:

$$\bar{\Phi}_k(p, \omega, \alpha) = \text{Re}[\hat{\Phi}_k(p, \omega) e^{i\alpha}] \quad (2.9)$$

where α is a phase shift common to all the vector components, which can also be related to the time-lag $\tau = \alpha/\omega$.

Beside the procedure described above, D-POD modes can be obtained using a full time-domain method that has the advantage of relying on the same algorithms developed for standard POD without the need of a specific implementation. In the present study, the full time-domain D-POD is chosen and can be formulated according to the following procedure:

1. The given signal $\mathbf{q}(t)$ is band-pass as

$$\mathbf{q}_\omega(\mathbf{p}, t) = BP[\mathbf{q}(\mathbf{p}, t); \omega; \Delta\omega] \quad (2.10)$$

where $BP[\cdot]$ is a band-pass filtered with central frequency ω and bandwidth $\Delta\omega$. In this study, only one frequency band $\Delta\omega=3.5\text{Hz}$ with central frequency $\omega=4\text{ Hz}$ is considered since the sampling frequency of PIV system is 15 Hz.

2. An analytic signal is constructed by completing $\mathbf{q}_\omega(\mathbf{p}, t)$ with its quadrature term as

$$\tilde{\mathbf{q}}_\omega(\mathbf{p}, t) = \mathbf{q}_\omega(\mathbf{p}, t) + i\mathcal{H}[\mathbf{q}_\omega(\mathbf{p}, t)] \quad (2.11)$$

where $\mathcal{H}[\cdot]$ is the Hilbert transform.

3. The analytic signal is processed through standard POD with the only difference with respect to Eqs. (2.1-2.3) that the signal is complex valued.

Apparently, the time-domain D-POD has a user-settable parameter, the filter bandwidth $\Delta\omega$, that is not present in standard D-POD. In reality, in standard D-POD this parameter is determined indirectly by the length of the time windows used to calculate the Fourier transform of the signal.

2.4 Analysis of a simulated synthetic vortex

POD modes have been widely employed in fluid dynamics to identify dominant flow features referred to as coherent structures, which are used to reveal the occurrence of large-scale phenomena that are hidden in a turbulent flow [33]. Coherent structures should be interpreted as spatially-coherent velocity components whose amplitude fluctuates with zero mean and are superimposed to the mean flow. In other terms, the coherent structures are ideal flow fields representing zero-mean corrections to the mean flow. Due to this nature, the interpretation of the coherent structures is reasonably straightforward when the mean flow is simple, but it requires a substantial attention whenever the mean flow is complex like in the present case of the tornado-like vortex.

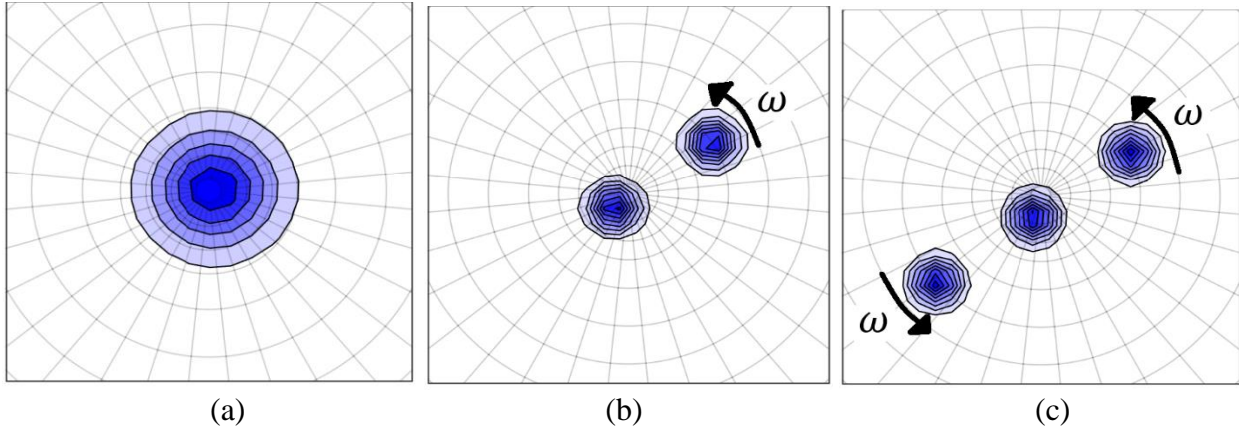


Figure 2. 3: A snapshot of the vorticity field (1/s) of the idealized (synthetic) vortex (a) with Gaussian random wandering and/or variation in size, (b) with a single spiral rotating around the vortex and (c) with a double spiral rotating around the vortex.

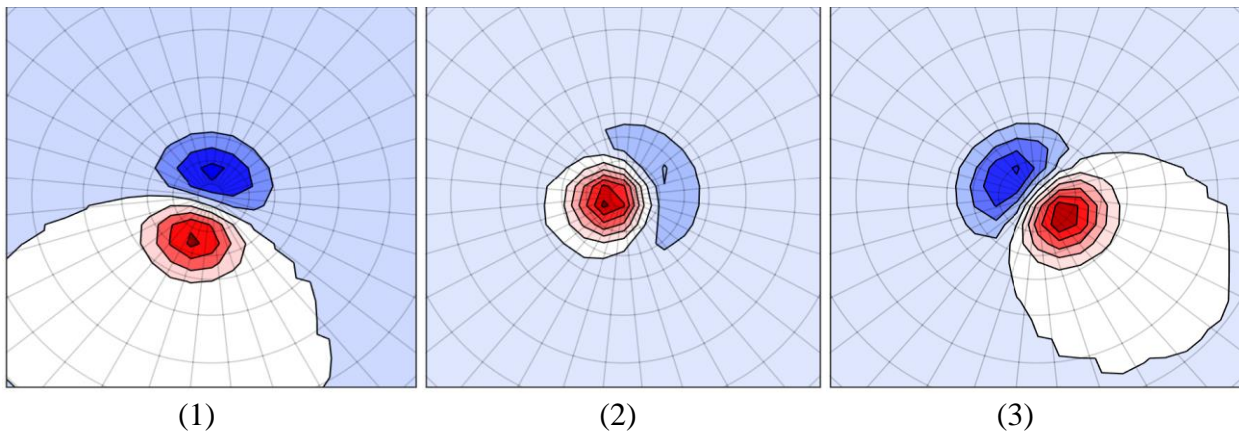


Figure 2. 4: Time history of fluctuating vorticity field (1/s) of the simulated vortex with only Gaussian random wandering. Positive (negative) values of vorticity are shown in red (blue) color.

In this section, we investigate the POD representation of an idealized vortex to help us with the interpretation of the modes extracted from the experimental measurements. The vortex is simulated with a vorticity field distributed according to a bivariate Gaussian function. To simulate different phenomenon in our tornado-like vortex, four different cases are considered for simulation of the synthetic vortex: (i) a vortex with only Gaussian random wandering (Figure 2.3-a), (ii) a vortex with a Gaussian random wandering plus a size variation (Figure 2.3-a), (iii) a vortex with a single spiral rotating around the vortex plus wandering motion (Figure 2.3-b), and (iv) a vortex with a

double spiral rotating around the vortex plus wandering motion (Figure 2.3-c). A snapshot of the vorticity field of the idealized vortex for these simulation cases is shown in Figure 2.3. To apply POD, we remove the mean component and then calculate the modes.

The analytic expression for the first simulation case is as follows:

$$f(x, y, t) = \frac{1}{2\pi\sigma^2} \exp\left(-\frac{(x-x_0)^2}{2\sigma} - \frac{(y-y_0)^2}{2\sigma}\right) \quad (2.12)$$

where $\sigma = 0.1$, represents the vortex size; x and y are the domain coordinates, x_0, y_0 is the vortex center position. To simulate the vortex wandering, the vortex center is located randomly at each time step using a normal distribution in a range of -1 to 1. The snapshots of the fluctuating vorticity field are shown in Figure 2.4. It shows that the fluctuating field has dipole-type shape with both negative and positive values, and sometimes it consists of mainly a single vortex. Figure 2.5 shows the first five POD modes of the idealized vortex with only Gaussian random wandering around the geometric center. The first two modes represent wandering motion of the vortex and mode three shows a single vortex. Modes four and five are not physically meaningful and are due to the orthogonality condition embedded in POD.

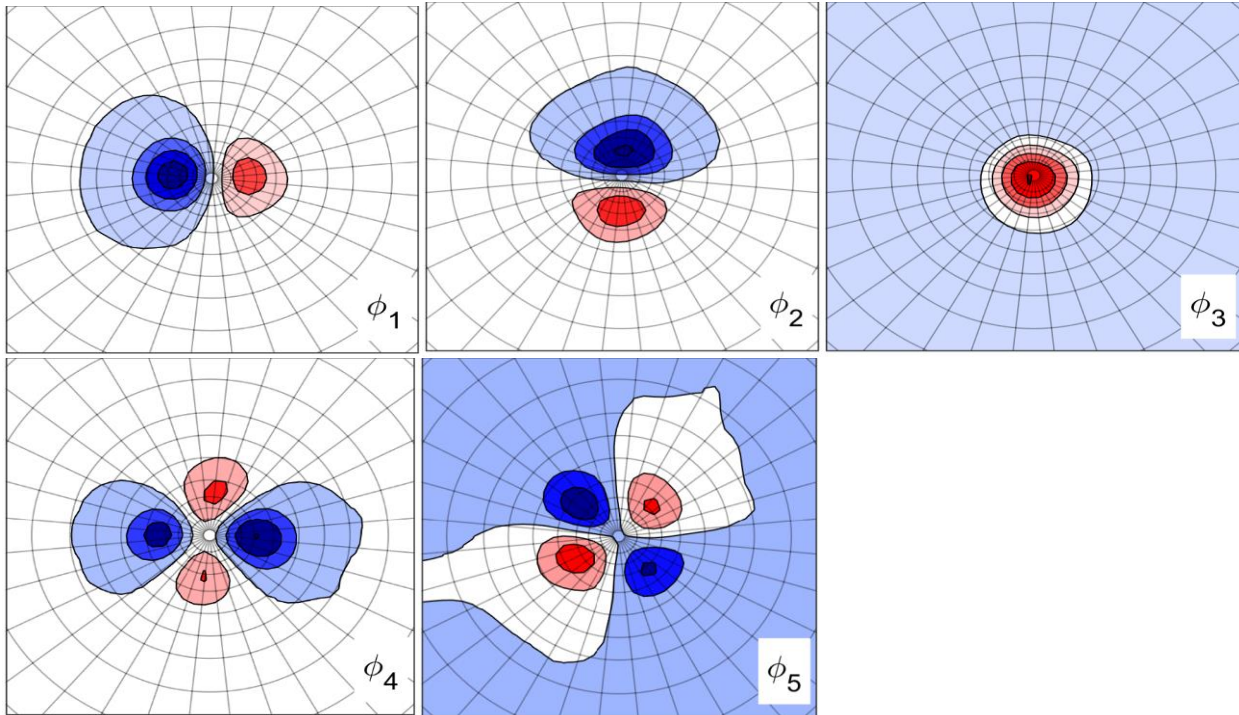


Figure 2. 5: The first five POD modes of the idealized (synthetic) vortex with only Gaussian random wandering.

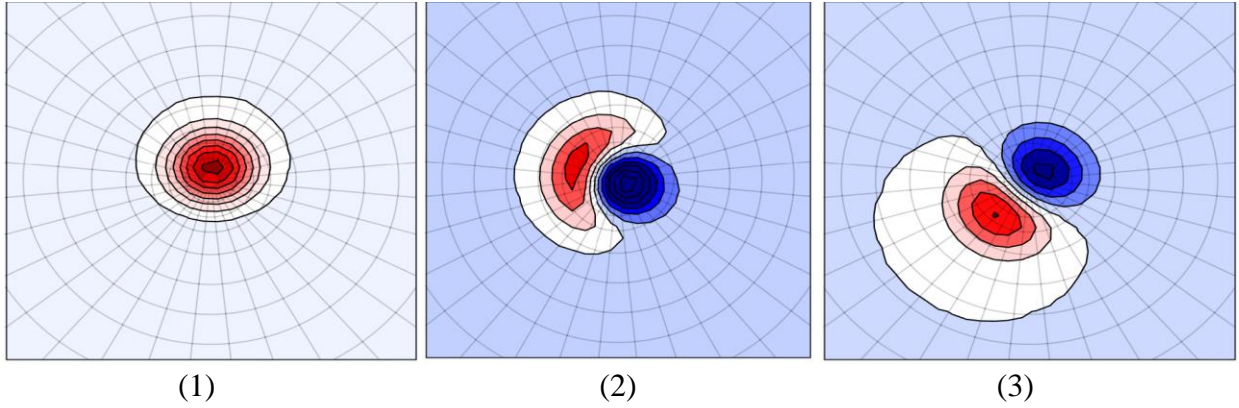


Figure 2. 6: Time history of fluctuating vorticity field of the simulated vortex with Gaussian random wandering plus a size variation. Positive (negative) values of vorticity are shown in red (blue) color.

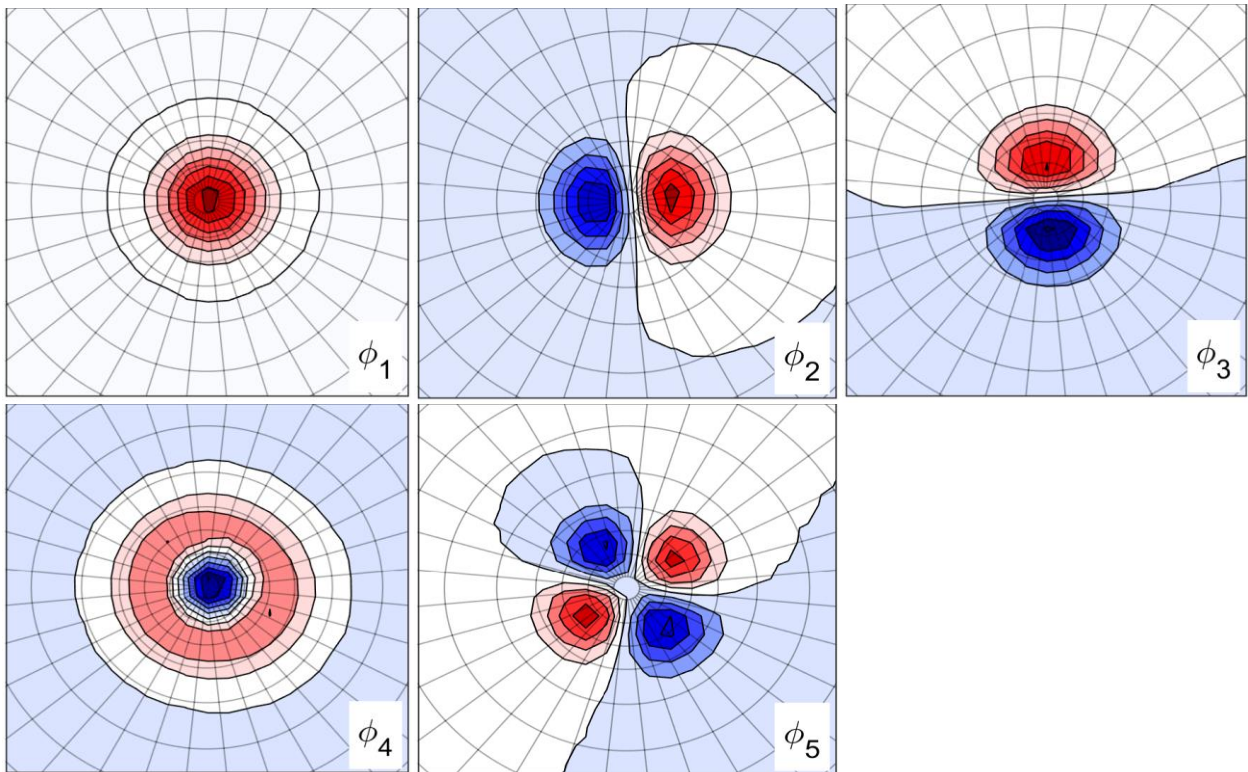


Figure 2. 7: The first five POD modes of the idealized (synthetic) vortex with Gaussian random wandering and variation in size.

The second simulation case which is a vortex with a Gaussian random wandering plus a size variation (see Figure 2.3-a) is generated using the same procedure for the first simulation case, except vortex size (σ) which is changing periodically using the equation $\sigma = 0.3 + 0.2 \sin (t)$.

Time history of the fluctuating vorticity field is shown in Figure 2.6. It shows that the fluctuating field consists of a single vortex, and then it gradually takes a dipole shape. Figure 2.7 shows the first five POD modes of the fluctuating flow field. Mode 1 shows a single vortex and modes 2 and 3 correspond to wandering motion. Mode 4 represents the size variation of the vortex, and mode 5 is non-physical.

The third simulation case, which is a single spiral rotating around a vortex plus wandering motion (see Figure 2.3-b), is generated using the following the formula:

$$f(x, y, t) = \frac{1}{2\pi\sigma_0^2} \exp\left(-\frac{(x-x_0)^2}{2\sigma_0} - \frac{(y-y_0)^2}{2\sigma_0}\right) + \frac{1}{2\pi\sigma_1^2} \exp\left(-\frac{(x-x_1)^2}{2\sigma_1} - \frac{(y-y_1)^2}{2\sigma_1}\right) \quad (2.13)$$

The first part in the Eq. (2.13) generates a single vortex at the center, and the second part generates a spiral vortex rotating the vortex. Both the single vortex and the spiral have the same size $\sigma_0 = \sigma_1 = 0.04$. The vortex center position, x_0 and y_0 , are located randomly at each time step using a normal distribution in a range of -1 to 1. The spiral position, x_1 and y_1 , are calculated using the equation: $x_1 = x_0 + 1.5 \cos(\omega t)$ and $y_1 = y_0 + 1.5 \cos(\omega t)$, where ω is the angular velocity of spiral.

The fourth simulation case, which is a double spiral rotating around a vortex plus wandering motion (see Figure 2.3-c), is generated using the same procedure for the third simulation case, except that two spirals are rotating around the vortex:

$$f(x, y, t) = \frac{1}{2\pi\sigma_0^2} \exp\left(-\frac{(x-x_0)^2}{2\sigma_0} - \frac{(y-y_0)^2}{2\sigma_0}\right) + \frac{1}{2\pi\sigma_1^2} \sum_{i=1}^2 \exp\left(-\frac{(x-x_i)^2}{2\sigma_1} - \frac{(y-y_i)^2}{2\sigma_1}\right) \quad (2.14)$$

The first part in the Eq. (2.14) generates a single vortex at the center, and the second part generates a double spiral. The second spiral position, x_2 and y_2 , are calculated using the equation: $x_2 = x_0 - 1.5 \cos(\omega t)$ and $y_2 = y_0 - 1.5 \cos(\omega t)$, where ω is the angular velocity of spiral.

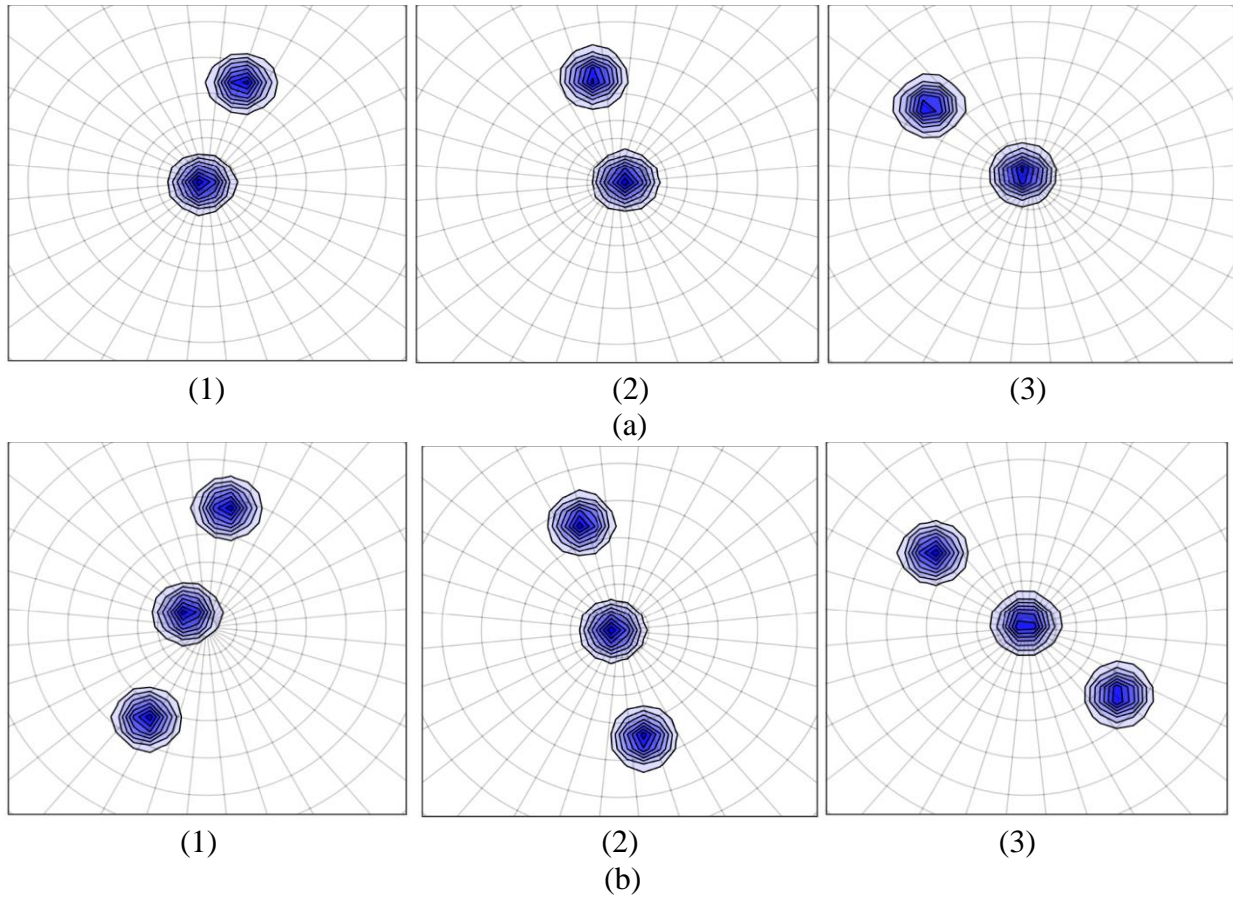
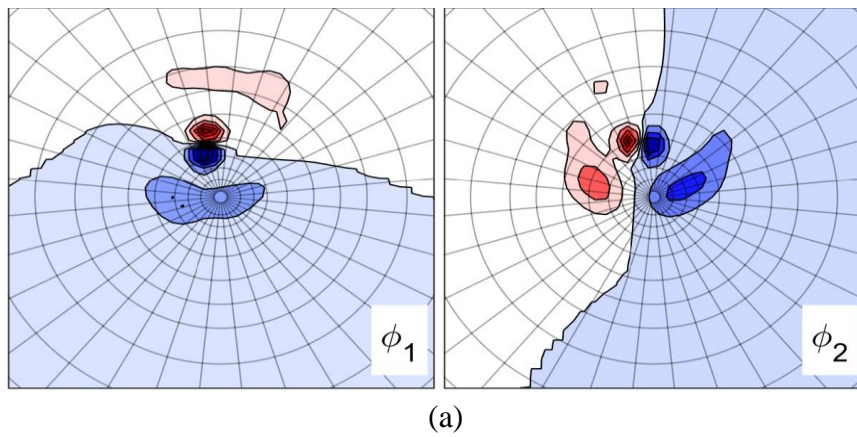


Figure 2. 8: Time history of the vorticity field (1/s) of (a) single and (b) double spiral rotating around the vortex.



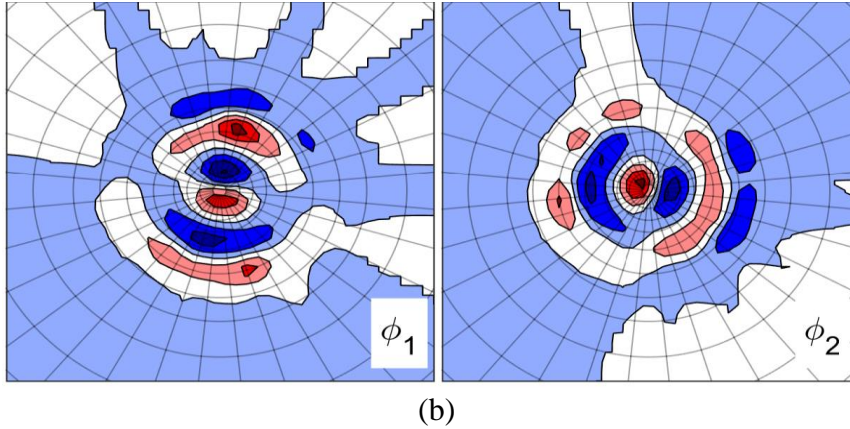


Figure 2. 9: The first two POD modes of the idealized (synthetic vortex) with (a) single and (b) double spiral rotating around the vortex (see Figures 3-b and 3-c).

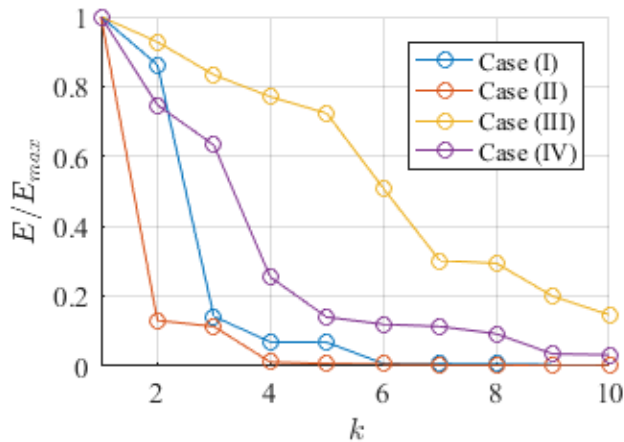


Figure 2. 10: Energy of POD modes of the idealized (synthetic) vortex with four different simulation cases: (I) vortex with only wandering, (II) vortex with wandering plus size variation, (III) vortex with single spiral and (IV) vortex with double spiral.

Time history of the vorticity field of the third and fourth cases are shown in Figure 2.8. It shows the rotation of the single (double) spiral around a single vortex at center while having wandering motion. The first two POD modes of third and fourth simulation cases are shown in Figure 2.9. For the vortex with single spiral, the POD mode shows a well separated dipole (Figure 2.9-a), while the dipoles wrap around each other for the vortex with double spiral (Figure 2.9-b). We will show that these modes are very similar to the POD mode of tornado-like vortex for swirl ratio $S = 0.57$ and 0.96 .

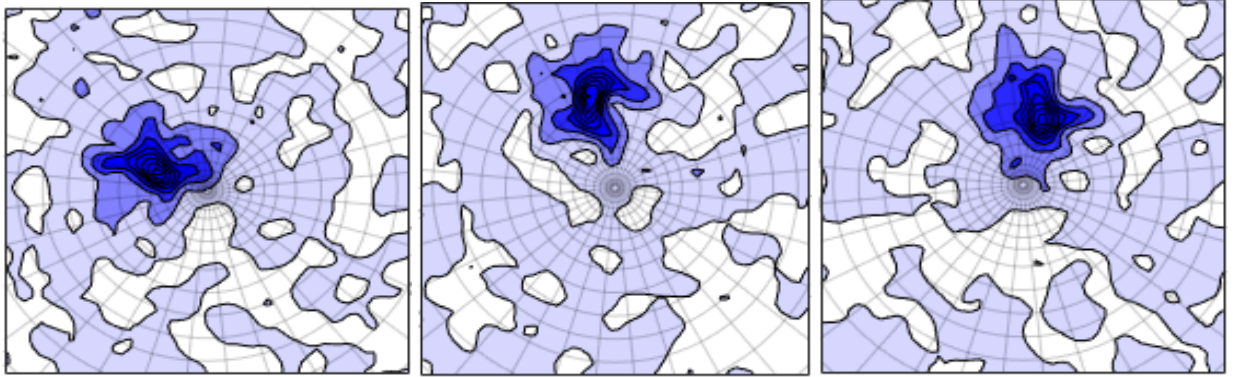
The energy of POD modes of the synthetic vortex for the four simulation cases are shown in Figure 2.10. It shows that the first few POD modes contribute the most to the total energy, while the subsequent modes have quite comparable effects. This suggests that we can characterize the large-scale fluctuations of the vorticity field by looking into only five POD modes. It can be noted that the dipole-type mode pairs (modes 1 and 2 for Case I, Figure 2.5 and modes 2 and 3 for case II, Figure 2.7) are associated to eigenvalues that are very close each other. This suggests that the dipole-type mode pairs represent 2-dimensional eigenspaces and are likely to be related to a unique phenomenon, namely the vortex wandering.

The simulation of the synthetic vortex can help us to have a better understanding of different phenomena (wandering motion, vortex breakdown and transition from one-cell to two-cell structures) in our tornado-like vortex. In the next section, we will look into the mean flow field of the tornado-like vortex and then apply POD on its fluctuating flow field.

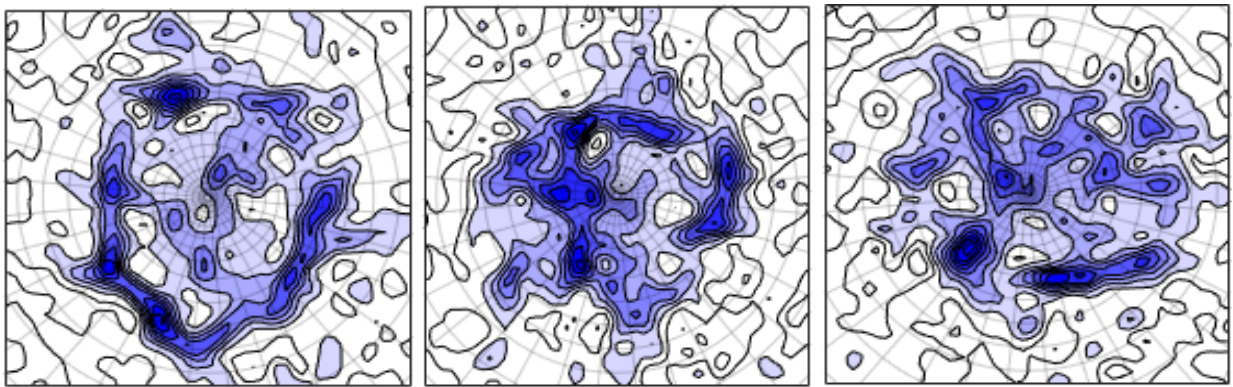
2.5 Analysis of experimental flow field

The tornado-vortex flow structure is highly dependent on the swirl ratio (S). The swirl ratio based on the vane angle collapses well with the value obtained from maximum circulation Γ_∞ , $S = \Gamma_\infty/2Qa$, where Q is the flow rate [2]. In the present work, three values of swirl ratio ($S = 0.22, 0.57$ and 0.96) were chosen since they represent distinct vortex flow structures.

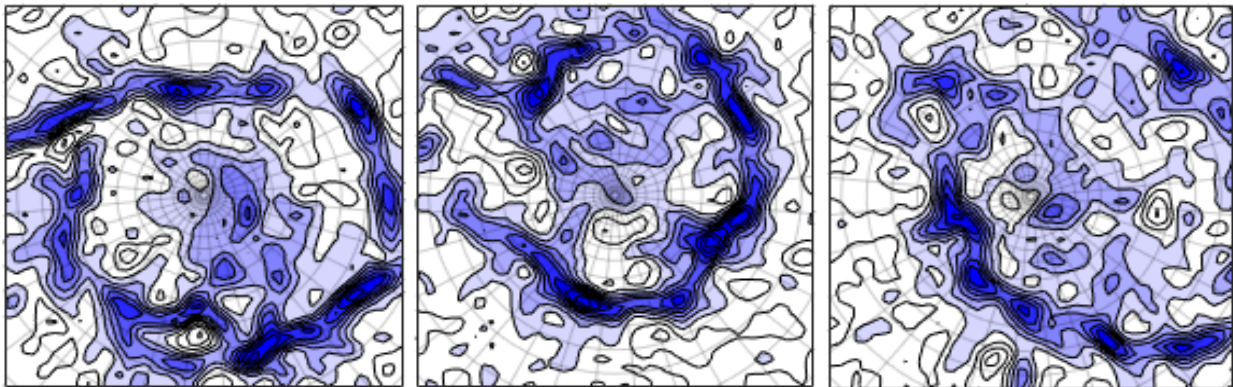
Church et al. [12] showed that for $S \cong 0.2$, the vortex is tilted at low heights while it is subjected to the highly intensified random motion wandering (see Figure 2.1-a). For $S \cong 0.4$, a recirculation bubble (vortex breakdown) forms aloft (see Figure 2.1-b), which moves toward the surface by increasing the swirl ratio, until it touches the surface panel around $S \cong 0.57$. When the swirl ratio is $0.7 \leq S \leq 1$, transition from single-cell to two-cell structures occurs. Note that double-cell structure includes two intertwined co-rotating sub-vortices that are imbedded in the fluctuating flow field. Time histories of the vorticity fields at the height of 3.5 cm above the surface for the three different swirl ratios are shown in Figure 2.11.



(a)



(b)



(c)

Figure 2. 11: Time histories of experimental vorticity fields (1/s) at height of 3.5 cm above the surface for (a) $S = 0.22$, (b) $S = 0.57$, and (c) $S = 0.96$. (Time step size is 0.067 s).

Here, we explore the mean flow field first and then the main mechanism underlying these phenomena using POD/D-POD techniques. To foster the physical interpretation of the POD/D-POD modes extracted from the experimental measurements, we also analyzed the velocity field produced by a simulated vortex in Section 4.

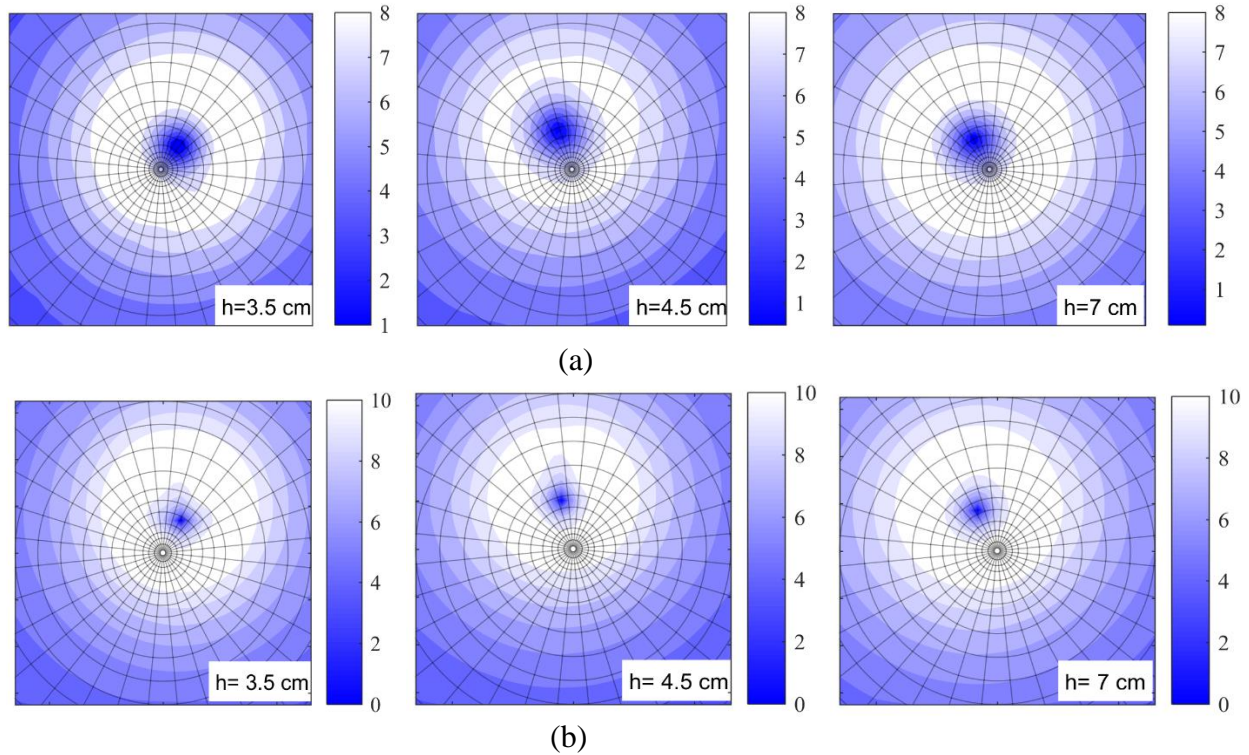


Figure 2. 12: Mean tangential velocity (m/s) contours for $S = 0.22$ at different heights for (a) unremoved wandering and (b) removed wandering.

2.5.1 Mean flow field of tornado-like vortex

(a) $S = 0.22$. Figure 2.12 shows the mean tangential velocity field for unremoved and removed wandering effects. Limited variations of the maximum tangential velocity and the core radius with height are observed. The average center of the vortex is not at the center of the test chamber as the vortex is weak. When wandering effects are removed (via re-centering the instantaneous vortex to its mean center), the maximum tangential velocity at $h = 3.5 \text{ cm}$ is increased from 9.3 m/s to 11.5 m/s and the core radius is decreased from 2.9 cm to 2.2 cm. Figure 2.13 shows the mean radial velocity field. A negative (positive) value of radial velocity shows convergent (divergent) flow towards the vortex center. It is observed that the radial flow distribution is asymmetric and accompanied by divergent flow at the vortex center. The divergent radial flow inside the core is unexpected as at this swirl ratio ($S = 0.22$) no recirculation breakdown bubble is expected to cause a downdraft and therefore divergent radial flow. The absence of vortex breakdown will be inferred later (Figure 2.25-a) from the steadiness of the coherent structures (or laminar appearance) along the height for this swirl ratio. Interestingly, when we remove the wandering effects (Figure 2.13-

b), the divergent flow (shown in red) remains consistent at lower heights ($h = 3.5$ and 4.5 cm) but disappears at higher heights ($h = 7$ cm). It is believed that this divergent flow is due to vortex tilting at low heights. A photograph of vortex tilting at low heights for small swirl ratios ($S = 0.2$) is shown in Figure 2.1-a [12]. Tang et al. [35] have also reported divergent radial flow in tornado-like vortex with small swirl ratio at low heights and attributed this behavior to the complex structure of vortex.

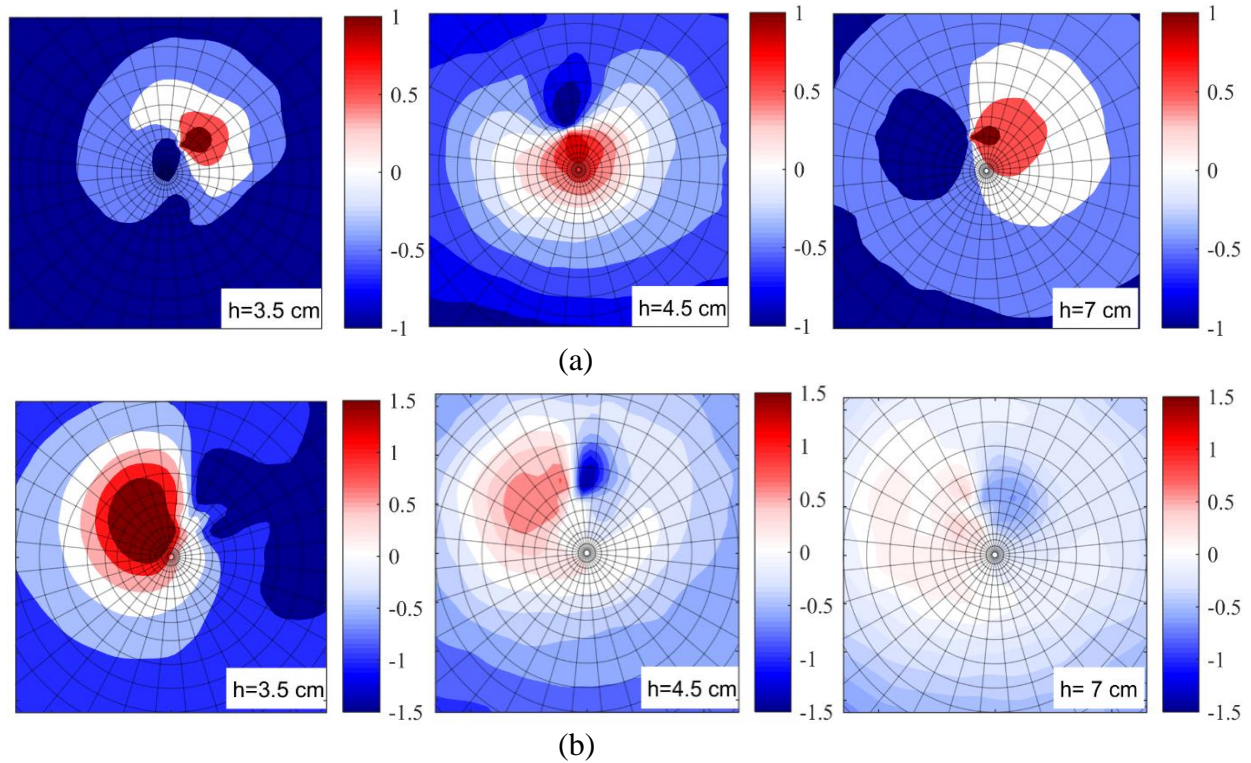
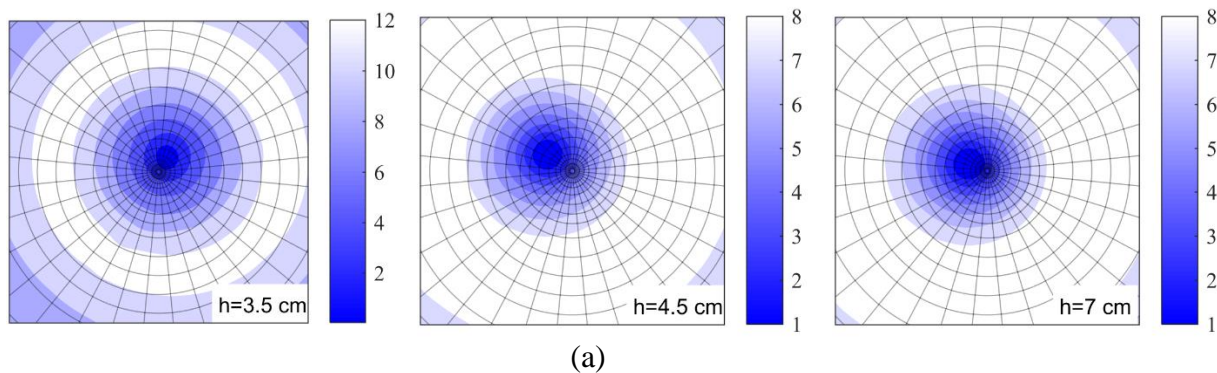
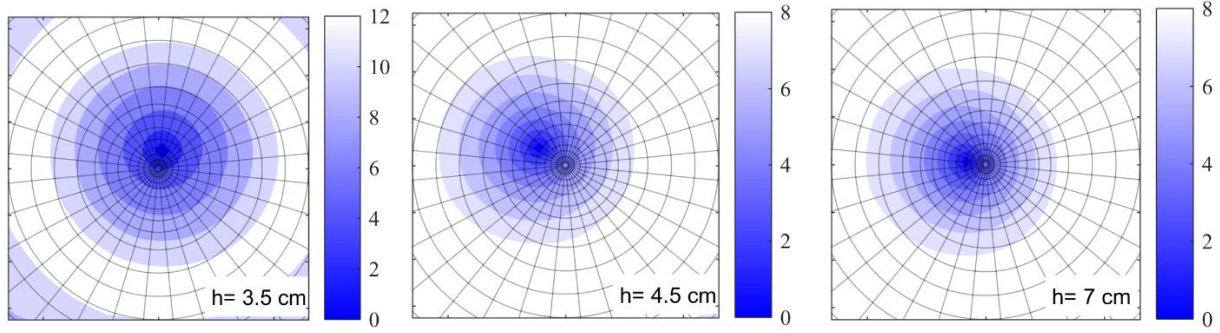


Figure 2. 13: Mean radial velocity (m/s) contours for $S = 0.22$ at different heights for (a) unremoved wandering and (b) removed wandering. Convergent and divergent radial flow are shown respectively in blue and red colors.

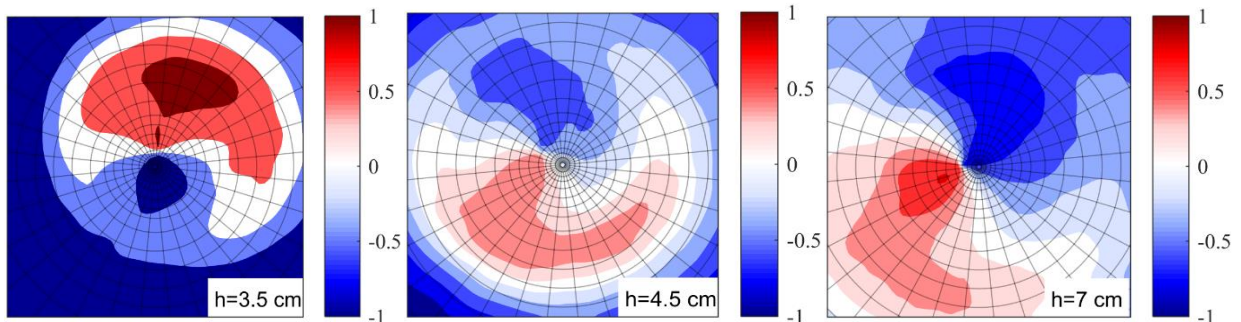




(b)

Figure 2. 14: Mean tangential velocity (m/s) contours for $S = 0.57$ at different heights for (a) un-removed wandering and (b) removed wandering.

(b) $S = 0.57$. Figure 2.14 shows the mean tangential velocity field. The peak tangential velocity and core radius are increased with respect to the ones observed for $S = 0.22$, and the peak tangential velocity is reduced rapidly near the ground. Furthermore, the mean center of the vortex is closer to the geometric center compared to the $S = 0.22$ case. When wandering effects are removed, the maximum tangential velocity at $h = 3.5 \text{ cm}$ is increased from 12.8 m/s to 13 m/s and the core radius is decreased from 6.4 cm to 5.9 cm. Figure 2.15 shows the mean radial velocity field. A negative and positive value of radial velocity corresponds to convergent and divergent flow towards the vortex center, respectively. The outward flow (shown in red) in this swirl ratio $S = 0.57$ is due to the presence of recirculation bubble vortex breakdown inferred later (Figure 2.25-b) based on the observation of an unsteady behaviour along the vortex height. Moreover, when wandering effects are removed, the radial flow becomes almost axisymmetric at lower heights, $h = 3.5 \text{ cm}$.



(a)

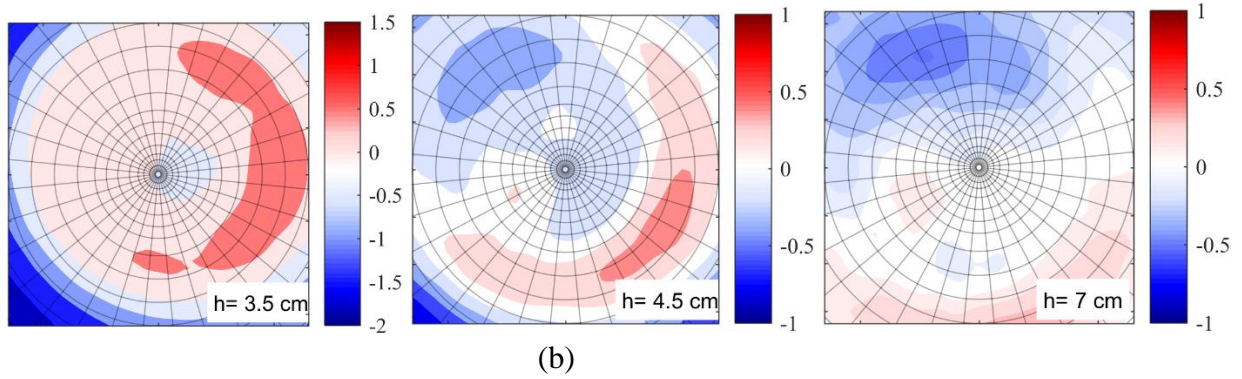


Figure 2. 15: Mean radial velocity (m/s) contours for $S = 0.57$ at different heights for (a) un-removed wandering and (b) removed wandering. Convergent and divergent radial flow are shown respectively in blue and red colors.

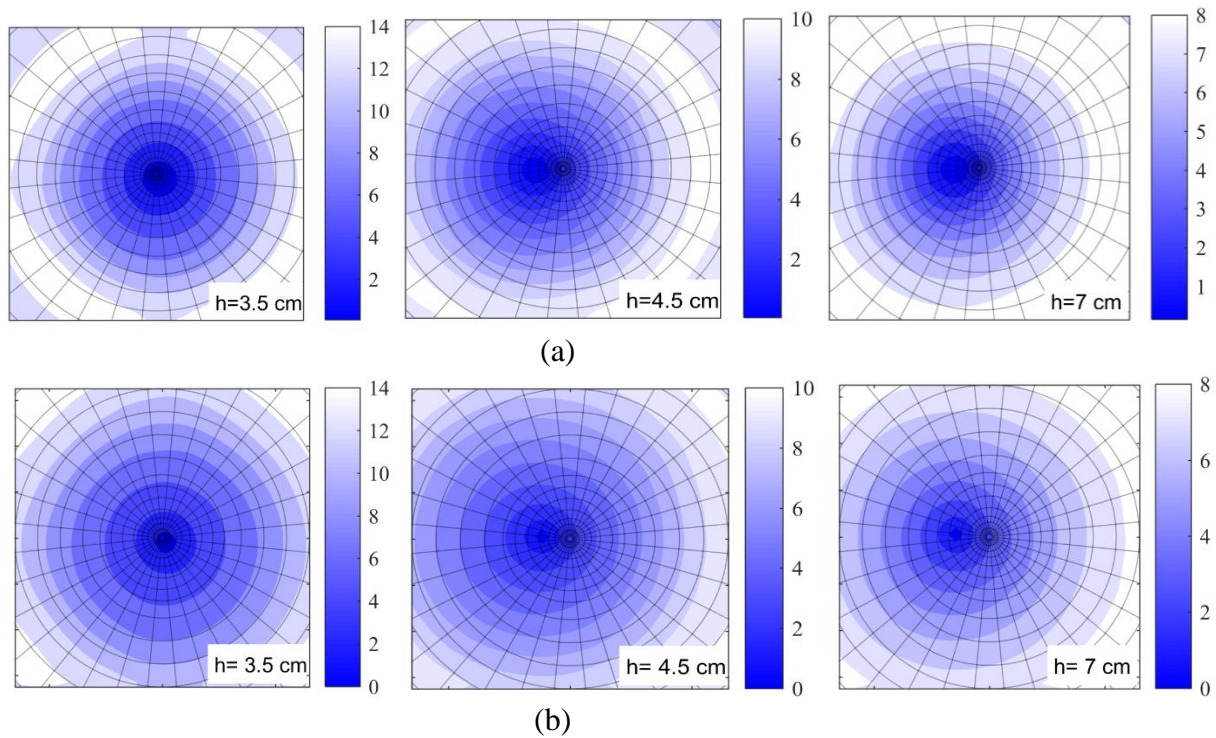


Figure 2. 16: Mean tangential velocity (m/s) contours for $S = 0.96$ at different heights for (a) un-removed wandering and (b) removed wandering.

(c) $S = 0.96$. Figure 2.16 shows the mean tangential velocity field. Due to the expanded core radius, a smaller area of the outer region is captured in PIV plane. Overall, the maximum tangential velocity is increased compared to the case with $S = 0.57$, but varies along the vortex height. When wandering effects are removed, the maximum tangential velocity and core radius at $h = 3.5 \text{ cm}$ remain almost constant and equals to 14.6 m/s and 8.2 cm, respectively. Figure 2.17 shows the mean radial velocity field. It can be seen that for $h = 3.5 \text{ cm}$, the radial outflow expands in an

annular form with a stagnant area (zero-value velocity) inside the core region. This quasi axisymmetric flow structure weakens with increasing height.

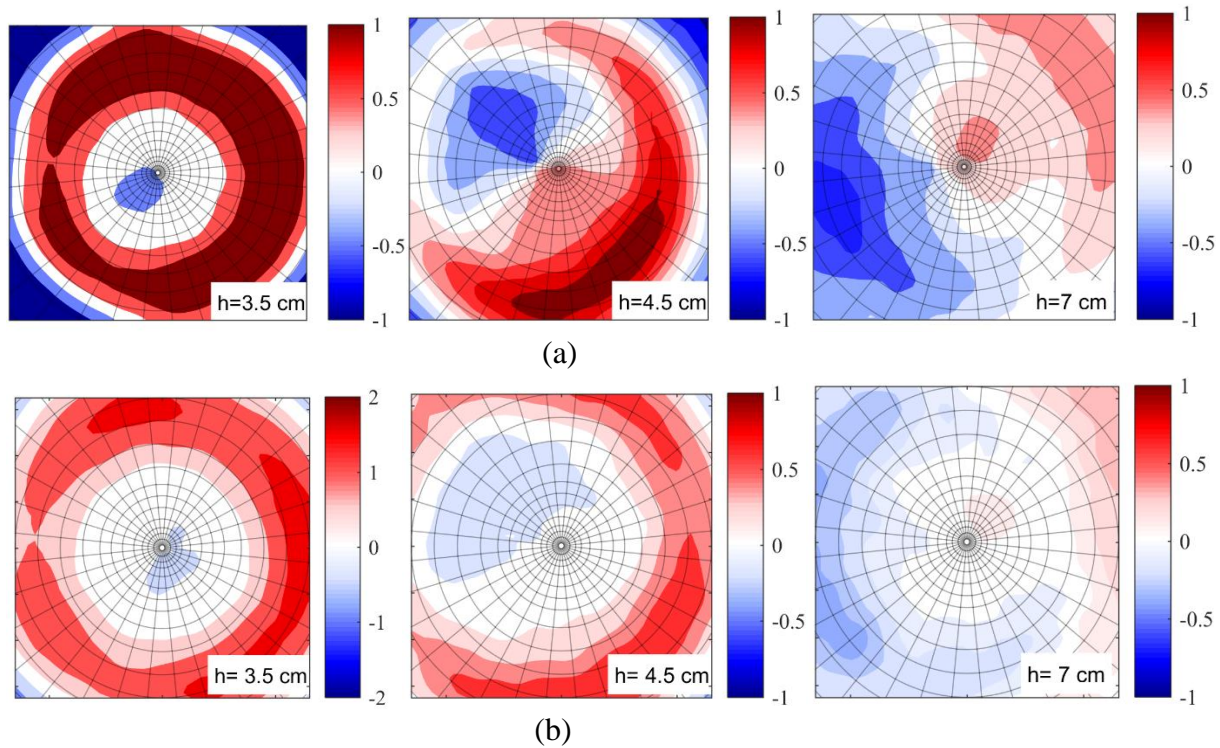


Figure 2. 17: Mean radial velocity (m/s) contours for $S = 0.96$ at different heights for (a) un-removed wandering and (b) removed wandering. Convergent and divergent radial flow are shown respectively in blue and red colors.

2.5.2 Modal analysis

This section describes the results of the modal analysis applied to the measured velocity fields. The modes extracted by POD represent coherent 2-D velocity fields defined on the horizontal measurement plane. To simplify the interpretation of the modes, the figures that follow represent the vertical component of the vorticity corresponding to these velocity fields.

(a) $S = 0.22$. Figure 2.18 shows the first five POD modes of the vorticity field with un-removed wandering effects. The vorticity field is calculated by the curl of POD modes of velocity components in x and y coordinates in the horizontal planes of the PIV measurements. These POD modes are very similar to what was observed for the synthetic vortex with Gaussian random wandering (compare Figures 2.5 and 2.18). Dipole modes 1 and 2 represent the wandering motion of the vortex. Mode 3 shows a single vortex. Modes 4 and 5 are due to the orthogonality and thus

non-physical. The animated movie of mode 1, obtained by D-POD, is shown in Figure 2.19. D-POD of mode 1 shows the rotation of dipoles at different phase shifts (α), picturing the vortex wandering phenomenon. Note that POD modes 1 and 2 correspond to a single vortex but appear as two vortices due to the wandering motion. This conclusion is confirmed by the fact that the first POD mode applied on the corrected velocity field (removed wandering effects) represents a single vortex (see Section 6). In short, for this swirl ratio $S = 0.22$, the flow field is characterized by a single vortex subjected to Gaussian random wandering.

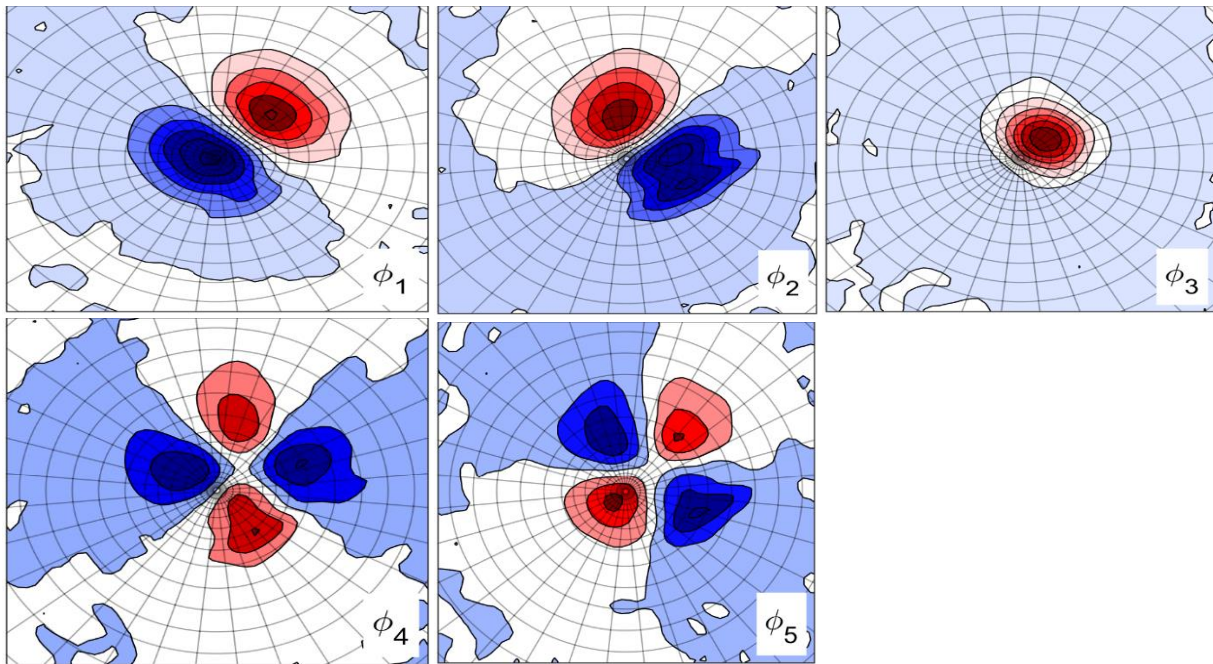
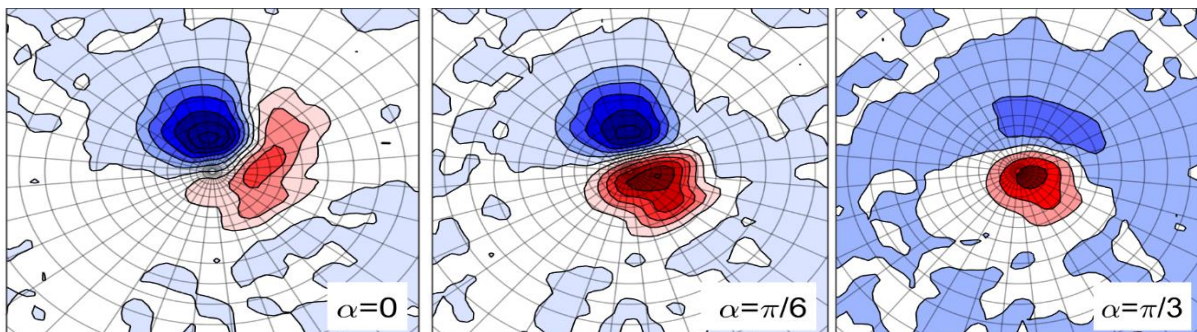


Figure 2. 18: First five POD modes of the vorticity field with un-removed wandering for $S = 0.22$ at $h = 3.5 \text{ cm}$. Positive (negative) values of vorticity are shown in red (blue) color.



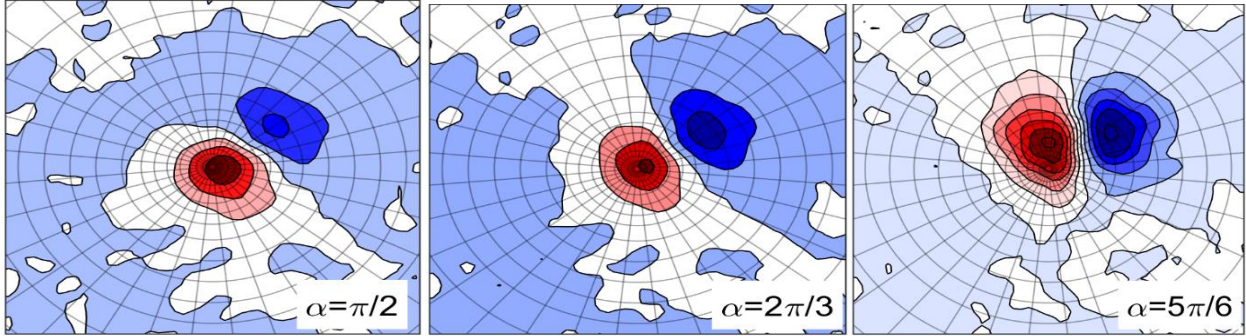


Figure 2. 19: D-POD mode 1 with un-removed wandering, for $S = 0.22$ and $h = 3.5 \text{ cm}$ at six different phase shifts (α), representing time-lag. Positive (negative) values of vorticity are shown in red (blue) color.

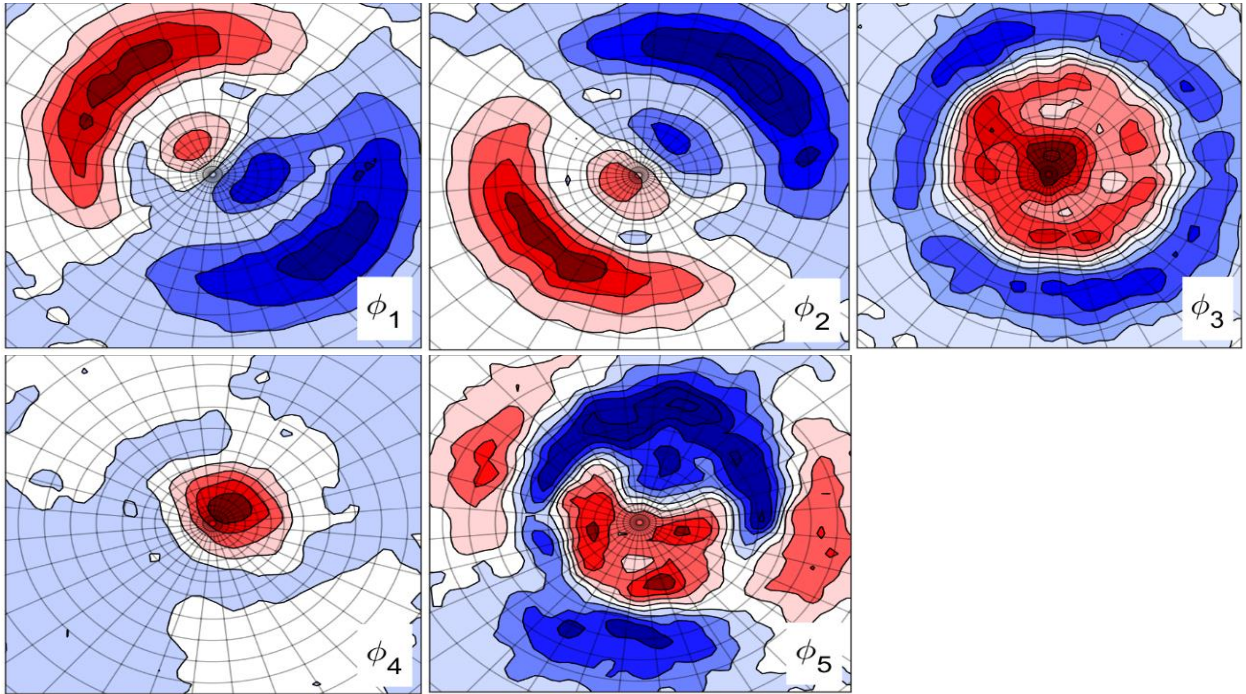


Figure 2. 20: First five POD modes of vorticity field with un-removed wandering for $S = 0.57$ at $h = 3.5 \text{ cm}$. Positive (negative) values of vorticity are shown in red (blue) color.

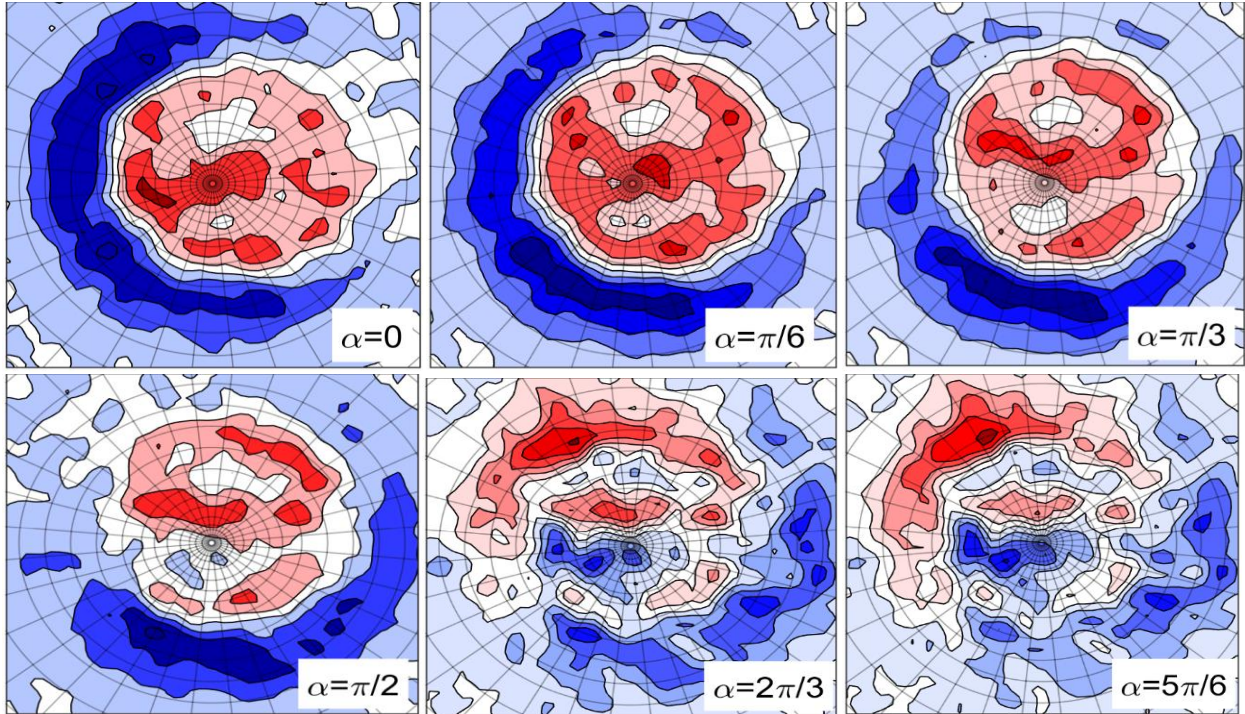


Figure 2. 21: D-POD mode 3, with un-removed wandering, for $S = 0.57$ and $h = 3.5 \text{ cm}$ at six different phase shifts (α), representing time-lag. Positive (negative) values of vorticity are shown in red (blue) color.

(b) $S = 0.57$. Figure 2.20 shows the first five POD modes of the vorticity field with un-removed wandering effects. Modes 1 and 2 are similar to what was observed for the synthetic vortex with a single spiral rotating around it (compare φ_1 and φ_2 in Figure 2.20 with Figure 2.9-a). Mode 4 shows a single vortex and mode 5 does not contain much coherency. Mode 3 is similar to what was observed for the synthetic vortex with variation in size (compare φ_3 in Figure 2.20 with φ_4 in Figure 2.7). It is therefore inferred that mode 3 corresponds to the size varying recirculation bubble of vortex breakdown, see also the flow visualization in Figure 2.1-b. Church [12] observed that the recirculation bubble has periodic vertical motion which can lead to the variation of vortex core size in the horizontal PIV plane. In short, for this swirl ratio $S = 0.57$, the flow is a combination between a spiral rotating around the recirculation bubble and a single vortex movement with variation in size. Indeed, the animated movie of the mode 3, obtained by D-POD, confirms this conclusion. Figure 2.21 shows D-POD mode 3 at $h = 3.5 \text{ cm}$. It shows that the single spiral (shown in blue) is winding around the bubble (shown in red) during $\alpha = 0$ to $\alpha = \pi/2$. Then, the coherency starts to disappear at $\alpha = 2\pi/3$ and $\alpha = 5\pi/6$ which is probably due to the periodic

vertical motion of the vortex. Note that when wandering effects are removed, the first POD mode 1 (see Section 6) shows a single vortex (or recirculation bubble) structure, suggesting that the single vortex, or the bubble, has the highest energy in the flow.

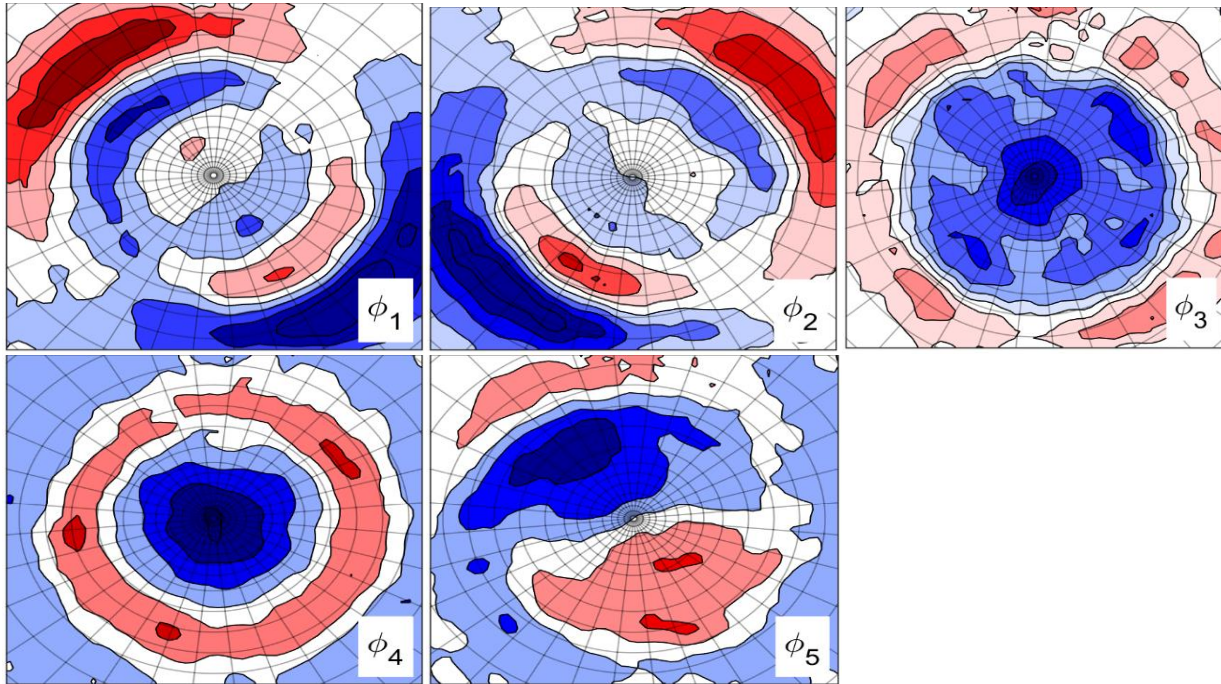


Figure 2. 22: First five POD modes of vorticity field with un-removed wandering for $S = 0.96$ at $h = 3.5 \text{ cm}$. Positive (negative) values of vorticity are shown in red (blue) color.

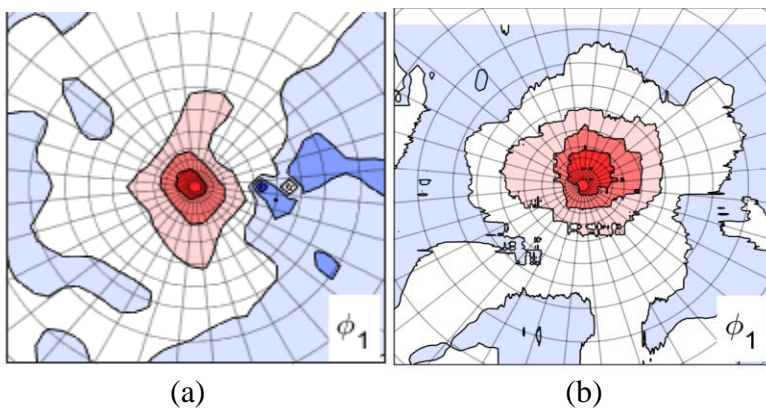


Figure 2. 23: The first POD mode of the vorticity field with removed wandering effects at $h = 3.5 \text{ cm}$ for (a) $S = 0.22$ and (b) $S = 0.57$. Positive (negative) values of vorticity are shown in red (blue) color.

(c) $S = 0.96$. Figure 2.22 shows the first five POD modes of the vorticity field with unreduced wandering effects. Modes 1 and 2 are similar to what was observed for the synthetic vortex with a double spiral rotating around it (compare φ_1 and φ_2 in Figure 2.22 with Figure 2.9-b). Modes 3 and 4 are similar to what observed for the synthetic vortex with variation in size (compare φ_3 and φ_4 in Figure 2.22 with φ_4 in Figure 2.7). These modes correspond to the recirculation bubble of vortex breakdown based on the same discussion provided for $S = 0.57$. Mode 5 is analogous to a single spiral vortex. It appears that for this swirl both a double spiral (modes 1 and 2) and a single spiral vortex (mode 5) are present in the flow with the double spiral dominating. This is confirmed by the streamline snapshots where one or two vortex structures are observed (see Section 6). In short, for this swirl ratio $S = 0.96$, the flow contains a single vortex, or recirculation bubble, with variation in size and a double or single spiral rotating around the bubble.

2.6 Summary and tornado-like vortex structure

In this section, we address the essential question raised at the beginning: what is the large-scale structure of the tornado-like vortex? We used the contours of the mean flow field and modal analysis to infer the configuration of the vortex shown in Figures 2.27 and 2.28. We also used the coherent structures extracted by POD at the different heights and time-frequency analysis of surface pressure fluctuations to reveal the evolutions of coherent structures. Note that due to low sampling frequency of PIV system, we applied time-frequency analysis (short-time Fourier transform) on the first POD mode of the surface panel pressure fluctuations; we first applied POD on the surface pressure fluctuations and then short-time Fourier transform is performed on principal component of the first POD mode.

For $S = 0.22$, the mean flow field shows a single vortex with convergent radial flow towards center. However, a divergent radial flow appears in the horizontal PIV planes at lower heights due to the vortex tilting. The modal analysis, or coherent structures extracted by POD, shows a single vortex subjected to wandering motion. This conclusion is confirmed also by the first POD mode applied on the corrected velocity field (removed wandering effects) representing a single vortex (Figure 2.23-a). Streamlines in a snapshot of the horizontal PIV plane also reveals a single vortex, shown in 24-a. Due to the absence of vortex breakdown at this swirl ratio, the coherent structures are quite persistent along the height and the flow looks laminar (see Figure 2.25-a). Time-frequency analysis (performed on the base pressure field) in Figure 2.26-a reveals that frequency

amplitudes are relatively constant in time and lie in the range of 0.1 and 4.5 Hz. The resulting schematics of the mean flow field and the vortex dynamics for $S = 0.22$ are shown in Figures 2.27-a and 2.28-a.

For $S = 0.57$, the mean flow field shows a recirculation bubble vortex breakdown accompanied with a divergent radial flow at the vortex center. The POD analysis shows a recirculation bubble with a single spiral rotating around it, which is rather similar to the synthetic vortex shown in Figure 2.3-b. Moreover, the coherent structures gradually disappear along the vortex height (see Figure 2.25-b) because of the presence of vortex breakdown. At this swirl ratio, a transition from single spiral to double spiral (or transition from one-cell to two-cell), resembling two intertwined sub-vortices, occurs, but it is very weak in terms of occurrences. Streamlines in a snapshot of the horizontal PIV plane revealing a double spiral pattern are shown in Figure 2.24-b. The number of snapshots showing double spiral is 9 out of 2018 snapshots, and the ensemble average distance between the two sub-vortices is 2.7 cm. This is also confirmed by the fact that when wandering effects are removed, the first POD mode shows a single vortex (Figure 2.23-b). Time-frequency analysis of the first POD mode of the surface pressures reveals the intermittency of the coherent structures in the low frequency range (Figure 2.26-b). The resulting schematics of the mean flow field and the coherent structures are shown in Figures 2.27-b and 2.28-b.

For $S = 0.96$, the mean flow field shows that the recirculation bubble is expanded into an annular form with a stagnant area (zero-value velocity) inside the core region. The modal analysis, or coherent structures extracted by POD, shows a recirculation bubble with a double spiral rotating around it. This structure refers also to two-cell structure and it is rather identical to the synthetic vortex shown in Figure 2.3-c. Rapid destruction of coherent structure along the vortex height can be observed because of the high turbulence in the flow (see Figure 2.25-c). Streamlines in a snapshot of the horizontal PIV plane for revealing double spiral pattern are shown in Figure 2.24-c. Double spiral occurs more often as the number of these snapshots is increased to 134 out of 2028 snapshots with the ensemble average distance of 6.2 cm between the two spirals. Indeed, time-frequency analysis of the first POD mode of the surface pressures (Figure 2.26-c) shows two intense frequency components: (i) one is restricted in the low-frequency range around 0.3 Hz which is relatively constant in time and (ii) an intermittent component concentrated around the

frequency 6.5 Hz. The resulting schematics of the mean flow field and the coherent structures are shown in Figures 2.27-c and 2.28-c.

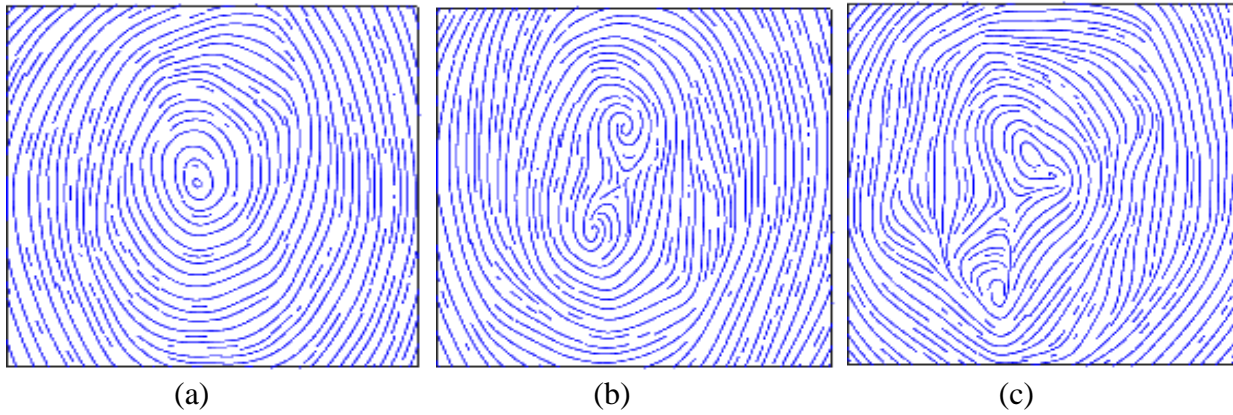
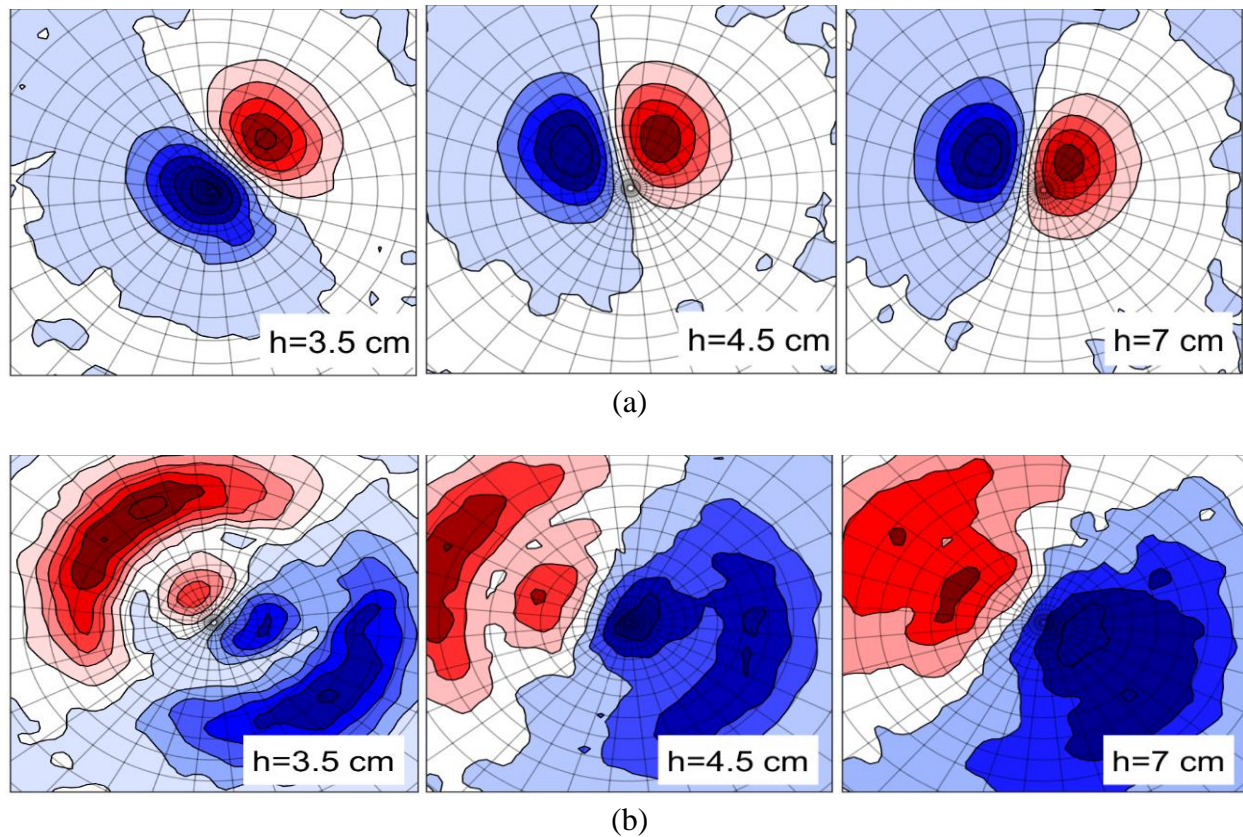


Figure 2. 24: Streamlines in a snapshot of the horizontal PIV plane at $h = 3.5$ cm for revealing (a) single-cell structure for $S = 0.22$, (b) double-cell structure for $S = 0.57$, and (c) double-cell structure for $S = 0.96$. Note that double-cell structure includes two co-rotating sub-vortices that are embedded in the fluctuating flow field.



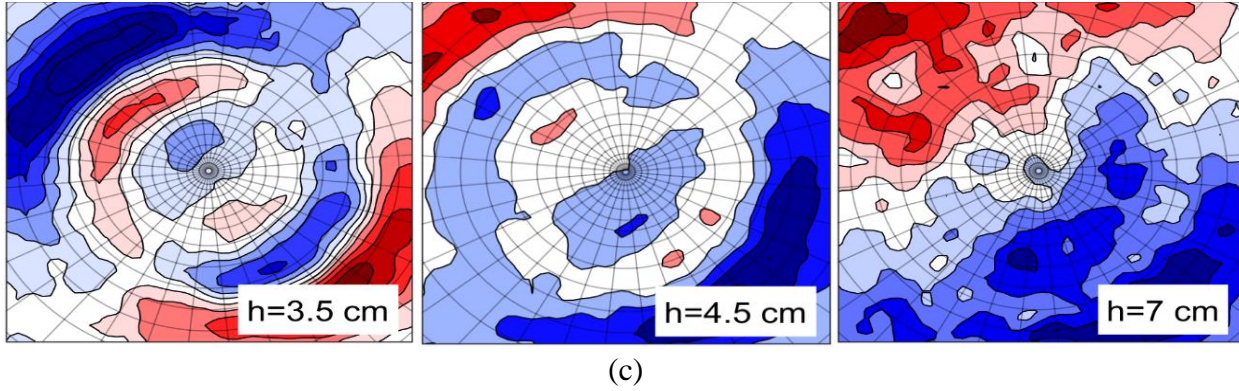


Figure 2.25: First POD mode of vorticity field with un-removed wandering at the different heights for (a) $S = 0.22$, (b) $S = 0.57$ and (c) $S = 0.96$. Positive (negative) values of vorticity are shown in red (blue) color.

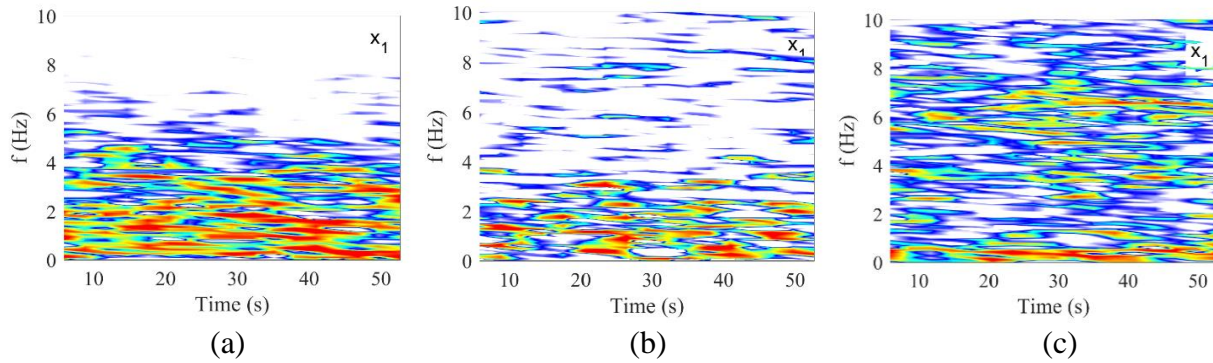


Figure 2.26: Time-frequency analysis (spectrogram) of the first POD mode of the surface pressure fluctuation for (a) $S = 0.22$, (b) $S = 0.57$ and (c) $S = 0.96$.

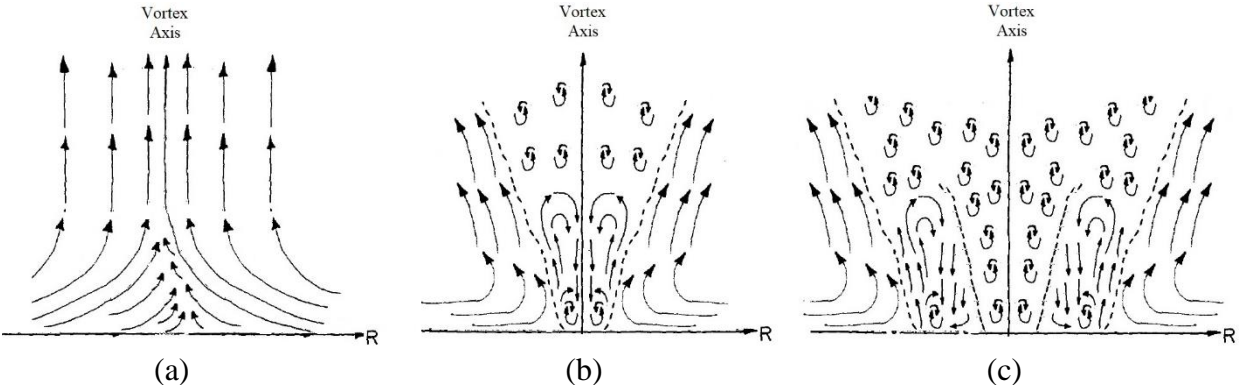


Figure 2.27: Schematic of the mean flow observed for the three swirl ratios (a) $S = 0.22$, (b) $S = 0.57$ and (c) $S = 0.96$.

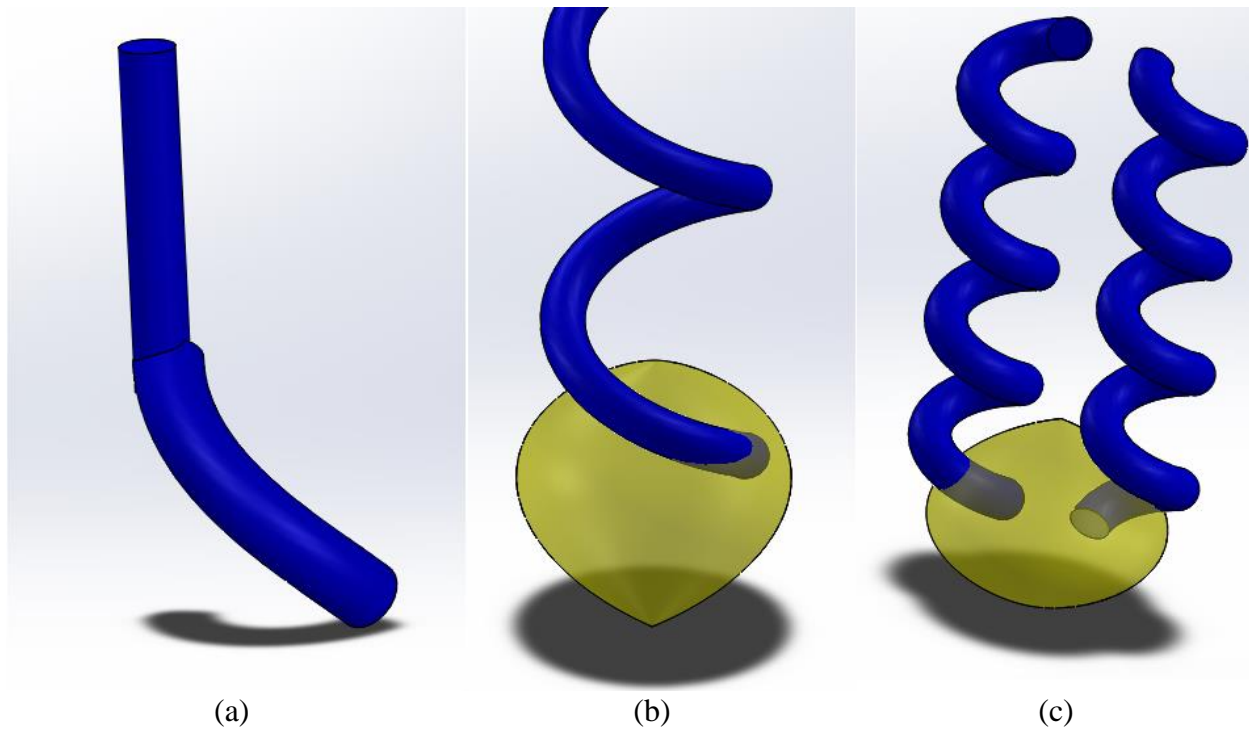


Figure 2. 28: Three-dimensional schematic of coherent structures inferred from modal analysis. (a) For $S = 0.22$, a single vortex with tilting at low heights (this structure refers to as single-cell), (b) for $S = 0.57$, a recirculation bubble (shown in yellow) with a single spiral behind the bubble, which still refers to as single-cell structure, and (c) for $S = 0.96$, a recirculation bubble with a double spiral behind the bubble, referring to as two-cell structure.

2.7 Conclusions

Many tornado chambers generate flows that reveal similar flow patterns and agree in general on the variations of the flow structures with swirl ratio. However, very little is known about the underlying physics of the flow. Herein, we applied POD on the fluctuating flow field to investigate the prominent mechanisms of tornado-like vortices for a range of swirl ratios ($0.22 \leq S \leq 0.96$). Moreover, a relative new Dynamic-POD analysis was used to provide the time evolutions of coherent structures. A synthetic vortex POD analysis was also conducted to help with the interpretation of the experimental results.

The results show that for $S = 0.22$, the flow contains a single vortex which is tilted at lower heights. For $S = 0.57$, the flow contains a recirculation bubble with a single spiral rotating around

it. Sometimes, transition from single spiral to double spiral (single-cell to two-cell) occurs, but its occurrence is very intermittent. By increasing swirl ratio further to $S = 0.96$, transition from single spiral to double spiral occurs more often.

Based on these results, the vortex structure is inferred for the range of Swirl ratios. This vortex structure can be further employed to generate an analytical model for the large-scale fluctuating flow field in tornado-like vortices.

As a final note, it is important to emphasize that tornado-like vortex has a highly sophisticated three-dimensional dynamical structure sensitive to boundary conditions. Categorizing vortex structure and its dynamic as such is obviously a drastic simplification. However, such simplified models can help extracting predominant underlying physical mechanisms that govern the dynamics of tornado-like vortex behaviour. Further detailed investigations on coherent structures and their dynamic characteristics are definitely necessary to foster the construction of low-dimensional models of tornado flows and the definition of wind-loads for design codes and standards.

References

- [1] M. Refan, H. Hangan, Near surface experimental exploration of tornado vortices, *J. Wind Enging Industrial Aerody* 175 (2018) 120–135.
- [2] M. Refan, H. Hangan, Characterization of tornado-like flow fields in a new model scale wind testing chamber, *J. Wind Enging Industrial Aerody*. 151 (2016)107–121.
- [3] A. Gairola, G. Bitsuamlak, Numerical tornado modeling for common interpretation of experimental simulators, *J. Wind Enging Industrial Aerody* 186 (2019) 32-48.
- [4] CS. Yih, Tornado-like flows, *Phys. Fluids* 19, 076601 (2007).
- [5] M. C. Jischke, M. Parang, Properties of Simulated Tornado-Like Vortices, . *J. Atmos. Sci.* 31 (1973) 506-512.
- [6] J. Wang, S. Cao, W. Pang, J. Cao, Experimental Study on Effects of Ground Roughness on Flow Characteristics of Tornado-Like Vortices, *Boundary-Layer Meteorology* 162 (2017) 319-339.

- [7] A. Razavi, W. Zhang, P. P. Sarkar, Effects of ground roughness on near-surface flow field of a tornado-like vortex, *Exp Fluids* (2018) 59: 170.
- [8] A. R. Mishra, D. L. James, C. W. Letchford, Physical simulation of a single-celled tornado-like vortex, Part A: Flow field characterization, *J. Wind Enging Industrial Aerody* 96 (2008) 1243-1257.
- [9] A. R. Mishra, D. L. James, C. W. Letchford, Physical simulation of a single-celled tornado-like vortex, Part B: Wind loading on a cubical model, *J. Wind Enging Industrial Aerody* 96 (2008) 1258-1273.
- [10] R. Ashton, M. Refan, G. V. Iungo, H. Hangan, Wandering corrections from PIV measurements of tornado-like vortices, *J. Wind Enging Industrial Aerody.* 189 (2019) 163-172.
- [11] A. M. Edstrand, T. B. Davis, P. J. Schmid, K. Taira, L. N. Cattafesta, On the mechanism of trailing vortex wandering, *J. Fluid Mech.* (2016) 801 R1-R11.
- [12] C. R. Church, J. T. Snow, G. L. Baker, E. M. Baker, E. M. Agee, Characteristics of tornado-like vortices as a function of swirl ratio: a laboratory investigation. *J. Atmos. Sci.* 36 (1979) 1755–1766.
- [13] J. H. Faler, S. Leibovich, Disrupted states of vortex flow and vortex breakdown, *The Physics of Fluids* 20, 1385 (1977).
- [14] P. HashemiTari, R. Gurka, H. Hangan, Experimental investigation of tornado-like vortex dynamics with swirl ratio: The mean and turbulent flow fields, *J. Wind Enging Industrial Aerodyn.* 98 (2010) 936–944.
- [15] J.L., Lumley, *Stochastic Tools in Turbulence*. Academic Press, New York 1970.
- [16] L. Sirovich, Turbulence and the dynamics of coherent structures, *Quarterly of Applied Mathematics*, 45 (3) (1987), 561-590.
- [17] G Berkooz, P. Holmes, J. L. Lumley, The proper orthogonal decomposition in the analysis of turbulent flows, *Annu. Rev. Fluid Mech.* 25 (1993) 539-575.

- [18] B. Podvina, Y. Fraigneau, A few thoughts on proper orthogonal decomposition in turbulence, *Physics of Fluids* 29 (2017) 020709.
- [19] P. Druault, J. Delville, Jean-Paul Bonnet, Proper Orthogonal Decomposition of the mixing layer flow into coherent structures and turbulent Gaussian fluctuations, *C. R. Mecanique* 333 (2005) 824-829.
- [20] E. Liberge, A. Hamdouni, Reduced order modelling method via proper orthogonal decomposition (POD) for flow around an oscillating cylinder, *Journal of Fluids and Structures* 26 (2010) 292–311.
- [21] M. Sieber, C. O. Paschereit, K. Oberleithner, Spectral proper orthogonal decomposition, *J. Fluid Mech.* 792 (2016) 798-828.
- [22] P. J. Schmid, Dynamic mode decomposition of numerical and experimental data, *J. Fluid Mech.* 656 (2010) 5–28.
- [23] A. Towne, O. T. Schmidt, T. Colonius, Spectral proper orthogonal decomposition and its relationship to dynamic mode decomposition and resolvent analysis, *J. Fluid Mech* 847 (2018) 821-867.
- [24] L. Carassale, M. Marre-Brunenghi, Statistical analysis of wind-induced pressure fields: A methodological perspective, *J. Wind Eng. Ind. Aerodyn.* 99 (2011) 700–710.
- [25] H. Hangan, M. Refan, C. Jubayer, D. Romanic, D. Parvu, J. Lotufo, A. Costache, Novel techniques in Wind Engineering, *J. Wind Enging Industrial Aerody* 171 (2017) 12-33.
- [26] A. L. Heyes, R. F. Jones, D. A. R. Smith, Wandering of wing-tip vortices. in *Proceedings of the 12th International Symposium on the Applications of Laser Techniques to Fluid Mechanics*, Lisbon, Portugal, 2004.
- [27] Jiang, M., Machiraju, R., Thompson, D., 2002. In: Ebert, D., Brunet, P., Navazo, I. (Eds.), *A Novel Approach to Vortex Core Region Detection*. The Eurographics Association, pp. 217–225.
- [28] G. V. Iungo, P. Skinner, G. Buresti, Correction of wandering smoothing effects on static measurements of a wing-tip vortex, *Exp Fluids* (2009) 46:435–452

- [29] David M. Birch, Self-similarity of trailing vortices, *Physics of Fluids* 24, 025105 (2012).
- [30] H. Hu, Z. Yang, P. Sarkar, Dynamic wind loads and wake characteristics of a wind turbine model in an atmospheric boundary layer wind, *Exp Fluids* (2012) 52:1277–1294.
- [31] S. J. Beresh, J. F. Henfling, and R. W. Spillers, Meander of a fin trailing vortex and the origin of its turbulence, *Exp Fluids* (2010) 49, 599–611.
- [32] L. Carassale, M. Marrè-Brunenghi, Identification of meaningful coherent structures in the wind-induced pressure on a prismatic body, *J. Wind Eng. Ind. Aerodyn.* 104–106 (2012) 216–226.
- [33] L. Carassale, G. Solari, F. Tubino, Proper orthogonal decomposition in wind engineering. Part 2: Theoretical aspects and some applications, *Wind and Structures*, Vol. 10, No. 2 (2007) 177-208.
- [34] L. Carassale, Analysis of aerodynamic pressure measurements by dynamic coherent structures, *Probabilistic Engineering Mechanics* 28 (2012) 66–74.
- [35] Z. Tang, C. Feng, L. Wu, D. Zuo, D. L. James, Characteristics of tornado-like vortices simulated in a large-scale ward-type simulator, *Boundary-Layer Meteorol* (2018) 166:327–350.

Chapter 3

3 Statistical and modal analysis of surface pressure fluctuations in tornado-like vortices

In the study of aerodynamic behavior of bluff bodies, a general technique is measurement of surface pressures. Due to its complex temporal and spatial features, modal analysis is an interesting tool to be used for interpretation and discussion. The most common technique for modal representation is proper orthogonal decomposition (POD), also refers to as principal component analysis (PCA). However, it's believed that POD sometimes fails to extract meaningful features of pressure field. To overcome this deficit, an advanced method independent component analysis (ICA) is applied. Furthermore, these two methods are generalized in the frequency domain, called dynamic POD and dynamic ICA, to provide the temporal evolutions of coherent structures over the spatial domain. A comparison between modal decomposition techniques and some common statistical techniques is also provided. Regardless of the reference to tornado-like vortices, the discussion of the present paper can be helpful in the physical interpretation of swirling flows in general.

3.1 Introduction

Measurement of surface pressures is a common technique in bluff-body aerodynamics as it provides a description of flow interaction with the body and an evaluation of wind-induced forces. Despite the accepted measurement techniques, the choice of processing tools for interpretation of the data is challenging as turbulent flow is usually characterized by complex variations in time and space. It is believed that there are well-correlated regions in the flow field, known as coherent structures, which provide insight into the turbulence. Despite the longstanding interest in coherent structure, its concept is still not consolidated and development of mathematical tools for their detection and extraction is difficult [1,2].

These mathematical tools are based on statistical properties and modal analysis. Modal representation is an efficient way to express the complex spatial and temporal variations of

turbulent flow as a combination of time-invariant distributions, called modes, modulated by scalar coefficients. In principle, the modal representations are infinite, but there are some requirements that may suggest some specific choices for the modes. In particular, it is desirable to adopt a modal representation that is synthetic, i.e. it should be able to represent the relevant features of the phenomenon using a small number of modes. Besides, it is best if the modes can be related to some physical phenomena so that the representation can be used as a support for qualitative interpretation and discussion. The definition of these two requirements is weak, depending on the metrics that is assumed by the analysts, as well as the features of the considered physical problem.

The most popular and probably the oldest technique for modal representation is proper orthogonal decomposition (POD), which is also referred to as covariance proper transformation, principal component analysis (PCA) or Karhunen–Loève expansion [3]. POD provides an optimum number of modes on the basis of their energy. The use of POD for extraction of coherent structures has been examined by several researchers [4-9], and the results are promising. However, the general opinion is that sometimes POD method fails to provide meaningful modes [10-12]. This failure is attributed mainly to two problems. (i) Ranking modes by their own energy might not be relevant in cases where weak or intermittent coherent structures exist [13-14]. Sieber et al. [14] showed that for a swirling jet flow, POD results in mixed coherent structures which do not represent distinct physical phenomena. (ii) Mode shapes are likely to be determined by the orthogonality constraint and thus may not be physically meaningful [10,15,16]. Carassale and Brunenghi [15] showed that POD suggests existence of a symmetric vortex shedding behind a prismatic body which is clearly non-physical.

To mitigate these problems associated to POD, the concept of independent component analysis (ICA) has been introduced for the interpretation of surface pressure field [15-18]. Its main difference with POD is that ICA exploits non-Gaussian structures and make them as independent as possible. Despite its widespread in several fields such as image recognition and signal processing, its application in fluid dynamics research area is very limited and its potentials are still unexplored [19]. Carassale and Brunenghi [19] studied wind pressure acting on a prismatic body and showed that ICA presents vortex shedding phenomenon independently on the two lateral faces of the model and thus avoids non-physical pattern obtained by POD. Gilliam et al. [17] applied ICA on the roof corner vortex of a low-rise building and showed its success over POD for

identification of the intermittent coherent structures. A weakness of ICA is ambiguity of the variances (energies) of the modes which makes the choice of mode order a challenging task. This issue is discussed in detail by Carassale and Brunenghi [15].

Both POD and ICA can be also generalized in the frequency domain, which respectively refers to as dynamic POD (D-POD) and dynamic ICA (D-ICA). D-POD is also known as spectral proper transformation [20,21]. These methods examine both temporal and spatial variations of pressure distribution and provide time evolution of coherent structures, also refers to as dynamic coherent structures. D-POD/D-ICA modes are completely uncorrelated for any time lag, while POD/ICA modes are only uncorrelated for zero-time lag which results in representation of the same physical phenomenon by different modes. The applications of these techniques in fluid mechanic problems are rare [19]. Sieber et al. [13] provides a comprehensive comparison between a somehow similar technique to D-POD (called spectral POD) and POD for three different problems. They showed that spectral POD is able to distinguish the coherent fluctuations from turbulent fluctuations in spite of their same energy content. On the other hand, Carassale and Brunenghi [19] showed that although D-POD modes provide information on the propagating pressure field, they are still limited by orthogonality and thus possibly associated to unrealistic physical phenomena.

Another alternative for extraction of dynamic coherent structures is dynamic mode decomposition (DMD) technique, introduced by Schmid [22]. In DMD, each mode has a single frequency and is ordered/arranged by its energy at that frequency, which is different from the energy ranking of POD. This technique has been applied on a variety of fluid mechanic problems and its advantages over POD method has been illustrated [23-26]. Muld et al. [27] showed that the advection of flow structures, represented by two POD modes, can be summarized in a single DMD mode. However, some researchers expressed their doubt on whether this method is suitable for the extraction of coherent structures in highly turbulent flows [13,14,28]. Due to the restrictions of modes to a single frequency, it fails to extract coherent structures that spread over a wide range of frequency [13].

The main objective of this article is applying these modal decomposition techniques for tornado-like vortex induced base pressures as well as comparing the extracted coherent structures from four modal decomposition techniques: (i) POD, (ii) ICA, (iii) D-POD and (iv) D-ICA. All the methods are applied to base surface pressure measurement which is a fundamental tool in the

experimental study of aerodynamic behavior of bluff bodies. To the authors' knowledge, the advanced ICA and D-ICA techniques have been applied only for a very simple case, i.e. a square-base prism in an atmospheric boundary layer flow [19]. On the other hand, the complex and rich nature of tornado-like vortices, in terms of the existence of different types of physical phenomena such as vortex wandering and vortex breakdown, can help us to indicate the capability and applicability of ICA or D-ICA. Moreover, the discussion presented here can be also helpful in the physical interpretation of the swirling flows, regardless of the reference to tornado-like vortices.

3.2 Experimental setup

The Wind Engineering, Energy and Environment (WinDEEE) Dome at Western University is the world's first three-dimensional and dynamic wind testing chamber that provides a novel technique to physically simulate various types of flow fields included tornadoes and downburst. A 1/11 scaled model of WinDEEE Dome (MWD) was built to reproduce and verify the characteristics of WinDEEE Dome. MWD uses 8 peripheral fans, except one wall that has an array of 4 rows×15 columns fans. MWD also uses 18 top fans similar to the peripheral ones. The schematic drawing of MWD is shown in Figure 3.1-a [29].

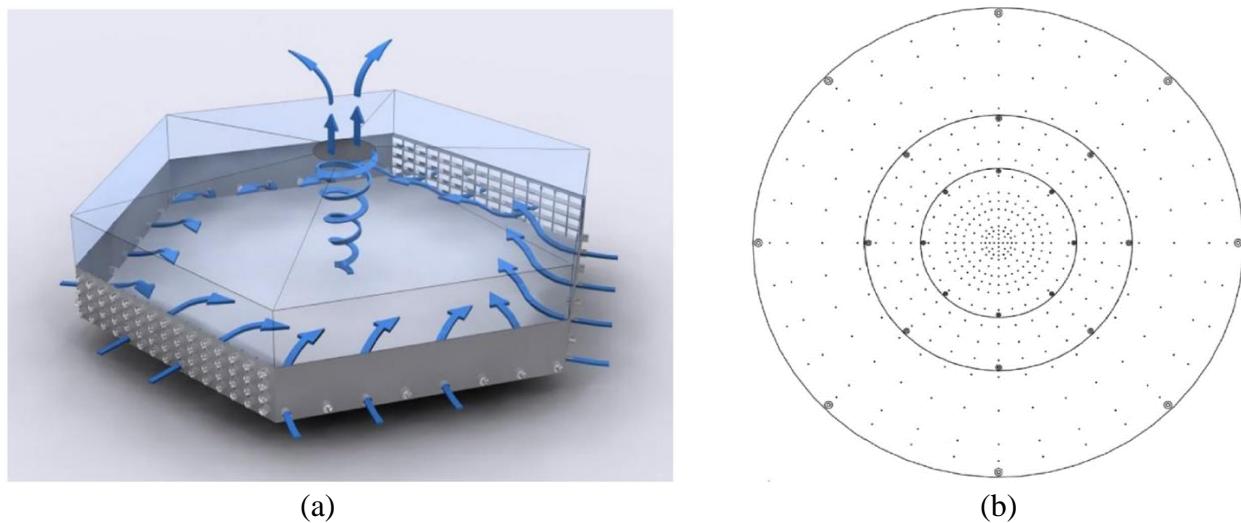


Figure 3. 1: (a) Schematic drawing of Mini-WinDEEE Dome (MWD) and (b) schematic of pressure taps arrangement over the surface panel. Obtained from Ref. [29].

In order to produce tornado vortices in MWD, top fans are used to extract the air from the hexagonal chamber. The inlet flow passes a set of guide vanes whose angles control the radial and tangential velocity components. As the inlet flow moves towards the center of the chamber, it is tilted in upward direction by the top fans. Then, the flow recirculates through a circuit where a honeycomb is installed to straighten the flow and eliminate the swirl produced by fans.

In MWD, the aspect ratio a , i.e. the ratio of inflow height to the updraft radius, is fixed and equal to 0.35. Note that the core radius and swirl ratio transition are independent from the aspect ratio [30,31]. Moreover, the radial Reynolds number (Re_r) is constant and equal to 6.7×10^4 . It was shown that the dynamic non-similarity between simulated and real tornadoes has negligible influence on results when $Re_r \geq 6.7 \times 10^4$ [29,31]. The main governing parameter is the swirl ratio which is defined as the ratio of tangential to radial velocity components at the inlet, $S = (1/2a) (V_{tan}/V_{rad}) = (1/2a) \tan\theta$, where θ is the vane angle with the normal direction to the sidewall.

Surface pressure fields provide new insights into wind loadings caused by tornado vortices. They are also fundamental tools for describing the flow fields as the velocity field measurement is challenging to measure near to the surface. The surface pressures have been measured with 413 static pressure taps distributed concentrically on a floor panel with a diameter of 56 cm, shown in Figure 3.1-b. The frequency of pressure signal collector is 700 Hz and the data are collected for a period of 60 s. Here, the pressure coefficients are normalized by the dynamic pressure calculated by average updraft velocity at the outlet. A maximum error of 1.17% is estimated for surface panel measurements. For more details of the experimental set-up please refer to Ref. [29].

The random motion of the vortex (wandering phenomenon) can lead to large errors in evaluating the mean pressure field. Thus, it is necessary to remove the effects of wandering from the surface pressure field data. Herein, we removed the wandering effects by detecting the vortex center via finding minimum pressure. Then, the vortex domain is shifted to the geometric center using an interpolation procedure.

3.3 Mathematical description of modal decomposition techniques

This section describes the formulations of POD, ICA, D-POD and D-ICA for extraction of the coherent structures from the surface pressure field fluctuations. The surface pressure field in different locations and time are collected into a vector $\mathbf{q}(t) \in \mathbb{R}^N$ ($N = 413$) with zero-mean value as we want to investigate the fluctuations. It's assumed that $\mathbf{q}(t)$ is statistically stationary and ergodic so that statistical properties can be estimated by time averaging.

3.3.1 Proper Orthogonal Decomposition (POD)

Let $\mathbf{C}_{\mathbf{q}\mathbf{q}}$ be the zero-time-lag covariance matrix estimated from the data as [32]:

$$\mathbf{C}_{\mathbf{q}\mathbf{q}} = E[\mathbf{q}(t)\mathbf{q}(t)^T] \cong \frac{1}{N} \sum_{t=1}^{N_t} \mathbf{q}(t)\mathbf{q}(t)^T \quad (3.1)$$

where $E[.]$ is statistical expectation which is implemented as a temporal average. According to POD, $\mathbf{q}(t)$ is represented by the modal expansion:

$$\mathbf{q}(t) = \sum_{k=1}^N \boldsymbol{\phi}_k x_k(t) = \boldsymbol{\Phi} \mathbf{x}(t) \quad (3.2)$$

where the vectors $\boldsymbol{\phi}_k \in \mathbb{R}^N$ ($k = 1, \dots, N$) are the eigenvectors of $\mathbf{C}_{\mathbf{q}\mathbf{q}}$, i.e. the solutions of the eigenvalue problem:

$$\mathbf{C}_{\mathbf{q}\mathbf{q}} \boldsymbol{\phi}_k = \lambda_k \boldsymbol{\phi}_k \quad (k = 1, \dots, N) \quad (3.3)$$

The eigenvectors are conventionally normalized to have unit norm and are assembled column-wise to build the matrix $\boldsymbol{\Phi}$. The coefficients x_k are the Principal Components (PC) of the process and are assembled in the vector $\mathbf{x} = [x_1, x_2, \dots, x_N]^T$. The cumulated energy can be defined as: $E = \sum_{k=1}^n \lambda_k / \sum_{k=1}^N \lambda_k$. The eigenvectors and the PCs are enumerated in such a way that their corresponding eigenvalues λ_k are sorted in decreasing order.

3.3.2 Independent Component Analysis (ICA)

Let us assume that the random fluctuation of the pressure field is provided by a generative model of the kind:

$$\mathbf{q}(t) = \mathbf{A} \mathbf{s}(t) \quad (3.4)$$

where \mathbf{s} is a vector of $n \leq N$ statistically independent sources s_k ($k = 1, \dots, n$) said Independent Components (IC) and \mathbf{A} is an $N \times n$ full-rank matrix referred to as mixing matrix. The target of ICA is the estimation of the sources \mathbf{s} and the mixing matrix \mathbf{A} , given the experimental measurements \mathbf{q} . It is clear that the ICA model (Eq. 3.4) is analogous to the representation formula offered by POD (Eq. 3.2), with the difference that the columns \mathbf{a}_k of the matrix \mathbf{A} are, in general, non-orthogonal and that the ICs s_k are now statistically independent (instead of simply uncorrelated like the PCs x_k).

The problem of estimating \mathbf{s} and \mathbf{A} from \mathbf{q} is indetermination since, as it is clear from the structure of Eq. (3.4), any permutation and scaling of the ICs can be compensated by a suitable permutation and scaling of the columns of \mathbf{A} . In order to remove such an indetermination, it is assumed that the ICs have unit variance and that are enumerated by sorting the norms of the corresponding columns of \mathbf{A} in decreasing order.

The estimation of \mathbf{s} and \mathbf{A} can be carried out by algebraic or iterative methods based on different principles including maximum likelihood, mutual information minimization, and non-Gaussianity maximization [33,34]. In this paper, the latter principle is adopted and is implemented through the fastICA algorithm [34].

The choice of the model order, i.e. the number of independent sources to be estimated, is often complicated. No general approaches for the model order selection are presently available, but some guidelines have been discussed in [15].

3.3.3 Dynamic-Proper Orthogonal Decomposition (D-POD)

A limitation of POD, as well as ICA, is implicit in their definition, which is based on a static mixing. The modes are constant in time, thus if a coherent structure has a time evolution, more than one mode may be necessary for its representation. It is the case, for example, of coherent pressure distribution that translate due to the advection produced by the main flow. A general way to overcome this limitation is to generalize the static mixture represented by Eq. (3.2) into a convolutive mixture

$$\mathbf{q}(t) = \int_0^t \mathbf{\Phi}(\tau) \mathbf{x}(t - \tau) d\tau \quad (3.5)$$

in which the mixing matrix Φ depends on the time lag τ and has the role of impulse response function. In Eq. (3.5), Φ is defined according to D-POD, the PC $x_j(t)$ are mutually uncorrelated for any time lag τ .

If the modal representation is exploited to extract coherent structures, the use of Eq. (3.5) is not practical and it is preferred to translate it in the frequency domain as:

$$\hat{\mathbf{q}}(f_c) = \hat{\Phi}(f_c) \hat{\mathbf{x}}(f_c) \quad (3.6)$$

where the symbol $\hat{\cdot}$ represents the Fourier transform and f_c is the circular frequency. In the frequency domain, D-POD is formally a static mixing (different for each frequency) and the mixing matrix $\hat{\Phi}$ may be interpreted as a frequency response function.

Modes obtained by D-POD are complex valued, thus represent pressure distributions characterized by amplitude and phase. To overcome the difficulty of visualization and physical interpretation, the complex modes can be represented as a sequence of real modes defined as [15,19]:

$$\bar{\Phi}_k(f_c, \alpha) = \text{Re}[\hat{\Phi}_k(f_c) e^{i\alpha}] \quad (3.7)$$

where α is a phase shift common to all the vector components, which can also be related to the time-lag $\tau = \alpha/f_c$.

3.3.4 Dynamic-Independent Component Analysis (D-ICA)

D-ICA can be generalized to the dynamic representation ICA following the same procedure applied for the time-domain D-POD. Accordingly, the analytic signal obtained by the given signal filtered in the neighborhood of f_c is represented as:

$$\tilde{\mathbf{q}}_{f_c}(t) = \hat{\mathbf{A}}(f_c) \mathbf{s}_{f_c}(t) \quad (3.8)$$

The complex-valued mixing matrix $\hat{\mathbf{A}}(f_c)$ can be obtained for each frequency band of interest using the complex generalization of static ICA algorithms. In this paper, like for the static case, the fastICA algorithm is adopted.

Likewise, for D-POD, the modes obtained by D-ICA are complex and represent pressure distributions characterized by amplitude and phase. To simplify representation and interpretation, the complex modes can be translated into a sequence of real modes defined as:

$$\bar{\mathbf{a}}_k(f_c, \alpha) = \text{Re}[\hat{\mathbf{a}}_k(f_c) e^{i\alpha}] \quad (3.9)$$

3.4 Modal representation of a simulated synthetic vortex

In this section, we investigated the relationship between POD modes and physical mechanism in tornado-like vortices. We simulated a synthetic vortex with two different simulation cases: (i) the vortex is subjected to a random Gaussian motion while its size remain fixed, and (ii) the vortex is subjected to a random Gaussian motion while its size is changing periodically. The mean pressure field of the synthetic vortex is shown in Figure 3.2.

To apply POD/ICA, we first remove the mean component and then compute the modes. Figure 3.3 shows the first five POD modes. The first two dipole modes correspond to the wandering motion and the third mode is a single vortex. The modes 4 and 5 are not physically meaningful. Figure 3.4 shows the ICA modes extracted from the data space defined by the first five POD modes. ICA modes 1, 2, 3 and 5 correspond to the POD modes 1 and 2 and thus represent the wandering motion. ICA mode 4 somehow corresponds to POD mode 3. The comparison between POD and ICA modes suggests that ICA removes the non-physical POD modes 4 and 5 and thus provides a closer physical description of the pressure field.

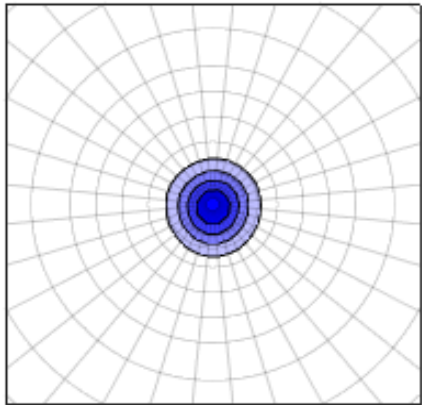


Figure 3. 2: A bivariate Gaussian synthetic vortex with variation in size and random wandering around the geometric center.

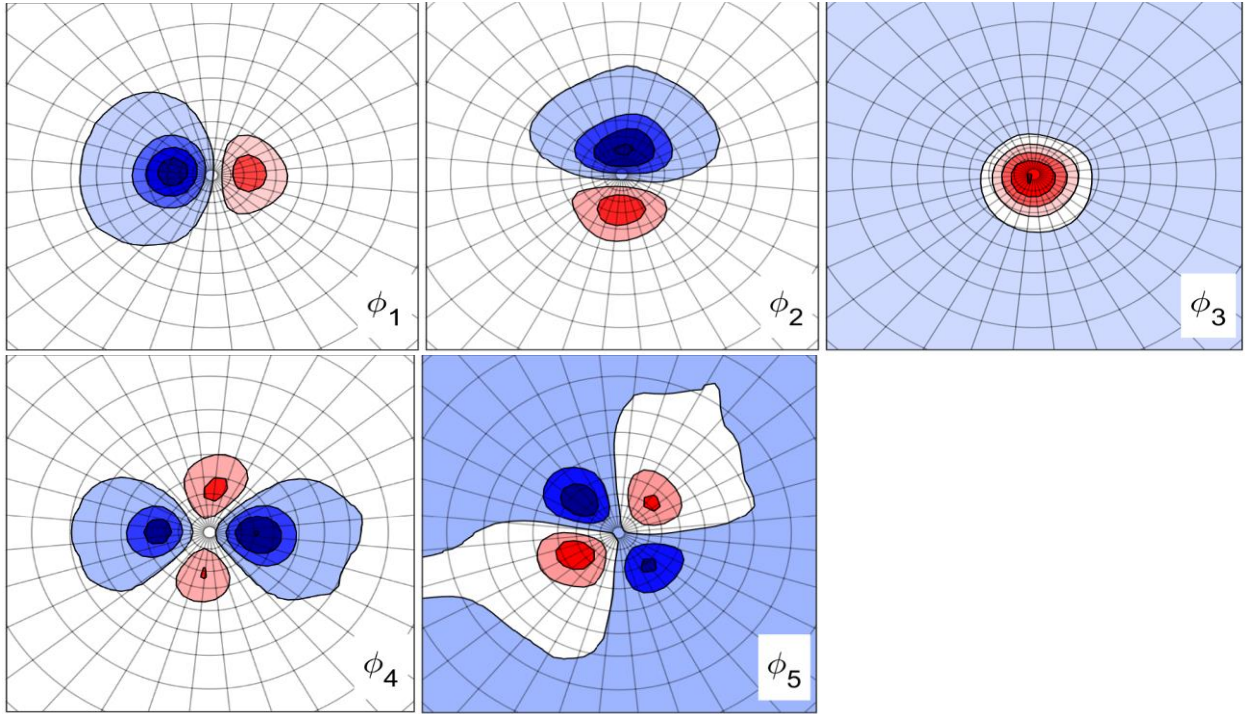


Figure 3. 3: The first five POD modes of the idealized (synthetic) vortex with Gaussian random wandering motion.

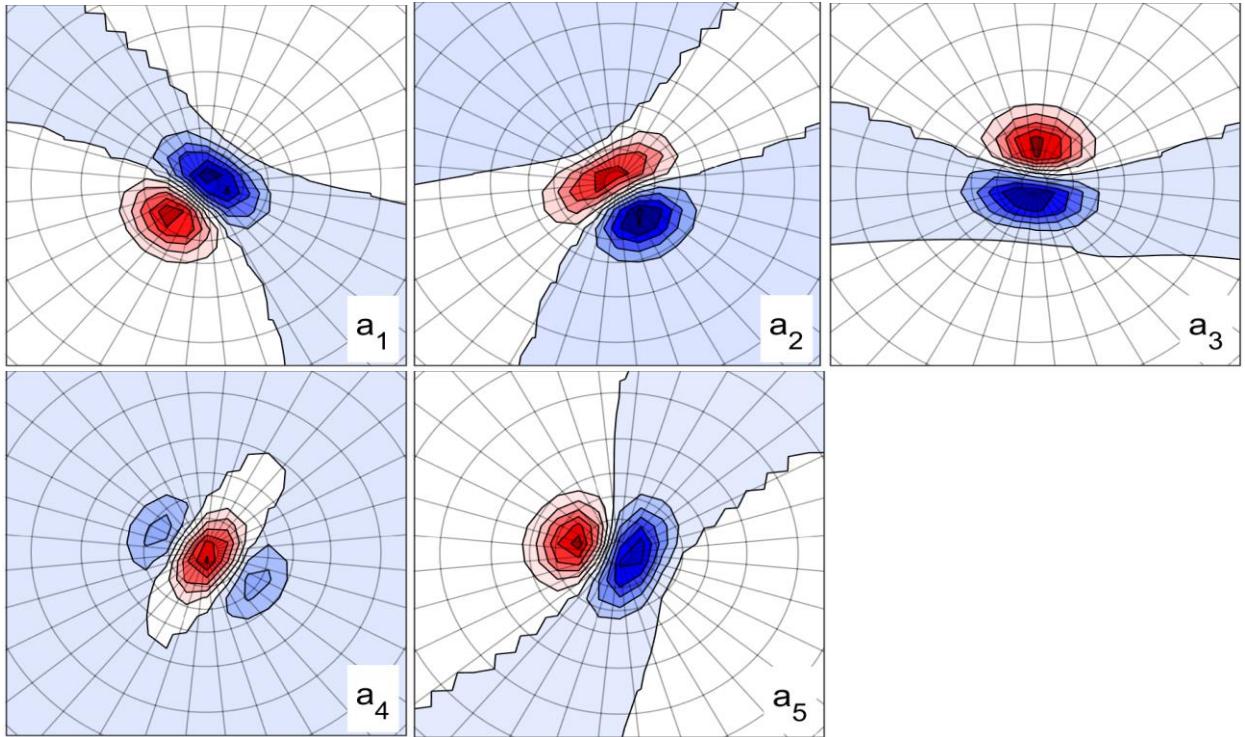


Figure 3. 4: The ICA modes extracted from the data space defined from the first six POD modes applied on the synthetic vortex. Positive (negative) values of pressure are shown in red (blue).

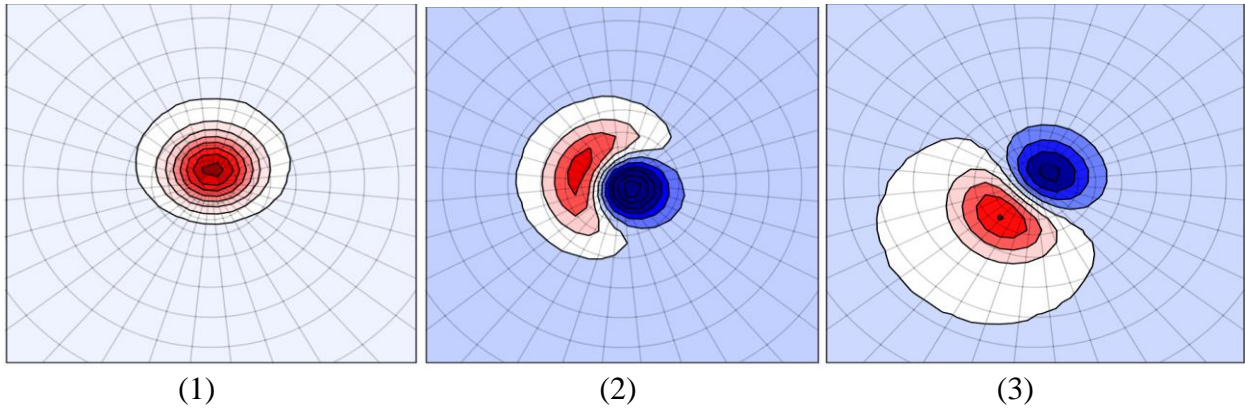


Figure 3. 5: Time history of fluctuating pressure field of the simulated vortex with Gaussian random wandering plus a size variation. Positive (negative) values of pressure are shown in red (blue) color.

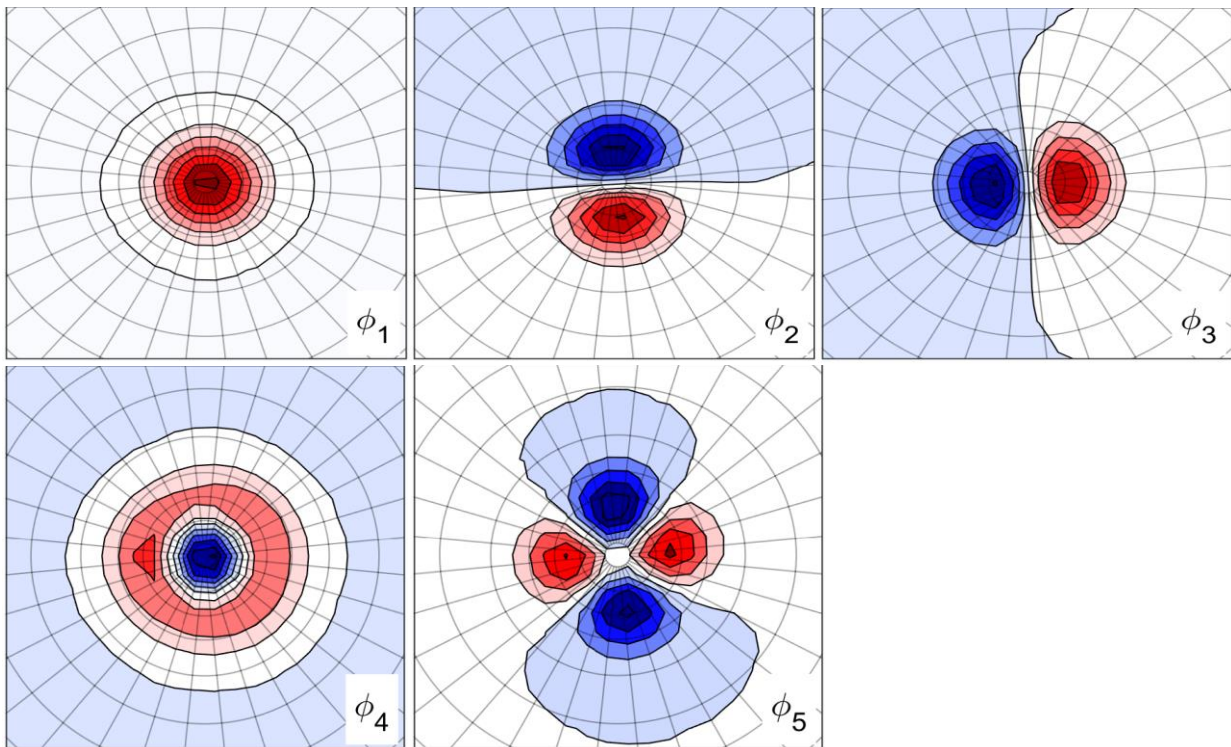


Figure 3. 6: The first five POD modes of the idealized (synthetic) vortex with Gaussian random wandering motion.

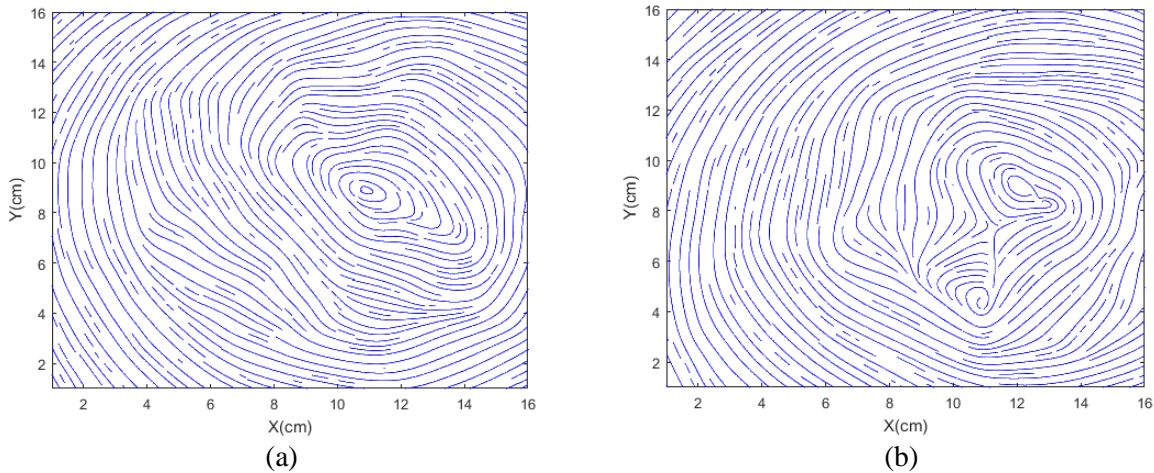


Figure 3. 7: Streamlines in two different snapshots of horizontal PIV plane for $S = 0.96$ revealing the presence of both (a) single-cell structure and (b) double-cell structure. Obtained from Ref. [36].

In the second simulation case, we vary the vortex size periodically while it is subjected to a random Gaussian motion. Figure 3.5 shows the time history of the fluctuating pressure field of the synthetic vortex. In the snapshot 1, the pressure field consists of a single vortex and then it is transformed into a dipole shape in the snapshots 2-3. Figure 3.6 shows the first five POD modes. Mode 1 consists of a single; its representation will be discussed in Section 5.2.2. Modes 2 and 3 are dipole and represent wandering motion. Mode 4 corresponds to size variation of the vortex, and mode 5 is not physically meaningful and is due to the orthogonality constraint embedded in POD.

Modal representation of the simulated synthetic vortex will assist understanding the relationship between the main mechanism of the tornado-like vortices and POD modes. In the next section, we apply modal decomposition on the fluctuating surface pressure field of the MWD experiment.

3.5 Analysis of experimental flow field

The structure of tornado-like vortex is highly dependent on the swirl ratio (S). Here, we selected three different swirl ratios ($S = 0.22, 0.57$ and 0.96) due to the existence of different vortex structures [29,35,36].

The vortex structure demonstrated based on the velocity and vorticity fields analysis in [36] is briefly summarized herein. For $S = 0.22$, the vortex structure is single-cell, and it is subjected to

intensified wandering motion. For $S = 0.57$, a recirculation bubble vortex breakdown occurs, and a single spiral is developed behind the bubble. When swirl ratio is increased to $S = 0.96$, an intermittent transition from single spiral to double spiral behind the bubble occurs. This is also referred to as transition from single-cell to double-cell structures. Figure 3.7 shows the presence of both single-cell and double-cell structures at different time snapshots in the horizontal PIV plane, see Ref. [36] for more information about coherent structures in tornado-like vortices. Here, we aim to extract these patterns out of surface pressure fluctuations using modal analysis.

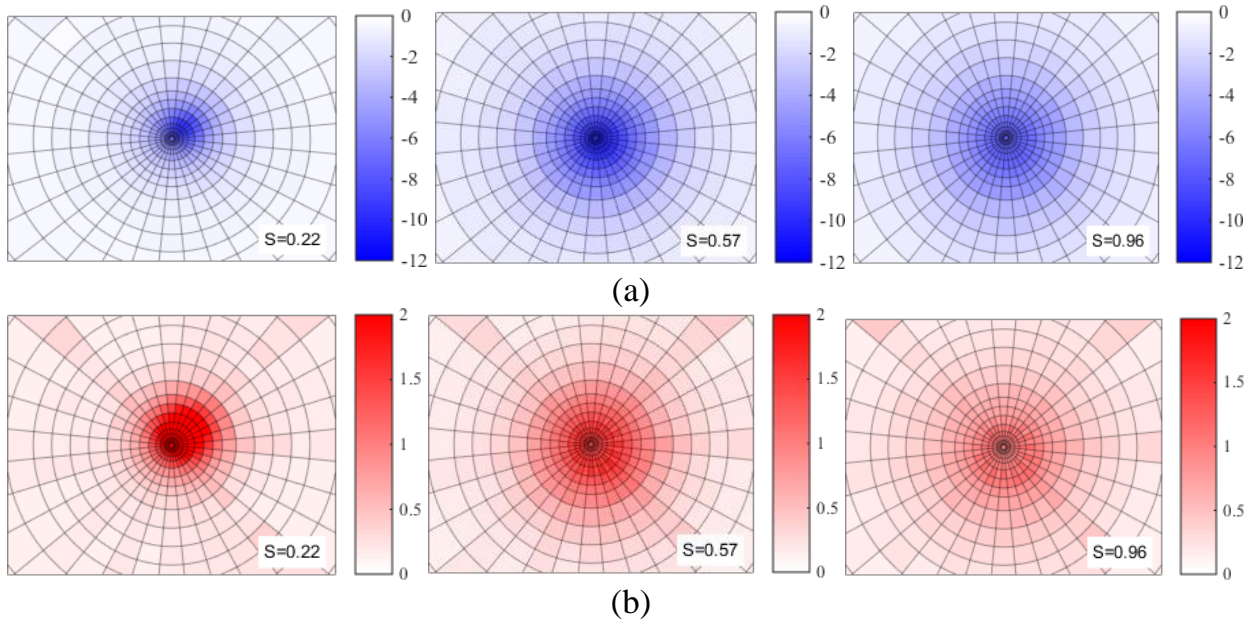


Figure 3. 8: (a) Mean and (b) standard deviation of the normalized surface pressure field. Wandering effects are not removed.

3.5.1 Basic statistical analyses

Figure 3.8-a shows the mean value and the standard deviation of the normalized pressure field; wandering effects are not removed. For $S = 0.22$, the location of minimum pressure deficit is not on the geometric center of the test area. When the swirl ratio increases to $S = 0.57$, the location of minimum pressure shifts to the geometric center. Besides, the intensity of pressure deficit is expanding as the swirl ratio increases from 0.22 to 0.57, while, afterwards (for $S = 0.96$), it is reduced due to the transition from single-cell to double-cell structure [35,36]. A similar comment

applies to the intensity of the pressure fluctuation in Figure 3.8-b, expressed in terms of standard deviation.

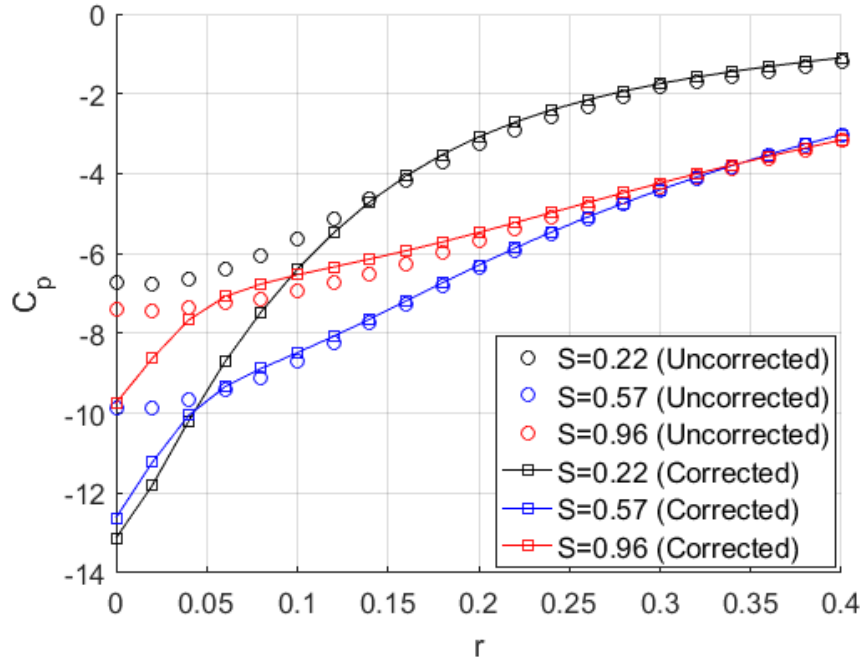


Figure 3. 9: Radial profile of mean surface pressure deficit for removed (corrected) and un-removed (uncorrected) wandering effects, (a) $S = 0.22$, (b) $S = 0.57$ and (c) $S = 0.96$. Radius (r) is normalized with updraft radius.

Figure 3.9 provides a comparison between corrected (removed-wandering) and un-corrected (unremoved-wandering) mean surface pressure field. For $S = 0.22$, the effects of vortex wandering motion is significant as it results in increase of minimum pressure deficit at center from -6.7 to -13.1. However, by increasing swirl ratio further ($S = 0.57$ and 0.96), the effects of wandering motion on the surface pressure field is reduced. Here, the pressure coefficients (C_p) are normalized by the dynamic pressure calculated by average updraft velocity at the outlet, which is remained constant for the different swirl ratios [29].

Figure 3.10 shows power spectral density of pressure field fluctuations for the three considered swirl ratios and three values of radial position. The spectral values reported are averaged in the circumferential direction. For $S = 0.22$ (a), the wide-band power content in the range $0 < f < 5$ Hz is interpreted as a consequence of intense vortex wandering. The variance, i.e. the area under

the curve, reduces along the radius ($S_{P,r=0.025} > S_{P,r=0.15}$). When the swirl ratio is increased to $S = 0.57$ (b), the frequency peaks become restricted to low frequencies; however, the variance at $r = 0.15$ is higher than that of $r = 0.025$ ($S_{P,r=0.025} < S_{P,r=0.15}$). This suggests the expansion of vortex core at the swirl ratio, $S = 0.57$. By increasing the swirl ratio further ($S = 0.96$) (c), some spectral peaks appear in a higher range of frequencies when $r = 0.025$ which are due to the transition in the structure of vortex. However, these evolutions in the vortex structure cannot be clearly understood through statistical analysis alone, i.e. mean, standard deviation and spectral analysis.

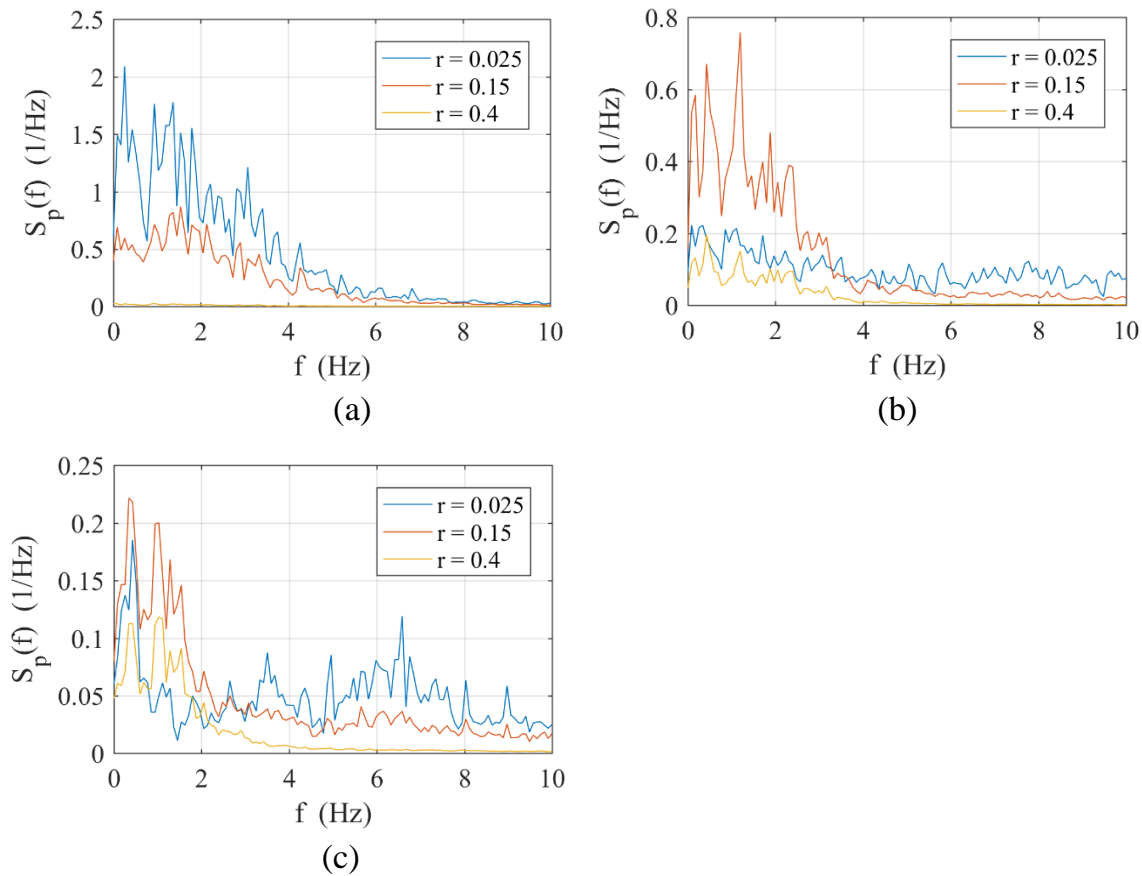


Figure 3. 10: Power spectral density along the radius for (a) $S = 0.22$, (b) $S = 0.57$ and (c) $S = 0.96$. Wandering effects are not removed. r is normalized with updraft radius. Note that the core radius (r_c) for the three swirl ratios (a-c) are respectively $r_c = 0.14, 0.32$, and 0.45 .

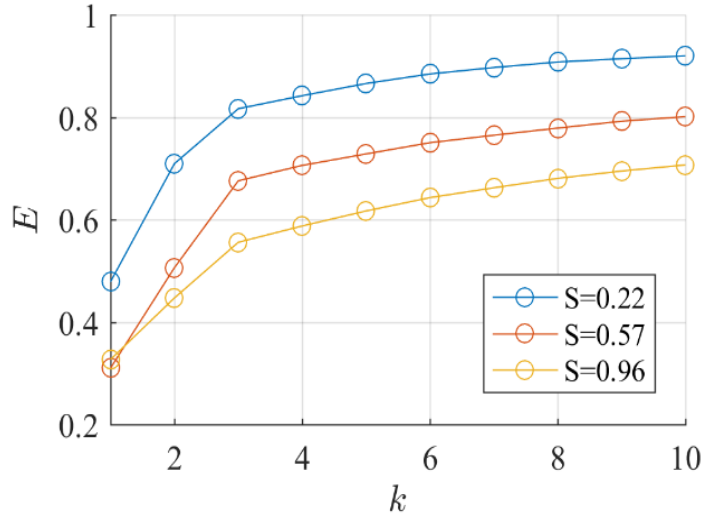


Figure 3. 11: Cumulated energy of POD modes.

3.5.2 Modal representation of the surface pressure fluctuations

Figure 3.11 shows the ratio of cumulated energy of the POD modes of the surface pressure. The first three POD modes contribute the most to the total energy, while the subsequent modes have quite comparable effects. To represent the 90% of the total energy, it is necessary to include at least 60 modes. The modes corresponding to $S = 0.22$ deliver a ratio of energy that is higher than for other values of swirl ratio, which is due to the large fluctuations due to vortex wandering. Large contribution of the first few modes implies that we can characterize the large-scale fluctuations of the pressure field by looking into only five POD modes.

3.5.2.1. Modal analysis for swirl ratio 0.22

Figure 3.12 shows the first five POD modes of the surface pressure for $S = 0.22$. Negative (positive) values of surface pressure are shown in blue (red) color. Dipole-type modes 1 and 2 represent the wandering motion of the vortex. It is interesting that the distance between dipoles is around 2.9 cm which is very close to the vortex core radius observed in the PIV experiment [36]. Mode 3 shows a single vortex and modes 4 and 5 are due to the orthogonality constraint embedded in POD and thus are not physically meaningful.

Figure 3.13 shows the ICA modes that are extracted from the data space defined by the first five POD modes. The number associated to the ICA modes, unlike POD modes, \mathbf{a}_k ($k = 1, \dots, 5$) is not meaningful since it is determined by the initialization of the algorithm. Modes 1, 2, 3 and 4 correspond to the wandering motion of the vortex and mode 5 represents a single vortex. This last mode does not show a centered vortex but rather the interpretation is that the vortex has a pronounced bend near the surface which was also observed by Church et. al. [30] and commented in Ref. [36] for this low Swirl. Note that non-physical POD modes 4 and 5 are removed by ICA.

Figure 3.14 shows the power spectral density of the POD/ICA modes. For POD modes, or principal components in Figure 3.14-a, mode 1 has a wide band frequency roughly between 0.25 and 5 Hz. Mode 2 has one dominant frequency at 1.36 Hz, and mode 3 has a wide band frequency in the range $0 < f < 2$ Hz. Modes 4 and 5 have noise-like distributions without dominant frequency peaks. For ICA modes, independent components in Figure 3.14-b, modes 1 and 2 as well as modes 3 and 4 have a broad band frequency between 0.25 and 5 Hz; modes 1 and 2 have also a dominant frequency peak around 1.36 Hz. Mode 5 has a wide band frequency in the range $0 < f < 2$ Hz.

Spectral analysis shows that modes having the same circumferential shape tend to have similar spectral distribution. This identity, for instance, between dipole POD modes 1 and 2 is shown in Figure 3.15. The coherence function between x_1 and x_2 is very high (around 0.8), while the coherence function between other pairs are smaller. Moreover, the phase angle between x_1 and x_2 is $-\pi/2$, suggesting that modes 1 and 2 are rotating around each other. This rotation is also observable in the animated movie of D-ICA dipole mode $\bar{\mathbf{a}}_2$ in Figure 3.16. While the dipoles are rotating around each other at the different phase shifts, they have a global rotation toward the first quartile, and this global rotation is correlated with the location of minimum pressure deficit in the mean pressure field, see Figure 3.8-a.

Briefly, for swirl ratio $S = 0.22$, the pressure field is characterized by a vortex which is subjected to Gaussian random wandering, and spectral analysis shows that wandering motion has a broad band frequency between 0.25 and 5 Hz.

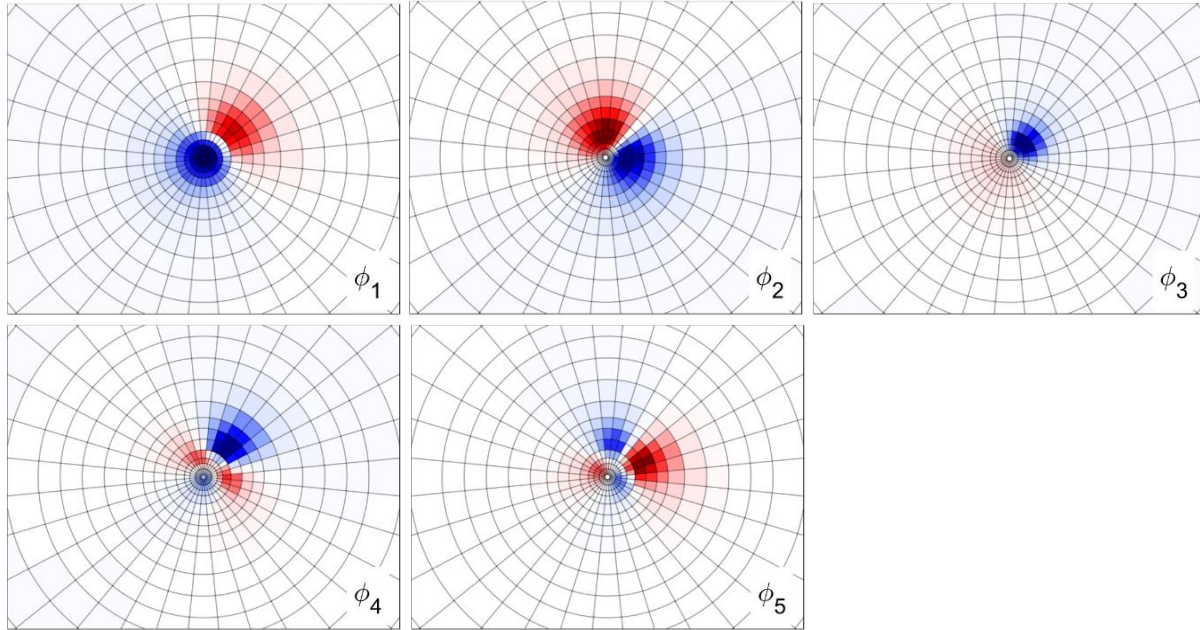


Figure 3.12: The first five POD modes of surface pressure for $S = 0.22$. Positive (negative) values of surface pressure are shown in red (blue). Wandering effects are not removed.

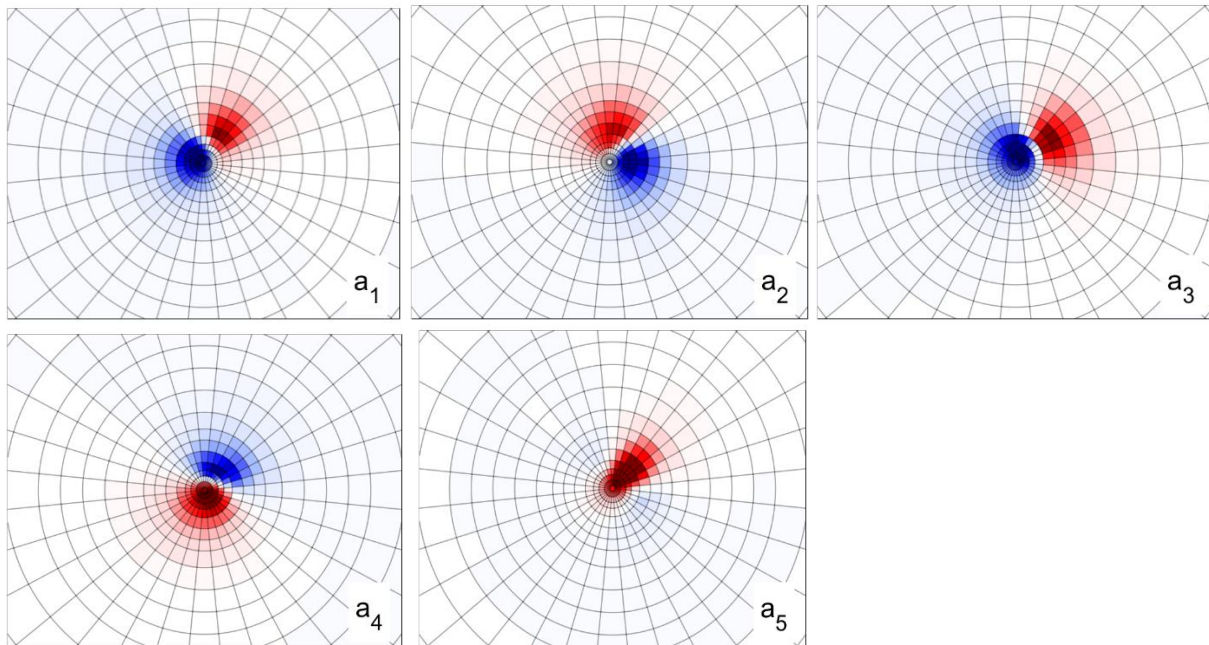


Figure 3.13: ICA modes extracted from the data space defined from the first five POD modes for $S = 0.22$. Positive (negative) values of surface pressure are shown in red (blue). Wandering effects are not removed.

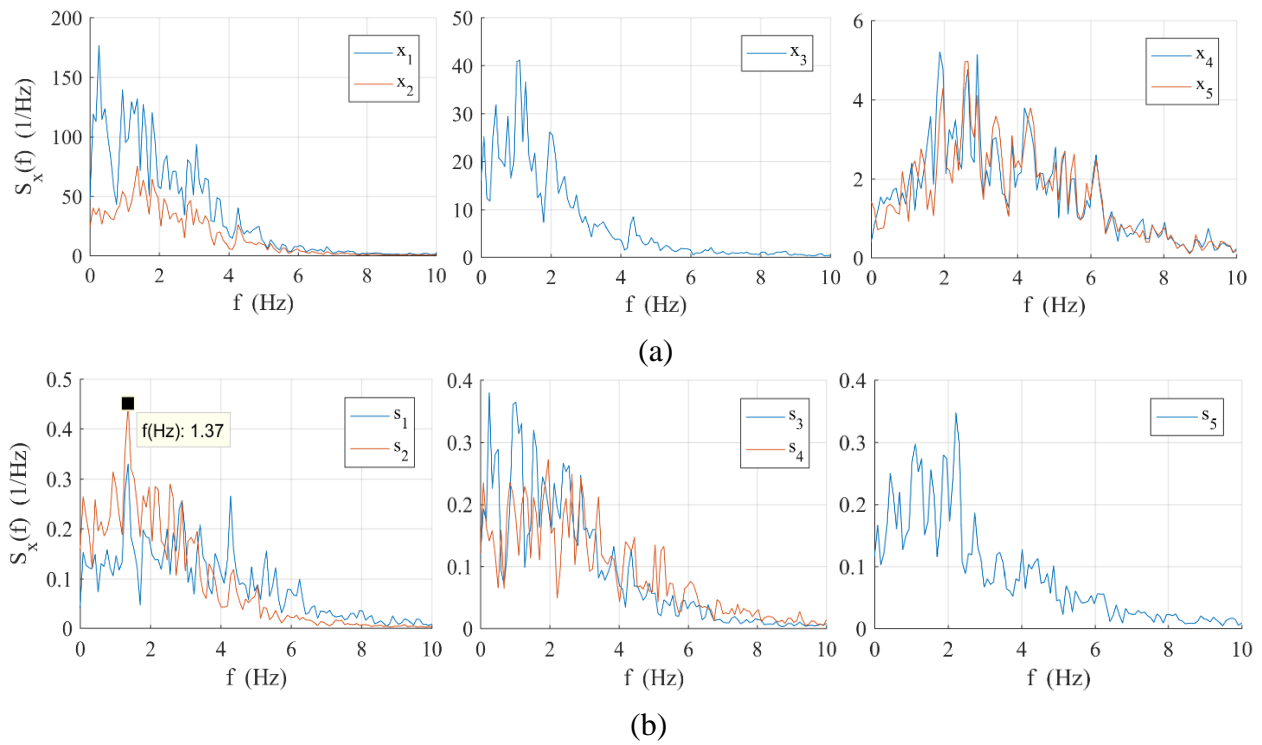


Figure 3. 14: Power spectral density of (a) PCs and (b) ICs for $S = 0.22$.

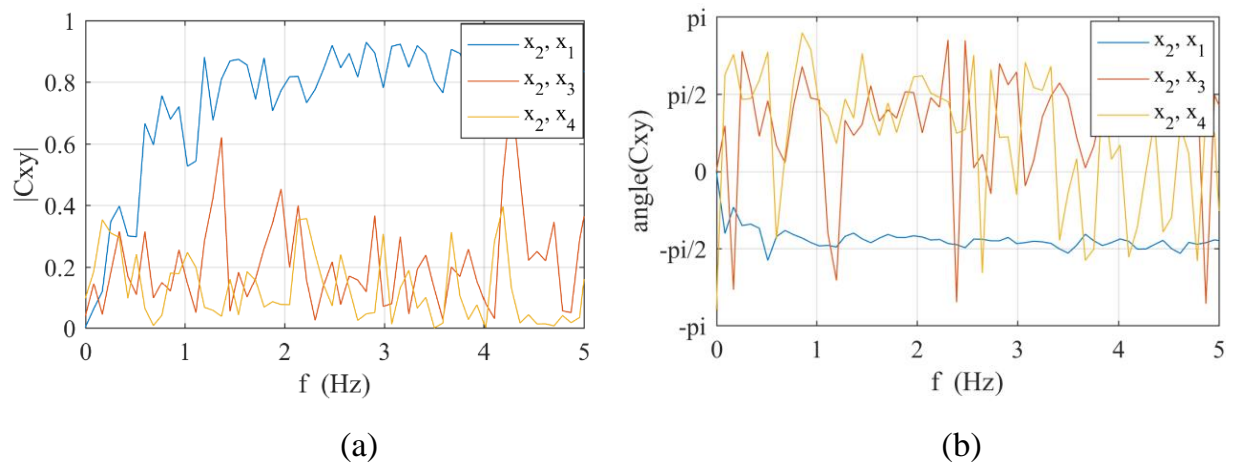


Figure 3. 15: (a) Absolute value of the coherence, and (b) phase angle of coherence of PCs for $S = 0.22$.

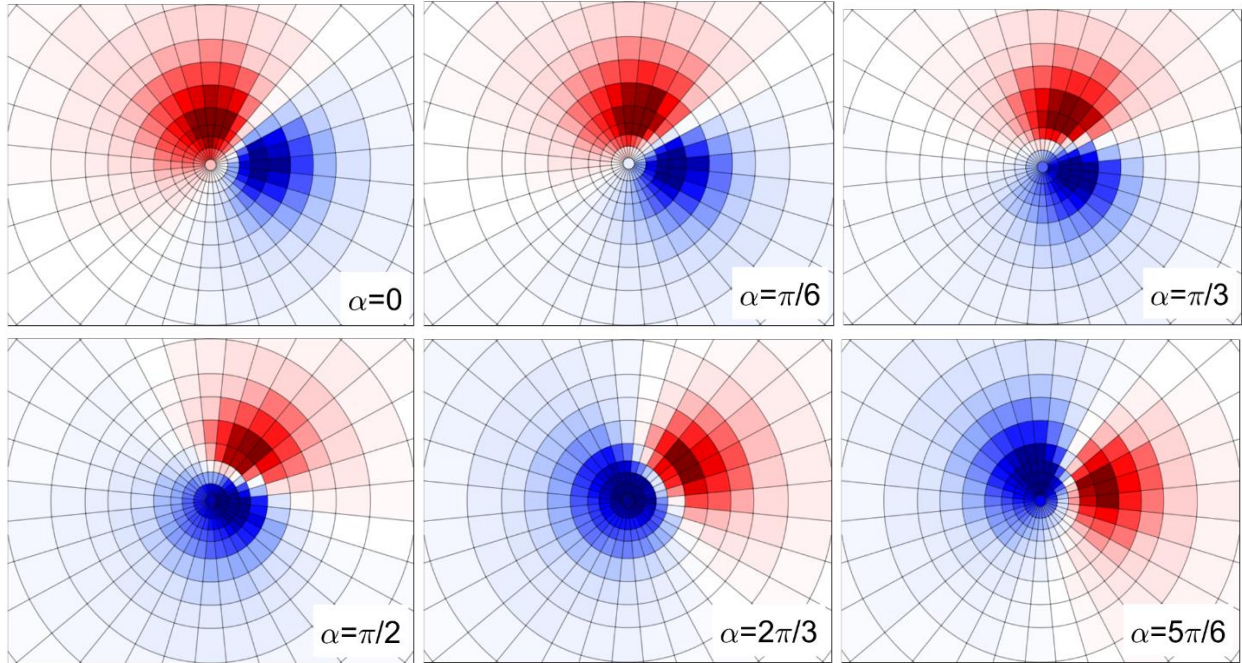


Figure 3. 16: D-ICA \bar{a}_2 for $S = 0.22$ at $f_c = 3.3 \text{ Hz}$ with $\Delta f = 2.9 \text{ Hz}$ at six different phase shifts (α). Positive (negative) values of surface pressure are shown in red (blue). The Figure scale is doubled. Wandering effects are not removed.

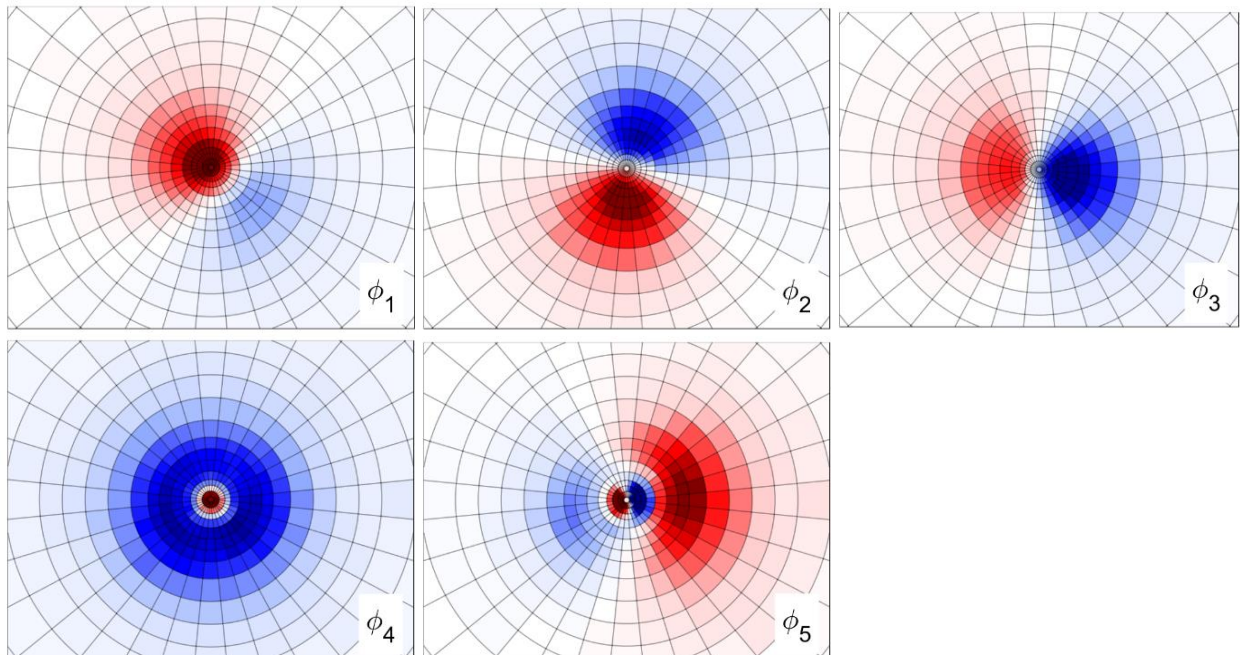


Figure 3. 17: The first five POD modes of surface pressure for $S = 0.57$. Negative (positive) values of surface pressure are shown in red (blue). Wandering effects are not removed.

3.5.2.2 Modal analysis for swirl ratio 0.57

Figure 3.17 shows the POD modes of the surface pressure for $S = 0.57$. Mode 1 corresponds to both wandering motion and size variation of the vortex; this suggestion is based on its time evolution obtained by D-ICA (see Figure 3.19-a) which is identical to the time history of the simulated vortex (see Figure 3.5). Dipole-type modes 2 and 3 represent the wandering motion. The distance between dipoles is around 6.4 cm representing the vortex core radius observed in the PIV experiment [36]. Mode 4 represents the variation in the vortex core size and associated to vortex breakdown recirculation bubble, see also Ref. [36], and mode 5 represents a single spiral.

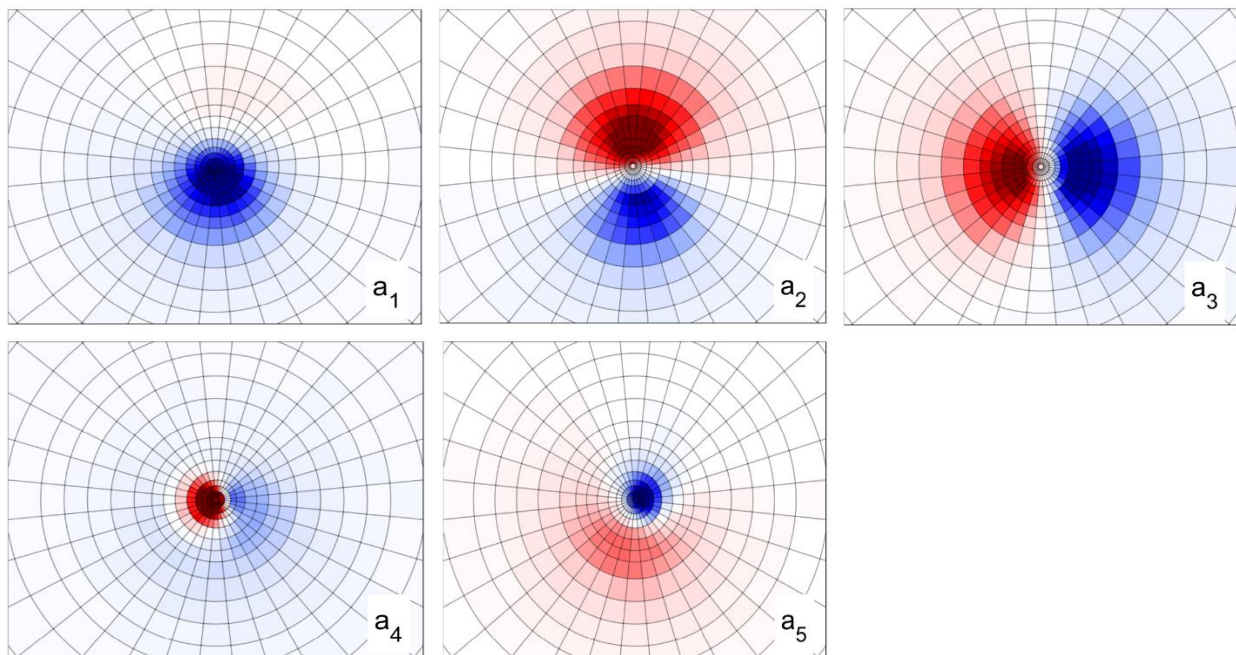
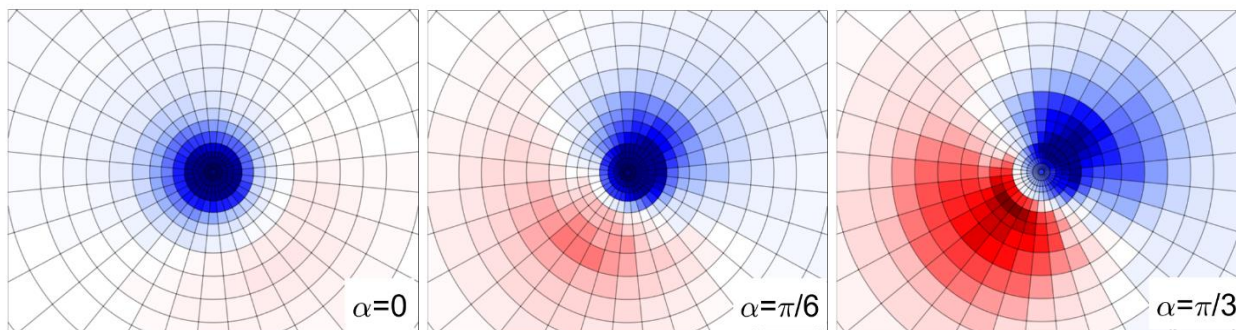
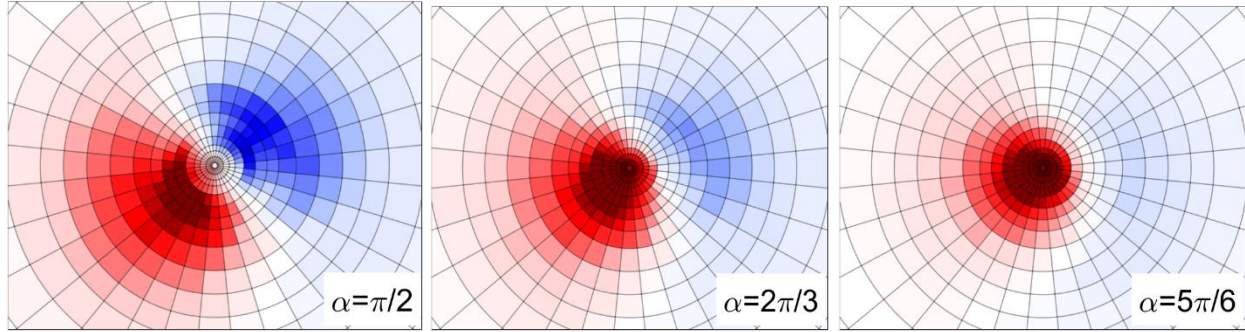
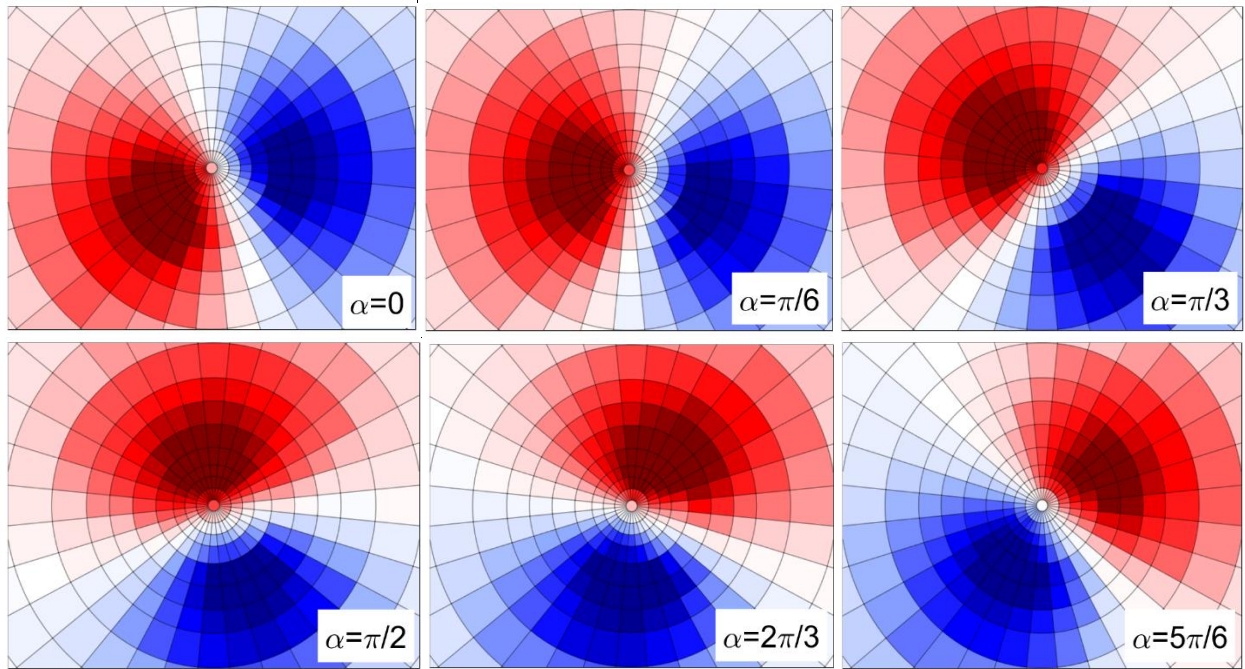


Figure 3. 18: ICA modes extracted from the data space defined from the first five POD modes for $S = 0.57$. Positive (negative) values of surface pressure are shown in red (blue). Wandering effects are not removed.





(a)



(b)

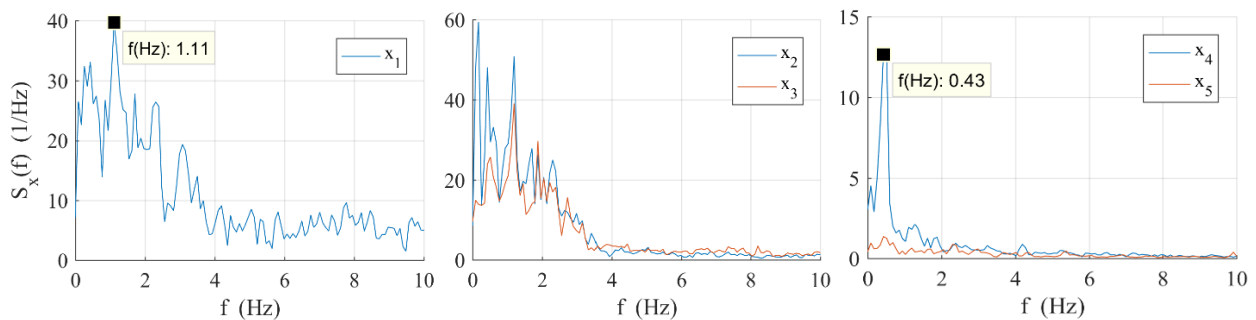
Figure 3. 19: D-ICA (a) $\bar{\mathbf{a}}_1$ and (b) $\bar{\mathbf{a}}_2$ for $S = 0.57$ at $f_c = 3.3 \text{ Hz}$ with $\Delta f = 2.9 \text{ Hz}$ at six different phase shifts (α). Positive (negative) values of surface pressure are shown in red (blue). Wandering effects are not removed.

Figure 3.18 shows the ICA modes from the data space defined from the first five POD modes. ICA mode 1 corresponds to POD mode 1 and presents the wandering motion and size variation of the vortex. ICA modes 2 and 3 correspond to POD modes 2 and 3 and show the wandering motion. ICA mode 4 corresponds to POD mode 5 and represents a single spiral. ICA mode 5 corresponds to asymmetric version of POD mode 4 and shows the size variation of the vortex.

It is interesting to note that while ICA mode 1 is very similar to ICA mode 2 (or ICA mode 3) and tend to have dipole shape, they represent distinct physical phenomena. D-ICA provides the animated movies of the ICA modes 1 and 2, shown in Figure 3.19; D-ICA mode 3 is similar to mode 2 and thus not shown here. D-ICA mode 1 shows the variation in the vortex core size (or vortex breakdown phenomenon) plus wandering motion. This suggestion is based on the time history of fluctuating pressure field of the simulated vortex (Figure 3.5) which is very similar to the D-ICA mode 1 in Figure 3.19-a. D-ICA mode 2 (Figure 3.19-b) shows that the dipoles are rotating around each other, representing wandering motion.

Figure 3.20 shows the power spectral density of the POD/ICA modes. For POD modes, or principal components in Figure 3.20-a, mode 1 has a wide band frequency between 0.25 and 3 Hz with one dominant peak at 1.11 Hz. Dipole modes 2 and 3 tend to have similar content with frequency peaks approximately limited to low range $0 < f < 2$ Hz. Mode 4 has one dominant frequency peak at 0.43 Hz, and mode 5 has noise-like distribution without a clear dominant frequency. For ICA modes, or independent components in Figure 3.20-b, mode 1 has a dominant peak around 0.51 Hz, and modes 2 and 3 tend to have similar content with frequency peaks approximately limited to low range $0 < f < 2$ Hz. Mode 4 has low-energy oscillation and mode 5 shows a dominant peak around 0.43 Hz.

Figure 3.21 shows the identity between the spectral distribution of POD modes, or principal components. The coherence function between x_2 and x_3 is very high (around 0.8), while the coherence function between other pairs are smaller. Moreover, the phase angle between x_2 and x_3 is $-\pi/2$ in almost the whole range of frequency, suggesting that modes 2 and 3 are rotating around each other. This rotation is also observable in the animated movie of D-ICA dipole mode \bar{a}_2 in Figure 3.19-b.



(a)

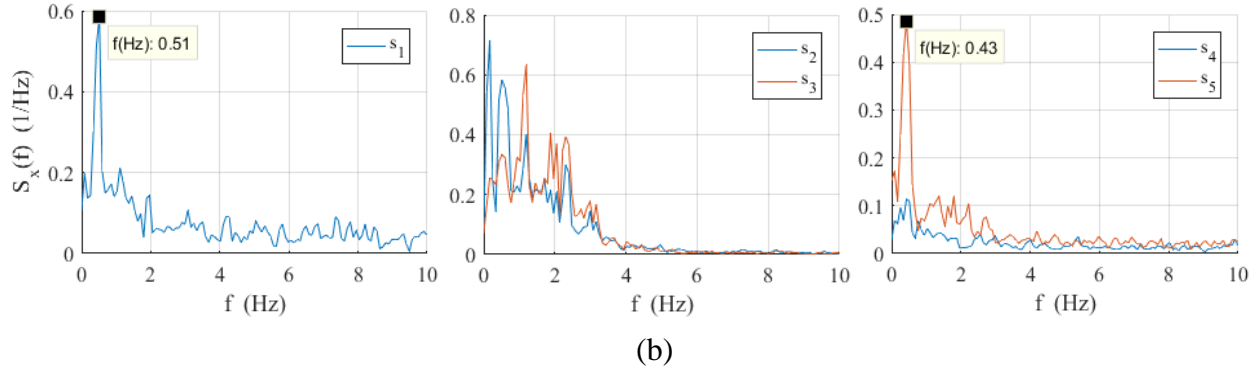


Figure 3. 20: Power spectral density of (a) PCs and (b) ICs for $S = 0.57$.

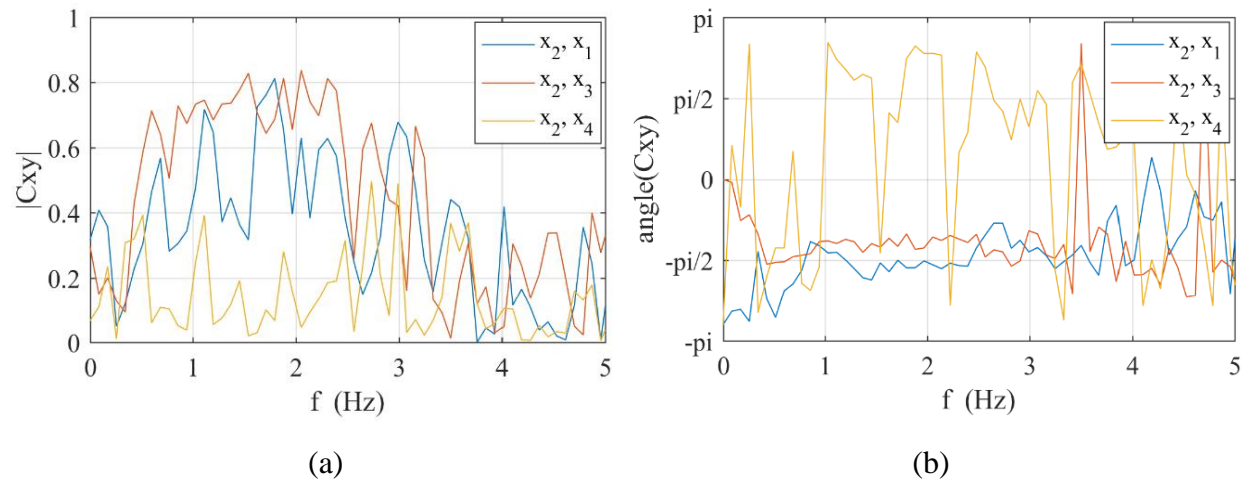


Figure 3. 21: (a) Absolute value of the coherence, and (b) phase angle of coherence of PCs for $S = 0.57$.

Briefly, for swirl ratio $S = 0.57$, the pressure field is characterized by a vortex whose size is changing periodically and is also subjected to wandering motion. It is believed that size variation of the vortex is due to the vortex breakdown phenomenon [36]. Spectral analysis shows that peak frequencies of wandering motion (or dipole modes) with a dominant frequency around 1.2 Hz get narrower, revealing the mitigation of vortex wandering phenomenon. Moreover, the size variation of the vortex has a dominant peak frequency at 0.43 Hz, and spiral vortex breakdown has noise-like spectral distribution without clear dominant peak.

3.5.2.3 Modal analysis for swirl ratio 0.96

Figure 3.22 shows the POD modes of the surface pressure. Mode 1 corresponds to both wandering motion and size variation of the vortex; this suggestion is based on the same discussion provided

for $S = 0.57$. Dipole-type modes 2 and 3 represent the wandering motion; the distance between dipoles is around 8.9 cm which is close to the vortex core radius observed in the PIV experiment [36]. Mode 4 corresponds to the size variation of the vortex which is attributed to the vortex breakdown, and mode 5 is a single spiral.

Figure 3.23 shows the ICA modes from the data space defined from the first five POD modes. ICA modes 1 and 2 correspond to POD mode 5 and show a single spiral. ICA modes 3 and 5 correspond to POD modes 2 and 3 and represent the wandering motion. ICA mode 4 corresponds to POD mode 1 and show both wandering motion and size variation of the vortex.

Figure 3.24 shows the spectral distribution of POD/ICA modes. For POD modes, or principal components in Figure 3.24-a, the single-core mode 1 has two intense components: one is restricted in the low-frequency range around 0.43 Hz and another has a wide band range concentrated around the frequency 6.5 Hz. Dipole modes 2 and 3 tend to have similar content with one dominant frequency peak around 1.03 Hz. Mode 4 has a pronounced peak around 0.43 Hz, while mode 5 has a noise-like distribution. For ICA modes, or independent components in Figure 3.24-b, ICA modes 1 and 2 have low-energy oscillation with one dominant peak frequency at 0.34 Hz. ICA Modes 3 and 5 tend to have similar harmonic content with a dominant peak frequency around 1.11 Hz. ICA mode 4 shows two frequency components around 0.43 Hz and 6.6 Hz.

Although the flow contains intermittent double-cell structure for this swirl ratio [36], POD and ICA modes have not extracted this pattern based on the surface pressure field. However, spectral analysis may give a clue to this characteristic of the vortex. Power spectral density of POD mode 1 as well as ICA mode 4 in Figure 3.24 shows appearance of a new frequency peak around 6.6 Hz which is unique for this swirl ratio $S = 0.96$ and is not observed for smaller swirl ratios ($S = 0.22$ and 0.57).

Spectral analysis shows also that the frequency peak of vortex breakdown (or size variation of the vortex) is around 0.43 Hz, and wandering motion (POD modes 2 and 3 as well as ICA modes 3 and 5) have a dominant peak frequency 1.1 Hz. The identity between POD modes 2 and 3 is also observable in the coherence function (Figure 3.25-a), which is very high (0.8) in the neighborhood of the spectral peaks. The phase angle of x_2 and x_3 is also $\pi/2$ (Figure 3.25-b), suggesting that modes 2 and 3 are rotating around each other.

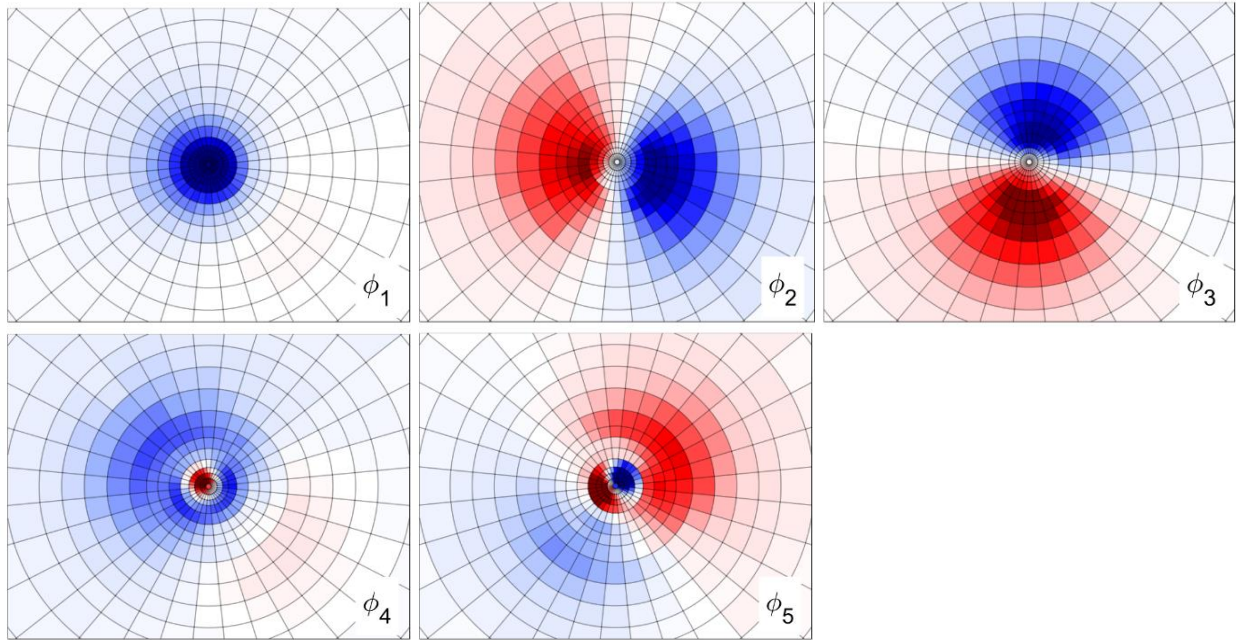


Figure 3. 22: The first five POD modes for $S = 0.96$. Positive (negative) values of surface pressure are shown in red (blue). Wandering effects are not removed.

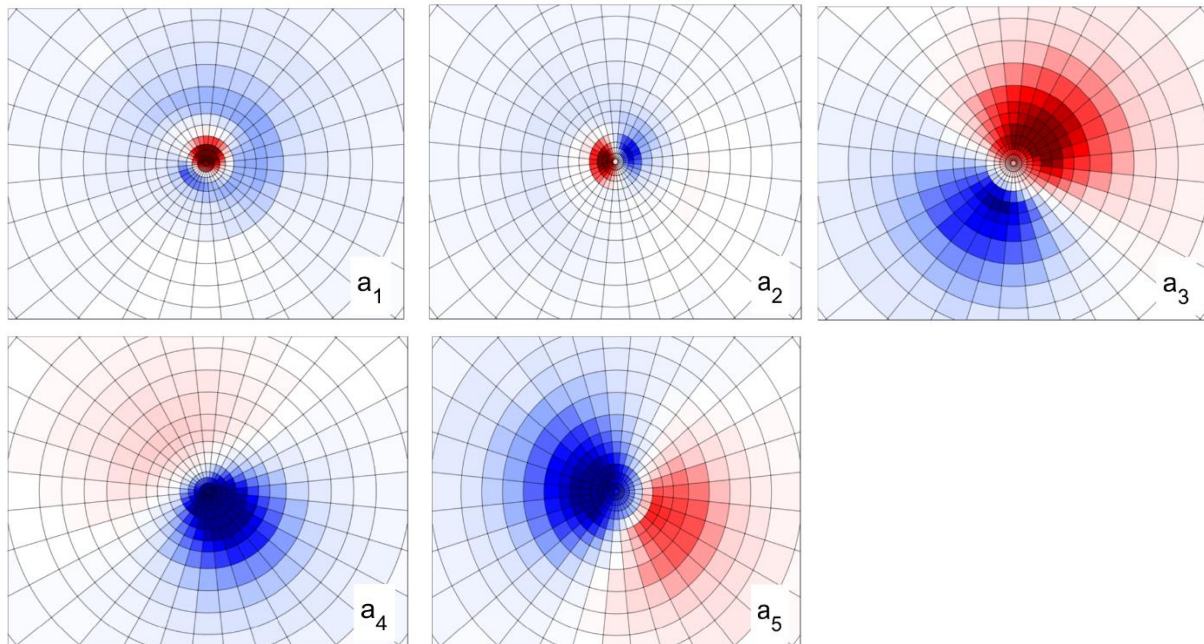


Figure 3. 23: ICA modes extracted from the data space defined from the first seven POD modes for $S = 0.96$. Positive (negative) values of surface pressure are shown in red (blue). Wandering effects are not removed.

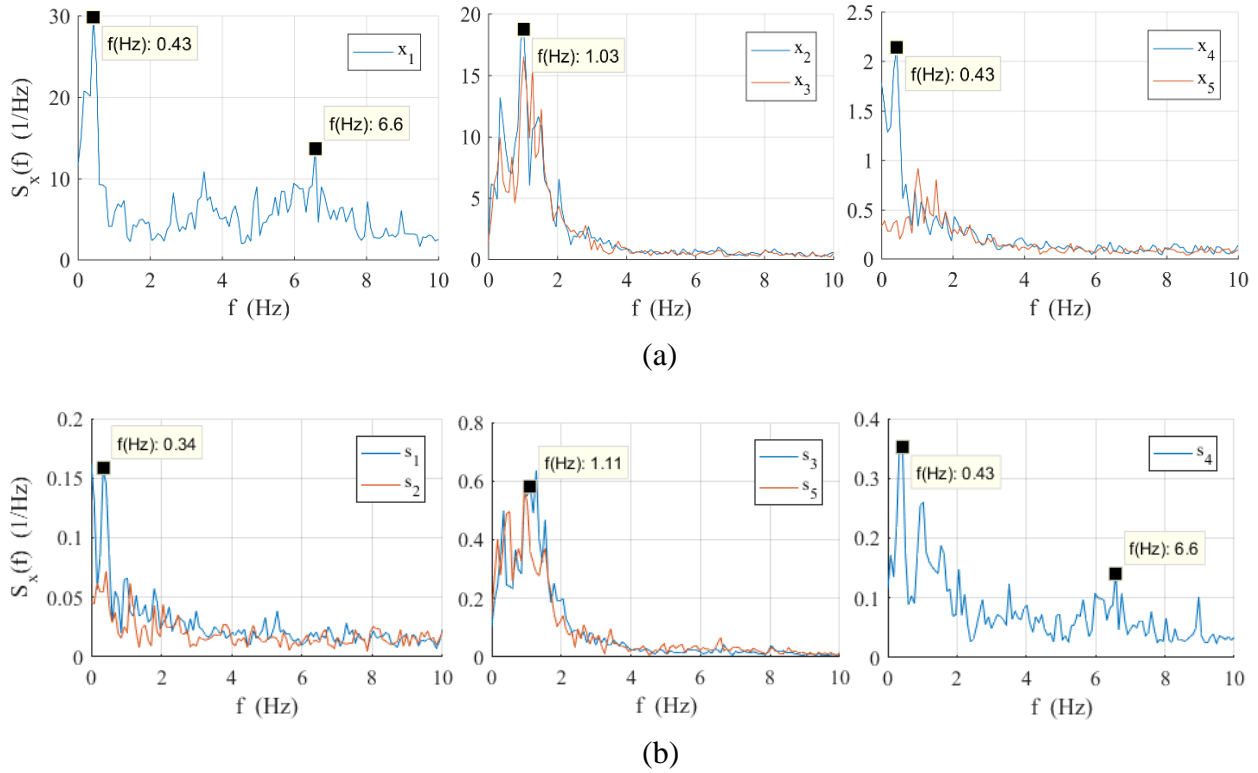


Figure 3.24: Power spectral density of (a) PCs and (b) ICs for $S = 0.96$.

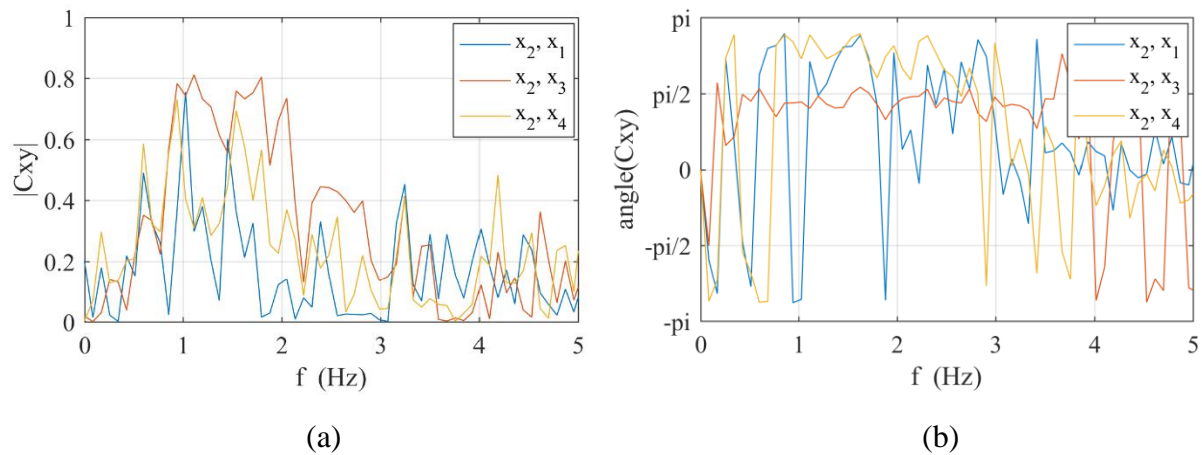


Figure 3.25: (a) Absolute value of the coherence, and (b) phase angle of coherence of PCs for $S = 0.96$.

3.6 Concluding remarks

Four decomposition methods (POD, ICA, D-POD, D-ICA) have been applied on a surface pressure fluctuation generated by tornado-like vortices. The physical interpretation of extracted

coherent structures as well as their spectral characteristics are provided. The major conclusions can be summarized as follows.

For $S = 0.22$, the vortex structure is single-cell and subjected to intensified wandering motion, which has a broad band frequency between 0.25 and 5 Hz. For $S = 0.57$, the vortex structure is single cell accompanied by vortex breakdown which leads to size variation of the vortex. Spectral analysis shows that peak frequencies of wandering motion with a dominant value around 1.2 Hz get narrower relative to what observed for $S = 0.22$, revealing the mitigation of wandering phenomenon. Moreover, vortex breakdown has dominant frequency peak at 0.43 Hz.

For $S = 0.96$, an intermittent transition between single-cell and double-cell structures occurs, based on the flow field analysis in [36]. While POD/ICA modes have not captured this pattern based on surface pressure analysis, the pressure spectral analysis show that the first POD mode (or the corresponding ICA mode) has two intense components: one is limited in the low-frequency range around 0.43 Hz and another component concentrated around 6.6 Hz. The second intense component is observed only for $S = 0.96$, suggesting the presence of double-cell structure. Moreover, peak frequencies of vortex wandering are limited to low range with a dominant frequency around 1.11 Hz, and dominant peak frequency of vortex breakdown is around 0.43 Hz.

References

- [1] A. Mariotti, G. Buresti, M.V. Salvetti, Connection between base drag, separating boundary layer characteristics and wake mean recirculation length of an axisymmetric blunt-based body, *Journal of Fluids and Structures* 55 (2015) 191-203.
- [2] A. Mariotti, G. Buresti, Experimental investigation on the influence of boundary layer thickness on the base pressure and near-wake flow features of an axisymmetric blunt-based body, *Exp Fluids* (2013) 54:1612.
- [3] J. L. Lumley, *Stochastic Tools in Turbulence*. Academic Press, New York (1970).
- [4] H. Kikuchi, Y. Tamura, H. Ueda, K. Hibi, Dynamic wind pressure acting on a tall building model - Proper orthogonal decomposition, *J. Wind Eng. Ind. Aerodyn.* 69-71 (1997) 631-646.

- [5] B. Bienkiewicz, Y. Tamura, H.J. Ham, H. Ueda, K. Hibi, Proper orthogonal decomposition and reconstruction of multi-channel roof pressure, *J. Wind Eng. Ind. Aerodyn.* 54-55 (1995) 369-381.
- [6] Y. Tamura, H. Ueda, H. Kikuchi, K. Hibi, S. Suganuma, B. Bienkiewicz, Proper orthogonal decomposition study of approach wind-building pressure correlation, *J. Wind Eng. Ind. Aerodyn.* 72 (1997) 421-432.
- [7] A. Kareem, J.E. Cermak, Pressure fluctuations on a square building model in boundary-layer flows, *J. Wind Eng. Ind. Aerodyn.* 16 (1984) 17-41.
- [8] J.D. Holmes, Analysis and synthesis of pressure fluctuations on bluff bodies using eigenvectors, *J. Wind Eng. Ind. Aerodyn.* 33 (1990) 219-230.
- [9] A. Kareem, C.M. Cheng, Pressure and force fluctuations on isolated roughened circular cylinders of finite height in boundary layer flows, *J. Fluids and Structures*, 13 (1999) 907-933.
- [10] C. J. Baker, Aspects of the use of proper orthogonal decomposition of surface pressure fields, *Wind & Struct.* 3 (2000) 97-115.
- [11] J.D. Holmes, R. Sankaran, K.C.S. Kwok, M.J. Syme, Eigenvector modes of fluctuating pressures on low-rise building models, *J. Wind Eng. Ind. Aerodyn.* 69-71 (1997) 697-707.
- [12] Y. Tamura, S. Suganuma, H. Kikuchi, K. Hibi, Proper orthogonal decomposition of random wind pressure field, *J. Fluids Struct.* 13 (1999) 1069-1095.
- [13] M. Sieber, C. O. Paschereit, K. Oberleithner, Advanced identification of coherent structures in swirl-stabilized combustors, *J. of Eng. for Gas Turbines and Power* 139 (2017) 021503-1
- [14] M. Sieber, C. O. Paschereit, K. Oberleithner, Spectral proper orthogonal decomposition, *J. Fluid Mech.* 792 (2016) 798-828.
- [15] L. Carassale, M. Brunenghi, Identification of meaningful coherent structures in the wind-induced pressure on a prismatic body, *J. Wind Eng. Ind. Aerodyn.* 104-106 (2012) 216-226.
- [16] L. Carassale, Analysis of aerodynamic pressure measurements by dynamic coherent structures, *Probabilistic Engineering Mechanics* 28 (2012) 66-74.

- [17] X. Gilliam, J. P. Dunyak, D. A. Smith, F. Wu, Using projection pursuit and proper orthogonal decomposition to identify independent flow mechanisms. *J. Wind Eng. Ind Aerodyn* 92 (2004) 53–69.
- [18] H. He, D. Ruan, K. C. Metha, X. Gilliam, F. Wu, Nonparametric independent component analysis for detecting pressure fluctuation induced by roof corner vortex. *J Wind Eng. Ind Aerodyn* 95 (2007) 429–43.
- [19] L. Carassale, M. Marre Brunenghi, Statistical analysis of wind-induced pressure fields: A methodological perspective, *J. Wind Eng. Ind. Aerodyn.* 99 (2011) 700–710.
- [20] E. T. de Grenet, F. Ricciardelli, Spectral proper transformation of wind pressure fluctuations: application to a square cylinder and a bridge deck, *J. Wind Eng. Ind. Aerodyn.* 92 (2004) 1281–1297.
- [21] T. H. Le, Y. Tamura, M. Matsumoto, Spanwise pressure coherence on prisms using wavelet transform and spectral proper orthogonal decomposition based tools, *J. Wind Eng. Ind. Aerodyn.* 99 (2011) 499–508.
- [22] P. J. Schmid, Dynamic mode decomposition of numerical and experimental data, *J. Fluid Mech.* 656 (2010) 5–28.
- [23] P. J. Schmid, Application of the dynamic mode decomposition to experimental data, *Exp. Fluids* 50 (2011) 1123–1130.
- [24] Q. Zhang, Y. Liu, S. Wang, The identification of coherent structures using proper orthogonal decomposition and dynamic mode decomposition, *Journal of Fluids and Structures* 49 (2014) 53–72.
- [25] P. J. Schmid, K. E. Meyer, O. Pust, Dynamic mode decomposition and proper orthogonal decomposition of flow in a lid-driven cylindrical cavity, 8th international symposium on PIV Melbourne, Australia, August, 2009.
- [26] S. Mariappan, A. D. Gardner, K. Richter, and M. Raffel, Analysis of dynamic stall using dynamic mode decomposition technique, *AIAA Journal* 52 (2014) 2427-2439.

- [27] T. W. Muld, G. Efraimsson, D. S. Henningson, Flow structures around a high-speed train extracted using proper orthogonal decomposition and dynamic mode decomposition, *Computers & Fluids* 57 (2012) 87–97.
- [28] K. Taira, S. L. Brunton, S. T. M. Dawson, C. W. Rowley, T. Colonius, B. J. McKeon, and O. T. Schmidt, S. Gordeyev, V. Theofilis, L. S. Ukeiley, Modal Analysis of Fluid Flows: An Overview, *AIAA Journal* 55 (2017) 4013-4041.
- [29] M. Refan, H. Hangan, Characterization of tornado-like flow fields in a new model scale wind Testing chamber, *Journal of Wind Engineering and Industrial Aerodynamic* 151 (2016)107–121.
- [30] C. R. Church, J. T. Snow, G. L. Baker, E. M. Baker, E. M. Agee, Characteristics of tornado-like vortices as a function of swirl ratio: a laboratory investigation. *J. Atmos. Sci.* 36 (1979) 1755–1766.
- [31] M. Refan, H. Hangan, Near surface experimental exploration of tornado vortices, *J. Wind Enging Industrial Aerody* 175 (2018) 120–135.
- [32] L. Carassale, G. Solari, F. Tubino, Proper Orthogonal Decomposition in Wind Engineering: Part 2: Theoretical Aspects and Some Applications, *Wind & Struct.* 10 (2007) 177-208.
- [33] P. Comon, C. Jutten (Eds.), *Handbook of blind source separation*, Academic press, Oxford, UK, 2010.
- [34] A. Hyvärinen, J. Karhunen, E. Oja, *Independent component analysis*, John Wiley and Sons, New York, 2001.
- [35] A. Gairola, G. Bitsuamlak, Numerical tornado modeling for common interpretation of experimental simulators, *J. Wind Eng. Ind. Aerodyn.* 186 (2019) 32-48.
- [36] M. Karami, H. Hangan, L. Carassale, H. Peerhossaini, Coherent structures in tornado-like vortices, *Physics of Fluids* (2019), Accepted.

Chapter 4

4 Analytical model for tornado-like vortices: mean and fluctuating flow fields

The evaluation of tornadic wind loads on structures highly depends on the accurate reconstruction of the tornado wind field. Besides, numerical and experimental simulations of tornado-like vortices, analytical modelling is attractive since it can be employed in standard codes. In this paper, the velocity field of tornado-like vortices with single-cell and double-cell structures is analytically modeled. Both the mean and fluctuating flow fields are considered. The mean flow field is modeled using a combination of Burgers-Rott model and stagnation flow. Modal analysis of experimentally generated tornado-like vortices (M. Karami et. al., 2018) has shown that the large-scale fluctuating flow field can be attributed to two phenomena: (i) random displacement of the vortex (wandering motion), and (ii) sub-vortex dynamics (coherent structures). Herein, the wandering motion of the vortex is modeled by a convolution integral approach. The sub-vortex dynamics is modeled based on the reduced vorticity field resulting from the modal analysis (Proper Orthogonal Decomposition).

4.1 Introduction

In wind engineering the analytical modeling of tornado vortices is complementary to experimental or numerical simulations and is attractive due to its simpler form and its potential implementation in risk analysis [1,2].

The most well-known analytical model is the modified Rankine vortex model which is described as follows:

$$U_{\theta} = \frac{\Gamma}{\pi} \frac{r^2}{r_c^2 + r^2} \quad (4.1)$$

where Γ is the circulation (m^2/s) considered as a constant and r_c is the core radius.

Xu and Hangan [3] presented a vortex model by combining a jet model with a modified Rankine vortex. In their approach, the jet model characterizes the radial and axial motions, and the Rankine vortex describes the tangential component. They compared the analytical model with experimental

data at only small values of Swirl ratio ($S = 0.28$). The swirl ratio is defined as the ratio of tangential to radial velocity components at the inlet, and the variation of the structure of tornado-like vortices with swirl ratio is crucial. Recently, Baker and Sterling [4] proposed a vortex model which is suitable for calculation of debris trajectories. Their tangential and axial velocity components increase with height which is not reflected by experimental data [5]. Kim and Matsui [5] provided a comprehensive review on the existing analytical models.

To the best of authors' knowledge, no analytical model has been proposed for the fluctuating flow field. Herein, we propose for the first time an analytical model which combines the mean and large-scale fluctuations of tornado-like vortices over a range of swirl ratios. Based on recently conducted modal analysis of experimental tornado-like vortices [6], it is assumed that the large fluctuating flow field is mainly attributed to two phenomena: vortex wandering motion and coherent structures (sub-vortex) dynamics. The modeled velocity fields are compared with two experimental data sets from Western WindEEE Research Institute experiments Refan and Hangan [7] and [8] and from Iowa State University experiments Zhang and Sarkar [9]. Moreover, the current model is compared with Rankine, Xu and Hangan [3], Baker and Sterling [4], Wood and White [10], and Vatisas [11] models, see the Appendix A for the analytic expression of the existing models.

4.2 Experimental setup of Mini-WindEEE Dome

The WindEEE Dome at Western university is a three-dimensional and dynamical wind testing chamber that provides a novel technique to physically simulate various types of flow fields included tornadoes and downburst [12]. A 1/11 scaled model of WindEEE Dome (MWD) was built to reproduce and verify the characteristics of WindEEE Dome. MWD uses 8 peripheral fans, except one wall that has an array of 4 rows \times 15 columns fans. MWD also uses 18 top fans, installed in an upper chamber and communicating with the main chamber through a bell-mouth. Figure 4.1 shows a schematic of MWD facility. For a more detailed description of the MWD simulator please refer to [7].

Particle Image Velocimetry (PIV) was used to measure the flow field in horizontal planes at heights of 3.5, 4.5, 7 and 8 cm above the surface. A pulsed Nd:YAG laser generator with a wavelength of 532 nm was used as a source of illumination. The laser can be run at pulse repetition

rates of up to 30 Hz with 120 mJ/pulse output energy. A CCD camera (VA-4M32, Vieworks) with a spatial resolution of 2336×1752 pixels was used to capture images. Using a calibration board, the field of view of the camera was set to 23.4 cm by 17.5 cm and pixel to meter conversion ratio was determined. The light sheet with uniform thickness of 2 mm was created using only a cylindrical lens. Since this thickness is small enough to avoid the out of plane motion errors, no spherical lens was used for these experiments. A maximum error of 7.2% was estimated for velocity measurements in horizontal planes. For more information about the experimental setup see [7].

The random motion of the vortex (wandering phenomenon) can lead to large errors in evaluating the flow field. Thus, it is necessary to remove the effects of wandering from the flow field data. Herein, we removed the wandering effects by detecting the vortex center using the method suggested by Jiang et al. [13]. Then, the vortex domain is shifted to its mean center. For more information about re-centering the vortex, see Ref. [14].

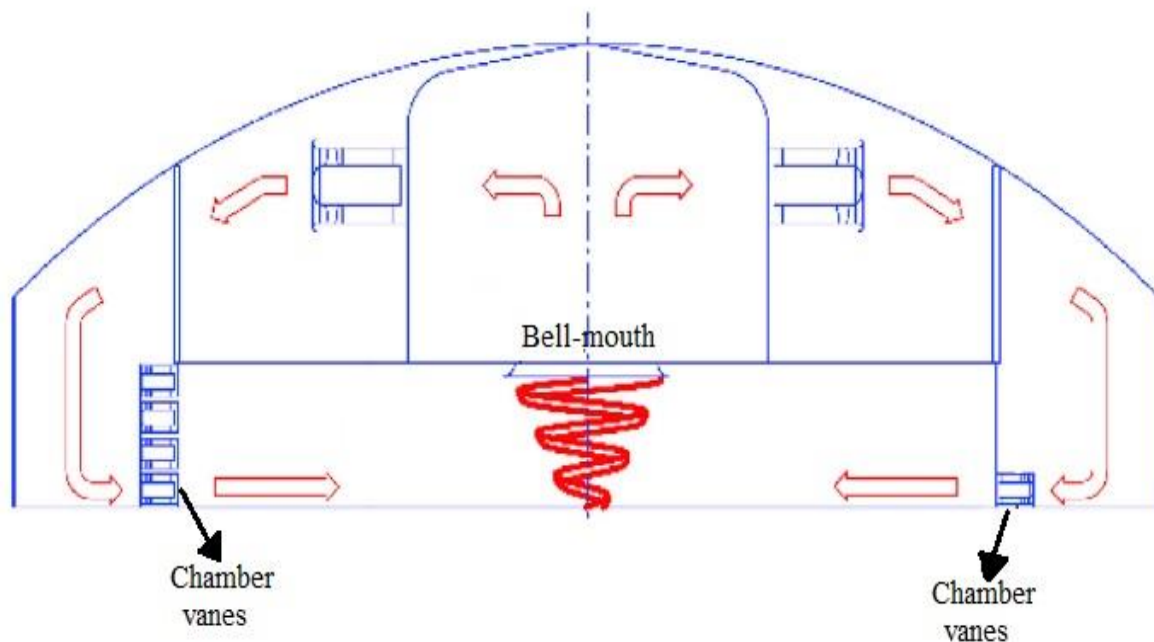


Figure 4. 1: Schematic drawing of WindEEE Dome [12].

4.3 Analytical model for the vortex flow

The current analytical model (mean and fluctuating flow fields) is proposed for a tornado-like vortex flow for three swirl ratios ($S = 0.22, 0.57$ and 0.96) as they represent distinct vortex flow structures. For $S = 0.22$, the vortex flow is characterized by single-cell structure and the flow has a laminar aspect, and at this swirl the wandering motion is high [15]. For $S = 0.57$, the flow becomes complex and a recirculation bubble vortex breakdown is formed with a single spiral rotating around the bubble [16]. For $S = 0.96$, a double spiral is formed and is rotating around the recirculation bubble leading to a vortex flow with double-cell structure [16]. For more information about the vortex dynamics of tornado-like vortices, see Ref. [6].

4.3.1 Mean flow field

The three-dimensional flow field in tornado vortices can be decomposed into a jet flow, or stagnation flow, to obtain the radial and axial velocity components and a swirl flow to obtain tangential velocity component. In addition, a boundary layer region can be considered to take into account the surface layer behaviour.

4.3.1.1 Radial and axial velocity components

According to Xu and Hangan [3], the following stream function can be used to describe a stagnation flow:

$$\Psi = W A_1 z^{B_1} \left(e^{-C_1 \left(\frac{r}{z}\right)} - 1 \right) + (1 - W) A_2 z^{B_2} \left(e^{-C_2 \left(\frac{r}{z}\right)^2} - 1 \right) \quad (4.2)$$

where W is weighted function and assumed as: $W = 1 - \exp(-0.1 r)$. $A_1, B_1, C_1, A_2, B_2, C_2$ are empirical constants. The radial and axial velocities can be obtained from the stream function as follows:

$$\frac{U_r}{U_{\theta, max}} = \frac{1}{r} \frac{d\Psi}{dz} = \frac{1}{r} \left[A_1 C_1 r W z^{B_1-2} e^{-\frac{C_1 r}{z}} + A_1 B_1 W z^{B_1-1} \left(e^{-\frac{C_1 r}{z}} - 1 \right) + 2 A_2 C_2 r^2 (1 - W) z^{B_2-3} e^{-C_2 \left(\frac{r}{z}\right)^2} + A_2 B_2 (1 - W) z^{B_2-1} \left(e^{-C_2 \left(\frac{r}{z}\right)^2} - 1 \right) \right] \quad (4.3)$$

$$\frac{U_z}{U_{\theta, max}} = -\frac{1}{r} \frac{d\Psi}{dr} = \frac{1}{r} \left[A_1 C_1 W z^{B_1-1} e^{-\frac{C_1 r}{z}} + 2 A_2 C_2 (1 - W) z^{B_2-2} r e^{-C_2 \left(\frac{r}{z}\right)^2} \right] \quad (4.4)$$

The radial and axial velocities are normalized by the maximum mean tangential velocity $U_{\theta,max}$. The radius (r) and height (z) are normalized by core radius at every height. A_1 , B_1 , C_1 , A_2 , B_2 and C_2 are empirical constants.

To consider the effect of boundary layer region near the ground, we divide z domain into two regions separated by $z_{U_r,max}$ or $z_{U_z,max}$ as a height corresponding to the maximum radial or axial velocity components. U_r and U_z within the boundary layer are defined as:

$$\frac{U_r}{U_{\theta,max}} = \left(\frac{z}{z_{U_r,max}}\right)^{\alpha_p} \quad (4.5)$$

$$\frac{U_z,max}{U_{\theta,max}} = \left(\frac{z}{z_{U_z,max}}\right)^{\alpha_p} \quad (4.6)$$

where $z_{U_r,max}$ and $z_{U_z,max}$ are respectively the height for which maximum radial and axial velocity components occur, and α_p is power-law index. Based on WindEEE Dome (WD) experiment [8], $z_{U_r,max}/r_c$ for the three swirl ratios, $S = 0.22, 0.57$ and 0.96 are respectively $0.22, 0.13$ and 0.09 . Using the WD experiment [8] α_p was also determined for the three swirl ratios based on the tangential component as being, $\alpha_p = 1/9, 1/7$ and $1/4$ for the three swirl ratios $S = 0.22, 0.57$ and 0.96 . Note that these values for α_p are assumed for the three velocity components.

Eqs. (4.3-4.4) define the velocity profiles above the surface layer, and Eqs. (4.5-4.6) define the velocity profiles within the surface layer. The empirical constants in Eqs. (4.3-4.4) were determined conducting regression analysis between the model and experimental data sets. The underlying behavior of velocity profiles in the experiments is considered to avoid overfitting in the regression analysis. For before-breakdown case ($S = 0.22$) these constants are $[A_1, B_1, C_1, A_2, B_2, C_2] = [0.14, 0.1, 1.5, 1.7, 0.75, 0.75]$. For after-breakdown case ($S = 0.57$ and 0.96), the empirical constants are $[A_2, B_2, C_2] = [1.9, 0.7, 1.6, 0.5, 0.3]$, $A_1 = 3(z_{U_r,max}/r_c)$, and $B_1 = -2A_1$.

4.3.1.2 Tangential velocity component

The swirl flow, or tangential velocity component, is originated from Burgers-Rott model [17,18]:

$$U_{\theta} = \frac{\Gamma}{2\pi r} \left[1 - \exp\left(-\frac{c r^2}{2\nu}\right) \right] \quad (4.7)$$

where ν is air kinematic viscosity, and C is empirical constant. The circulation is equal to, $\Gamma = 2\pi r_c U_{\theta,max}$ where r_c is core radius and $U_{\theta,max}$ is maximum tangential velocity at the core radius.

To implement the variations of U_{θ} with height as well as the effect of boundary layer region near the ground, we define $U_{\theta,max}$ as follows:

$$U_{\theta,max} = \begin{cases} U_{\theta,max,max} \left(\frac{z}{z_{U_{\theta,max,max}}} \right)^{\alpha_p} & (z \leq z_{U_{\theta,max,max}}) \\ D_1 U_{\theta,max,max} \exp \left(-D_2 \frac{z}{z_{U_{\theta,max,max}}} \right) & (z > z_{U_{\theta,max,max}}) \end{cases} \quad (4.8)$$

where $U_{\theta,max,max}$ is the maximum tangential velocity at $z_{U_{\theta,max,max}}$. α_p is power-law index and determined to be $\alpha_p = 1/9, 1/7$ and $1/4$ for the three swirl ratios $S = 0.22, 0.57$ and 0.96 , which are the values used for the other two velocity components. We used the function, $f(z) = D_1 U_{\theta,max,max} \exp(-D_2 z/z_{U_{\theta,max,max}})$, to satisfy the following conditions: (i) $z = z_{U_{\theta,max,max}} \rightarrow f(z) = U_{\theta,max,max}$, and (ii) $z = \infty \rightarrow f(z) = 0$. Based on WindEEE Dome (WD) experiment [8], $z_{U_{\theta,max}}/r_c$ for the three swirl ratios, $S = 0.22, 0.57$ and 0.96 are respectively $0.75, 0.47$ and 0.29 . The empirical constant for before-breakdown case ($S = 0.22$), $[D_1, D_2] = [1.03, 0.03]$, and for after-breakdown case ($S = 0.57$ and 0.96), $[D_1, D_2] = [1.11, 0.10]$.

4.3.2 Fluctuating flow field

Here, only fluctuation of tangential velocity component is considered as it is the dominant component compared to radial and vertical components. Zhang and Sarkar [9] reported that radial and vertical fluctuation vary between 8% and 23% of tangential component.

The fluctuating velocity can be decomposed into three components:

$$U_{\theta,fluc} = U_{\theta,sub-vortex} + U_{\theta,wandering} + U_{\theta,random} \quad (4.9)$$

where $U_{\theta,fluc}$ is the instantaneous fluctuating velocity and obtained by subtracting the mean tangential velocity from the instantaneous tangential velocity. $U_{\theta,sub-vortex}$ is the fluctuations attributed to coherent structures (sub-vortex dynamics), $U_{\theta,wandering}$ is the fluctuations attributed to vortex wandering motion and $U_{\theta,random}$ is the fluctuations attributed to random perturbations which is neglected here. For before-breakdown case ($S = 0.22$), only $U_{\theta,wandering}$ is significant,

and $U_{\theta,sub-vortex}$ is negligible [6]. For after-breakdown case ($S = 0.57$ and 0.96) only $U_{\theta,sub-vortex}$ is significant, and $U_{\theta,wandering}$ is negligible [6].

4.3.2.1 Fluctuations attributed to vortex wandering motions for swirl ratio $S=0.22$

In order to implement the effects of vortex wandering motions into the original Burgers-Rott model, Eq. (4.5), we used a convolution integral as follows [19]:

$$U_{\theta,corrected}(x, y) = \int_{-\infty}^{+\infty} \int_{-\infty}^{+\infty} PDF_{wandering\ motion} U_{\theta,uncorrected}(x, y) dx dy \quad (4.10)$$

Where $U_{\theta,uncorrected}(x, y)$ is the original Burgers-Rott model, Eq. (4.7), and $PDF_{wandering\ motion}$ is probability density function of the random displacement of the vortex with respect to its mean center which is assumed to be joint Gaussian distribution. Based on MWD experiment [7], for $S = 0.22$, the values of skewness and kurtosis of vortex displacement are respectively 0.39 and 3.38.

Fourier-transform technique is used here to solve the convolution integral. Thus, we take Fourier Transform of Eq. (4.10) and then transforming back to tangential velocity field. The Fourier transform of the convolution integral, Eq. (4.10), is:

$$Fourier [U_{\theta,corrected}] = Fourier [PDF_{wandering\ motion}] * Fourier [U_{\theta,uncorrected}(x, y)] \quad (4.11)$$

Before taking Fourier transform of Burgers-Rott model, Eq. (4.7), we convert it into cartesian form:

$$U_{\theta,uncorrected} = \frac{\Gamma}{2\pi(x^2 + y^2)} \left[1 - \exp\left(-\frac{c(x^2 + y^2)}{2v}\right) \right] \quad (4.12)$$

Then, we take the Fourier transform as follows (see Ref. [20] for the operation):

$$Fourier [U_{\theta,uncorrected}] = \int_{-\infty}^{+\infty} \int_{-\infty}^{+\infty} \frac{\Gamma}{2\pi(x^2 + y^2)} \left[1 - \exp\left(-\frac{c(x^2 + y^2)}{2v}\right) \right] \exp(-i(\omega_x x + \omega_y y)) dx dy \quad (4.13)$$

We can simplify the integral by introducing new variables: $y = r \sin(\theta)$, $x = r \cos(\theta)$, $\omega_y = K \sin(\alpha)$, and $\omega_x = K \cos(\alpha)$:

$$\begin{aligned} \text{Fourier}[U_{\theta, \text{uncorrected}}] &= \frac{\Gamma}{2\pi} \int_0^{+\infty} \int_0^{2\pi} \sin(\theta) \left[1 - \right. \\ &\left. \exp\left(-\frac{c r^2}{2v}\right) \right] \exp(-i k r (\cos(\alpha) \cos(\theta) + \sin(\alpha) \sin(\theta))) d\theta dr \end{aligned} \quad (4.14)$$

The term, $\cos(\alpha) \cos(\theta) + \sin(\alpha) \sin(\theta)$, can be rewritten as $\cos(\alpha - \theta)$. This leads us to introducing another variable, $\beta = \alpha - \theta$, in the integral:

$$\begin{aligned} \text{Fourier}[U_{\theta, \text{uncorrected}}] &= -\frac{\Gamma \sin(\alpha)}{2\pi} \int_0^{+\infty} \int_0^{2\pi} \cos(\beta) \left[1 - \right. \\ &\left. \exp\left(-\frac{c r^2}{2v}\right) \right] \exp(-i k r \cos(\beta)) d\beta dr \end{aligned} \quad (4.15)$$

We know that:

$$\int_0^{2\pi} \cos(\beta) \exp(-i k r \cos(\beta)) d\beta = \frac{2\pi}{i k} \frac{d}{dr} J_0(k r) \quad (4.16)$$

Where $J_0(k r)$ is first-order Bessel function. By substituting Eq. (4.16) into Eq. (4.15), we have

$$\text{Fourier}[U_{\theta, \text{uncorrected}}] = -\frac{\Gamma \sin(\alpha)}{i k} \int_0^{+\infty} \left[1 - \exp\left(-\frac{c r^2}{2v}\right) \right] \frac{d}{dr} J_0(k r) dr \quad (4.17)$$

Thus, the final solution of the Fourier transform of Burgers-Rott model, Eq. (4.13), becomes:

$$\text{Fourier}[U_{\theta, \text{uncorrected}}] = \frac{\Gamma \sin(\alpha)}{i k} \exp\left(-\frac{\nu k^2}{2c}\right) \quad (4.18)$$

For Fourier transform of the Gaussian PDF, we have:

$$\text{PDF}_{\text{wandering motion}} = \frac{1}{2\pi} \exp\left(-\frac{x^2 + y^2}{2\sigma^2}\right) \quad (4.19)$$

Using the same procedure as for $U_{\theta, \text{uncorrected}}$, we can find the Fourier transform of Eq. (4.19):

$$\text{Fourier}[\text{PDF}_{\text{wandering motion}}] = \frac{1}{2\pi} \exp\left(-\frac{\sigma^2 k^2}{2}\right) \quad (4.20)$$

After computing the Fourier transform of the Gaussian distribution and Burgers-Rott model, we can substitute Eqs. (4.18) and (4.20) into Eq. (4.11):

$$\text{Fourier} [U_{\theta,corrected}] = \frac{\Gamma \sin(\alpha)}{i k} \exp\left(-\frac{k^2(v+C\sigma^2)}{2C}\right) \quad (4.21)$$

By taking inverse Fourier transform of Eq. (4.21):

$$\text{Fourier}^{-1}[U_{\theta,corrected}] = \int_{-\infty}^{+\infty} \int_{-\infty}^{+\infty} \frac{\Gamma \sin(\alpha)}{i k} \exp\left(-\frac{k^2(v+C\sigma^2)}{2C}\right) \exp(i(\omega_x x + \omega_y y)) d\omega_x d\omega_y \quad (4.22)$$

We can solve the integral (22) using the same procedure used for the Eq. (4.13). Thus, the final solution of the Eq. (4.10) is:

$$U_{\theta,corrected} = \frac{\beta\Gamma}{2\pi r} \left[1 - \exp\left(\frac{-Cr^2}{2(v+C\sigma^2)}\right) \right] \quad (4.23)$$

where σ is standard deviation of the vortex wandering motion. β and C are empirical constants to control the shape of profile. Note that the variation of tangential velocity with height is implemented through Eq. 4.8. Based on the MWD experiment [7], for before-breakdown case ($S = 0.22$), $\beta = 1$, $C = 0.3$ and $\sigma = 0.28 r_c$. For after-breakdown case ($S = 0.57$ and 0.96), $C = 0.01/(r_c U_{\theta,max})$, β is in the range of 1 to 1.5 and the effects of wandering motion is negligible, $\sigma = 0$.

To obtain the fluctuations attributed to wandering motion, we can subtract the corrected velocity field from uncorrected velocity field as follows:

$$U_{\theta,wandering} = U_{\theta,corrected} - U_{\theta,uncorrected} \quad (4.24)$$

The effects of wandering motion on the velocity profile will be discussed in Section 3.1.

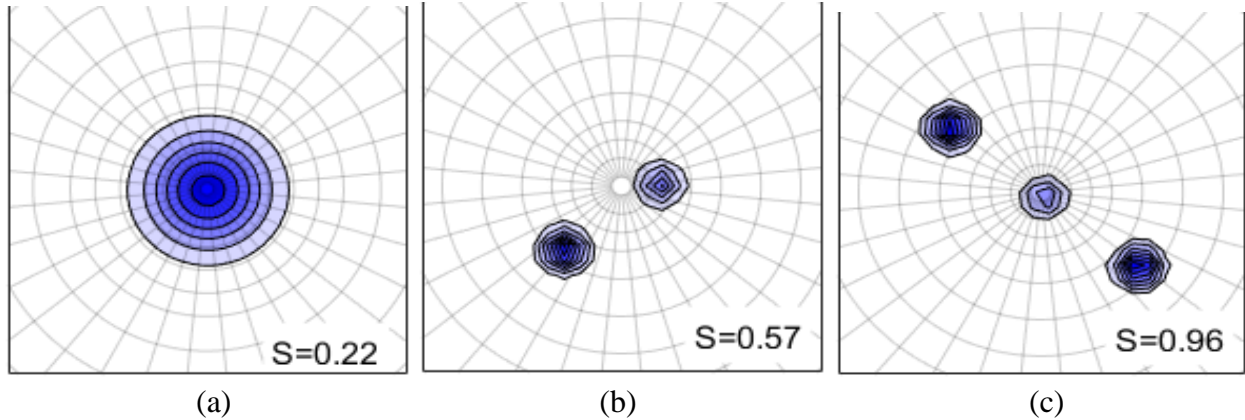


Figure 4. 2: Schematic representation of vorticity field of coherent structures. (a) $S = 0.22$, a single vortex subjected to random wandering motion. (b) $S = 0.57$, a recirculation bubble vortex at the center and a spiral vortex rotating around the bubble. (c) $S = 0.96$, a recirculation bubble vortex at the center and a double spiral vortex rotating around the bubble.

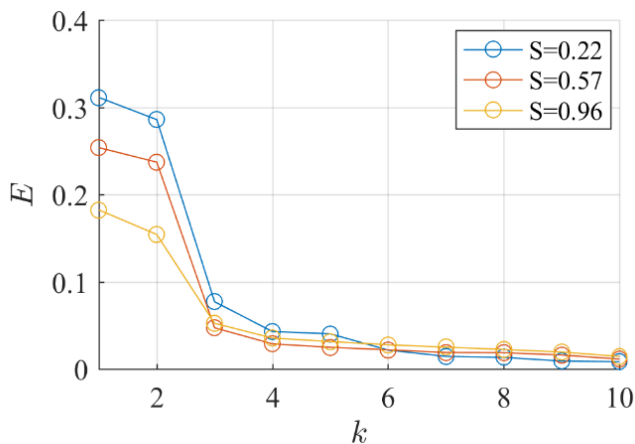


Figure 4. 3: The energy of POD modes for the three swirl ratios of MWD experiment. Wandering is included.

4.3.2.2 Fluctuations attributed to sub-vortex dynamics for swirl ratio $S=0.57$ and 0.96

Coherent structures are well-correlated regions of the fluctuating flow field that reflect the vortex dynamics and are responsible for large-scale fluctuations. The coherent structures are identified and extracted using proper orthogonal decomposition (POD) technique. POD was applied on the fluctuating flow field of MWD experiment, and based on the first two POD modes, the reduced

vorticity field, shown in Figure 4.2, was proposed [6]. For $S = 0.22$ (a), the coherent structures consist of a single vortex which is subjected to highly intensified random motion. Thus, the effect of sub-vortex dynamics is negligible. For $S = 0.57$ (b) the coherent structures are mainly representative of a recirculation bubble at the center and a spiral structure rotating around the bubble. For $S = 0.96$ (c), the coherent structures are similar to $S = 0.57$, except a double spiral was identified rotating around the recirculation bubble. A detailed description of the coherent structure identification and the associated simplified vortex field are presented in [6].

To approximate the ratio of the fluctuations from the sub-vortex dynamics to the total fluctuations ($U_{\theta,sub-vortex}/U_{\theta,fluc}$), the distribution of energy of POD modes for the three swirl ratios of MWD experiment is presented in Figure 4.3. It reveals that the energy of the first two POD modes are quite comparable and their cumulative energy falls in the range of 35% to 60% of the total fluctuating energy. Their cumulative energy is approximately 60% for $S = 0.22$, 50% for $S = 0.57$ and 33% for $S = 0.96$. The relative energy of the first two POD modes decreases with increasing swirl as at higher swirl the sub-vortex dynamics becomes more complex and at lower swirl the wandering motion is relatively more important.

Herein, we derive the fluctuating tangential velocity field from the simplified vorticity field shown in Figure 4.2. To achieve that, the following differential equation is assumed for the vorticity field [10,21]:

$$\zeta_z = \frac{dU_\theta}{dr} + \frac{U_\theta}{r} \quad (4.25)$$

where ζ_z is the vertical component of the vorticity and is assumed to be axisymmetric. For a single vortex, the vertical vorticity follows the Gaussian distribution:

$$\zeta_z/\zeta_{z,max} = \frac{(\lambda I)}{2\pi(\frac{\gamma}{r_c})^2} \exp\left(-\frac{r^2}{2(\frac{\gamma}{r_c})^2}\right) \quad (4.26)$$

where ζ_z is normalized by maximum vertical ζ component of the vorticity. I is turbulence intensity of $U_{\theta,max}$, γ is an empirical constant which controls the size of the vortex, and λ is an empirical constant to control the cumulated energy of coherent structures. By substituting Eq. (4.26) into Eq. (4.25), we can obtain the fluctuating tangential velocity for a single vortex:

$$U_{\theta,sub-vortex}/U_{\theta,max} = (\lambda I) \left[\frac{1}{r} - \frac{\exp\left(-\frac{r^2}{2\left(\frac{\gamma}{r_c}\right)^2}\right)}{r} \right] \quad (4.27)$$

where $U_{\theta,sub-vortex}$ is normalized by maximum tangential velocity.

Based on the Eq. (4.27) for a single vortex, we can assume that ζ_z follows a weighted combination of Gaussian distribution for after-breakdown cases ($S = 0.57$ and 0.96) since the flow consists of a bubble vortex at center and a spiral vortex rotating around the bubble:

$$\zeta_z/\zeta_{z,max} = (\lambda I) W \left[\frac{1}{2\pi\left(\frac{\gamma_b}{r_c}\right)^2} \exp\left(-\frac{r^2}{2\left(\frac{\gamma_b}{r_c}\right)^2}\right) \right] + (\lambda I)(1 - W) \left[\frac{r^2}{2\pi\left(\frac{\gamma_s}{r_c}\right)^2} \exp\left(-\frac{(r-(r_0/r_c))^2}{2\left(\frac{\gamma_s}{r_c}\right)^2}\right) \right] \max(\sin\omega t, 0) \quad (4.28)$$

where γ_b and γ_s are associated to the size of recirculation bubble and spiral respectively. Here, $\gamma_b/r_c = 0.13$ and $\gamma_s/\gamma_b = 0.57$. ω is the angular velocity of spiral and equals to $\omega = 2\pi St (U_{\theta,max}/r_c)$. The Strouhal number ($St = f r_c/U_{\theta,max}$) is based on the frequency of spiral(s) which was determined to be $St = 0.002$ for single spiral and $St = 0.004$ for double spiral. The frequency of spiral was obtained from the spectral analysis of surface pressure measurements in MWD experiment [7]. The constant r_0 is the distance of spiral from the center which is chosen $r_0/r_c = 0.55$, and the empirical constant $\lambda = 3.5$, based on MWD experiment. t is time variable and W is the weighted function assumed as follows:

$$W = \exp(-0.6 r) \quad (4.29)$$

By substituting Eq. (4.28) into Eq. (4.25) and solving the first order differential equation, the fluctuating tangential velocity field for after-breakdown case ($S = 0.57$ and 0.96) is:

$$\begin{aligned}
U_{\theta,sub-vortex}/U_{\theta,max} = & \lambda IW \left[\frac{1}{r} - \frac{\exp\left(-\frac{r^2}{2\left(\frac{\gamma_b}{r_c}\right)^2}\right)}{r} \right] + \lambda I(1 - W) \left[\frac{\sqrt{\frac{\pi}{2}} r_0^3 \operatorname{erf}\left(\frac{r-r_0}{\sqrt{2}\left(\frac{\gamma_s}{r_c}\right)}\right)}{\left(\frac{\gamma_s}{r_c}\right) r} - \right. \\
& \frac{r_0^2 \exp\left(-\frac{(r_0-r)^2}{2\left(\frac{\gamma_s}{r_c}\right)^2}\right)}{r} + \frac{3\sqrt{\frac{\pi}{2}} r_0 \left(\frac{\gamma_s}{r_c}\right) \operatorname{erf}\left(\frac{r-r_0}{\sqrt{2}\left(\frac{\gamma_s}{r_c}\right)}\right)}{r} - \left. \left(r + r_0 + \frac{2\left(\frac{\gamma_s}{r_c}\right)^2}{r}\right) \exp\left(-\frac{(r_0-r)^2}{2\left(\frac{\gamma_s}{r_c}\right)^2}\right) + \right. \\
& \left. \frac{1}{r} \right] \max(\sin\omega t, 0) \quad (4.30)
\end{aligned}$$

Where $\operatorname{erf}()$ is error function. Note that the fluctuating profile (Eq. 4.30) for after-breakdown case is time dependent as the spiral(s) rotate around the vortex at the center. Thus, its standard deviation profile will be used for comparison with MWD experiment.

4.4 Results and comparisons

In this section, we first look into the effects of vortex wandering on the velocity profiles for three swirl ratios. Then the current analytical model for the mean flow field is compared with two experimental data sets from Western WindEEE Research Institute experiments Refan and Hangan [7] and [8], referred to as MWD and WD, and from Iowa State University experiments Zhang and Sarkar [9], referred to as ISU. Moreover, the current model is compared with Rankine, Xu and Hangan [3], Baker and Sterling [4], Wood and White [10], and Vatistas [11] analytical models. The current analytical model for the fluctuating flow field ($U_{\theta,wandering}$ in Eq. 4.24 and $U_{\theta,sub-vortex}$ in Eq. 4.30) is compared with standard deviation profile of U_{θ} in MWD experiment.

4.4.1 Effects of vortex wandering motions

Figure 4.4 shows the effects of vortex wandering on the mean tangential velocity profile of MWD experiment for three different swirl ratios. For before-breakdown case, $S = 0.22$ (a), the effect of wandering on the velocity profile is significant. At $h = 3.5$ cm, wandering correction has resulted in an increase in maximum tangential velocity ($U_{\theta,max}$) from 9.3 (m/s) to 11.5 (m/s) as well as decrease of core radius (r_c) from 2.9 cm to 2.2 cm. Moreover, the velocity profiles remain almost

constant with increasing height when wandering effects are removed, while this is not the case for un-removed wandering cases. For after-breakdown case, $S = 0.57$ and 0.96 (b-c), the effect of wandering on the velocity profile is negligible, and the maximum tangential velocity is reduced rapidly near the ground. Note that due to the expanded core radius for $S = 0.96$, a smaller area of the flow region is captured in PIV plane.

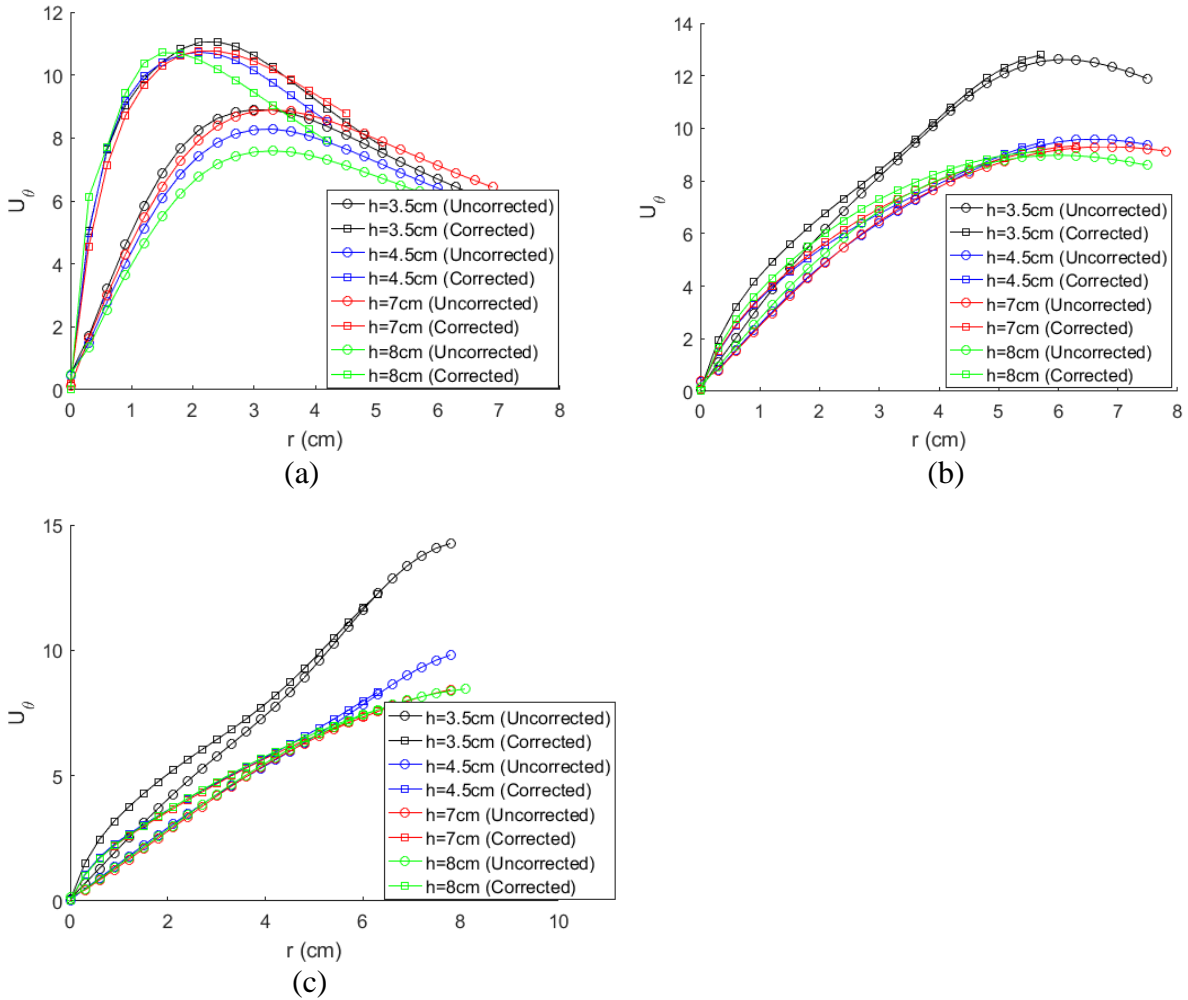


Figure 4. 4: Mean tangential velocity (m/s) profile of MWD experiment for removed (corrected) and un-removed (uncorrected) wandering effects, (a) $S = 0.22$, (b) $S = 0.57$ and (c) $S = 0.96$.

4.4.2 Comparison of mean flow field model

Figure 4.5 compares the present model for radial profile of tangential velocity (Eq. 4.23) with experimental observations and existing models. For $S = 0.22$ (a), the present model as well as

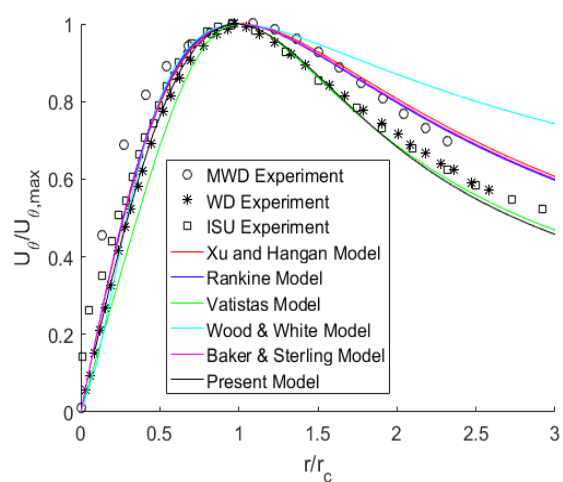
Vatistas model has a better agreement with WD and ISU experiments than the MWD experiment. Xu and Hangan model, Rankine model as well as Baker and Sterling model show similar behaviour while Wood and White model has the largest deviation from experimental observations. The same comments apply to the velocity profile for $S = 0.57$ (b). For $S = 0.96$ (c), neither model is able to capture experimental observations in the vortex core ($r \leq r_c$) since the tangential velocity is not increasing linearly with radius. At the outer core ($r > r_c$), the present model and Vatistas model has a better agreement with experimental observations. Xu and Hangan model, Rankine model as well as Baker and Sterling model show similar results while Wood and White model has the largest deviation from experimental data.

Figure 4.6 provides a comparison for the vertical profile of tangential velocity (Eqs. 4.8 and 4.23) for the three swirl ratios. The present model and Xu and Hangan model capture the boundary layer effects, while Baker and Sterling model U_θ linearly increases with height which is not realistic. For $S = 0.22$ (a), the variation of U_θ with height above the boundary layer is smooth. However, for $S = 0.57$ and 0.96 (b-c), a sharp variation of U_θ with height can be observed.

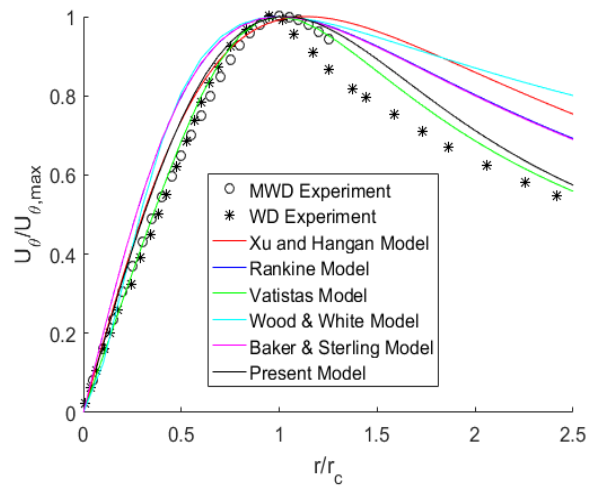
Figure 4.7 compares the radial and vertical profiles of U_r and U_z for $S = 0.22$ and its comparison with existing models and experimental observations. The radial profiles are plotted for $z = 0.4 r_c$ and the axial profile is plotted for $r = r_c$. Due to the lack of experimental data, the vertical profile of U_z is not shown. The radial profile of U_r (Figure 4.7-a) shows that the radial flow is convergent toward the center with minimum value at the center ($r = 0$). The present model and Baker and Sterling model provide a better agreement than Vatistas model as well as Xu and Hangan model.

The radial profile of U_z (Figure 4.7-b) shows that axial velocity varies between 10% to 25% of $U_{\theta,max}$ and its maximum value occurs at the core radius. Vatistas model is the only model which predicts maximum value of U_z at $r = r_c$ while the other models predict the maximum value of U_z at the center $r = 0$. Moreover, all the models, except Vatistas model, suggest that the maximum value of U_z is more than 50% of $U_{\theta,max}$ which is not consistent with experimental observations.

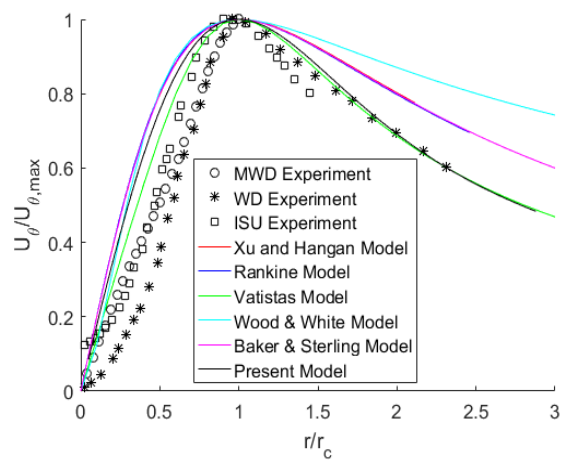
The vertical profile of U_r (Figure 4.7-c) shows that the current model and Baker and Sterling model have a better agreement than the Xu and Hangan model. Moreover, Xu and Hangan model misses the no-slip boundary condition on the wall ($z = 0$).



(a)



(b)



(c)

Figure 4. 5: The radial profile of normalized tangential velocity and its comparison with existing models for (a) $S = 0.22$ at $z = r_c$, (b) $S = 0.57$ at $z = 0.6 r_c$, and (c) $S = 0.96$ at $z = 0.4 r_c$.

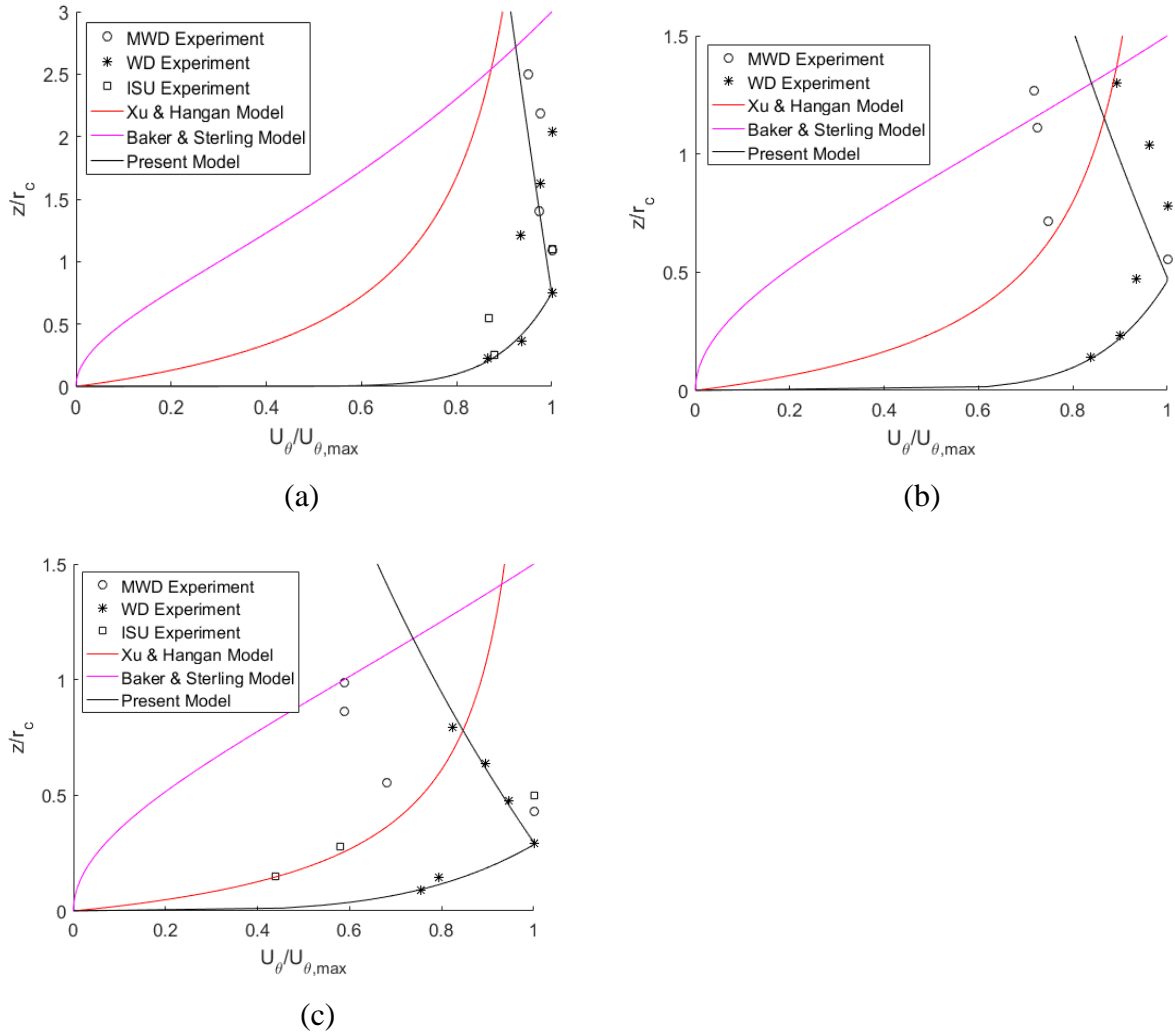
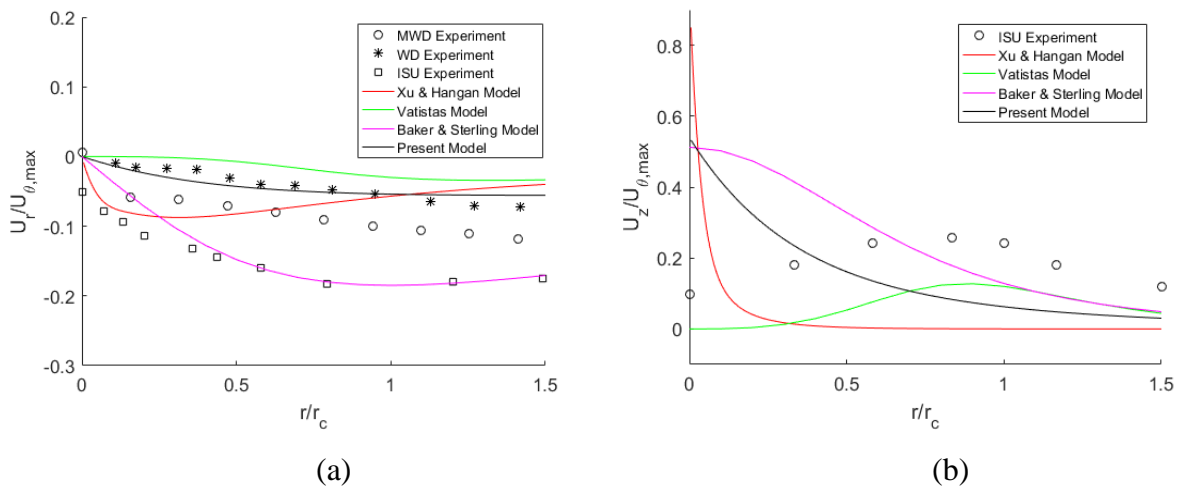


Figure 4. 6: The vertical profile of normalized tangential velocity and its comparison with existing models at $r = r_c$ for (a) $S = 0.22$, (b) $S = 0.57$, and (c) $S = 0.96$.



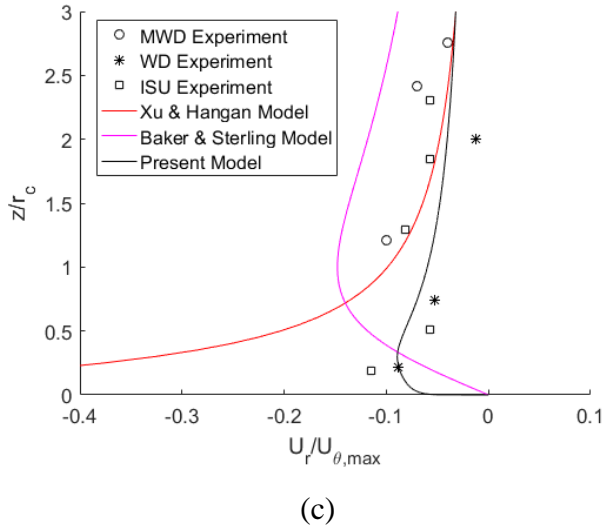
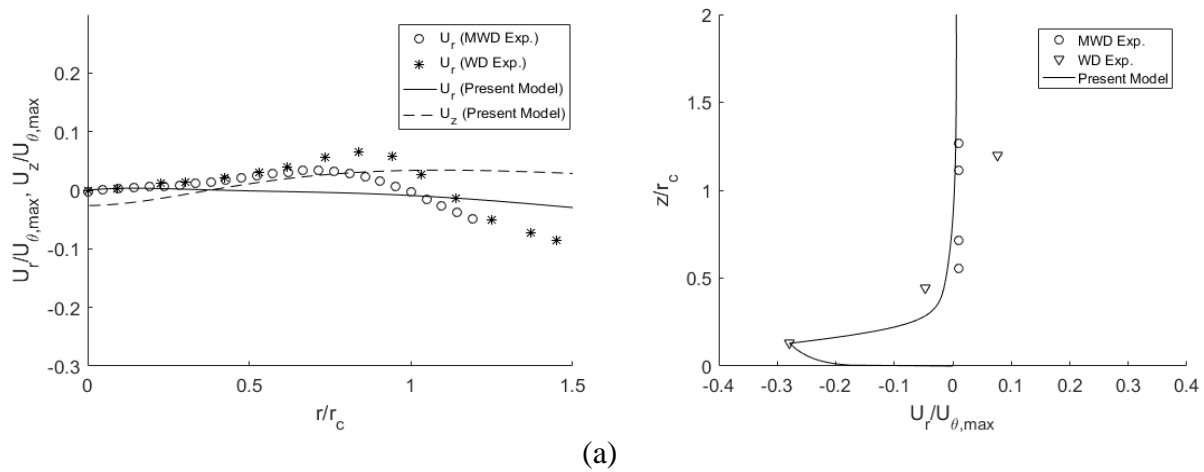


Figure 4. 7: The radial (a-b) and vertical (c-d) profiles of normalized radial and axial velocity components and their comparison with existing models for $S = 0.22$ ($z = r_c$ and $r = r_c$).

Figure 4.8 shows the radial and vertical profiles of U_r and U_z for after-breakdown case ($S = 0.57$ and 0.96). The radial profiles are plotted for $z = 0.4 r_c$ and the axial profile is plotted for $r = r_c$. It shows that vortex is leading to a downdraft vertical or divergent radial flow, and U_r is almost negligible compared to $U_{\theta,max}$. Moreover, maximum values of U_r and U_z occur at the core radius, $r = r_c$.



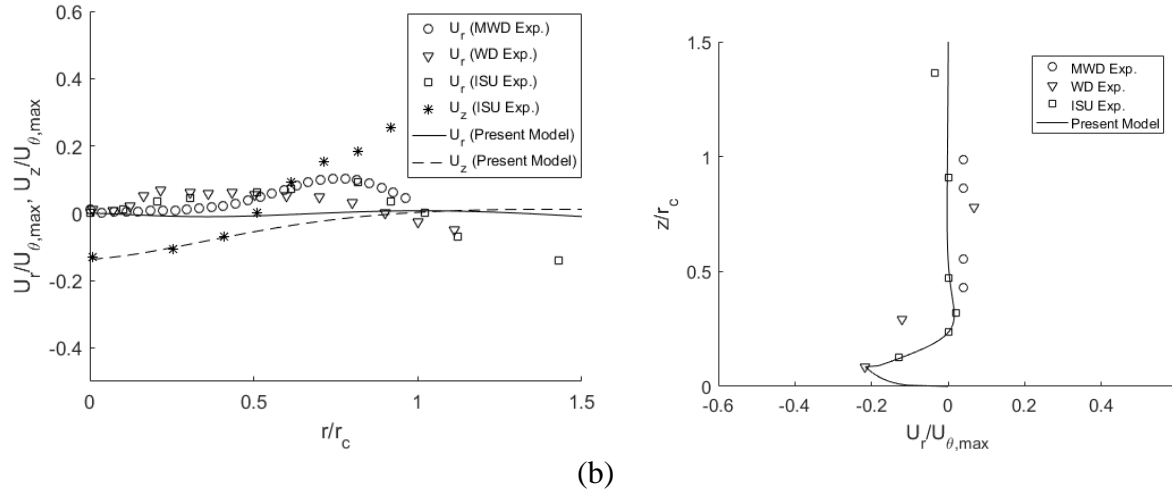


Figure 4. 8: The radial and vertical profiles of mean radial and axial velocity components (Eqs. 4.3 and 4.4) at $r = r_c$ for (a) $S = 0.57$ at $z = 0.6 r_c$, and (b) $S = 0.96$ at $z = 0.4 r_c$.

4.4.3 Comparison of fluctuating flow field model

Based on recently conducted modal analysis of experimental tornado-like vortices [6], it is assumed that fluctuations from wandering motion ($U_{\theta,wandering}$) is significant for before-breakdown case, $S = 0.22$, leading to negligible effects of fluctuations from sub-vortex dynamics ($U_{\theta,sub-vortex}$). However, for after-breakdown case, $S = 0.57$ and 0.96 , it is reverse; $U_{\theta,sub-vortex}$ is significant, and $U_{\theta,wandering}$ is negligible.

Figure 4.9 compares the analytical model of $U_{\theta,wandering}$ (Eq. 4.24) with the standard deviation profile of U_{θ} in MWD experiment for the before-breakdown case ($S = 0.22$). A similar trend is observed between model and experimental results but MWD experiment shows that fluctuation is maximum at $r = 0.3 r_c$ and the analytical model suggests this value at $r = 0.6 r_c$.

Figure 4.10 compares the standard deviation of the model of $U_{\theta,sub-vortex}$ (Eq. 4.30) with that of MWD experiment for after-breakdown cases ($S = 0.57$ and 0.96). It shows that the fluctuation is increased by swirl ratio and its maximum value occurs at $r = 0.7 r_c$. Reasonable similar trends are present in the model and the experimental data. Note that the analytical model has extremum point around $r = 0.55 r_c$, and thus the model is not shown around this point.

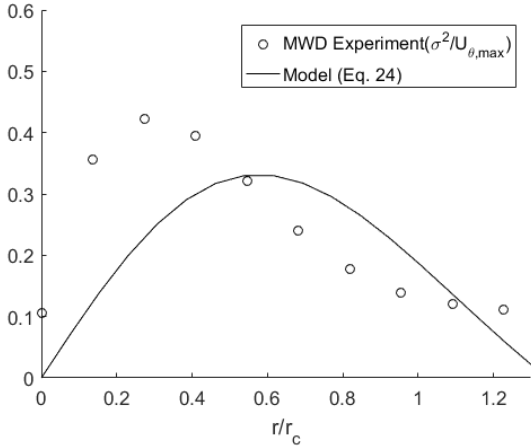


Figure 4. 9: Radial profile of the fluctuating tangential velocity based on wandering motion and its comparison with MWD experiment at $z = r_c$ for $S = 0.22$.

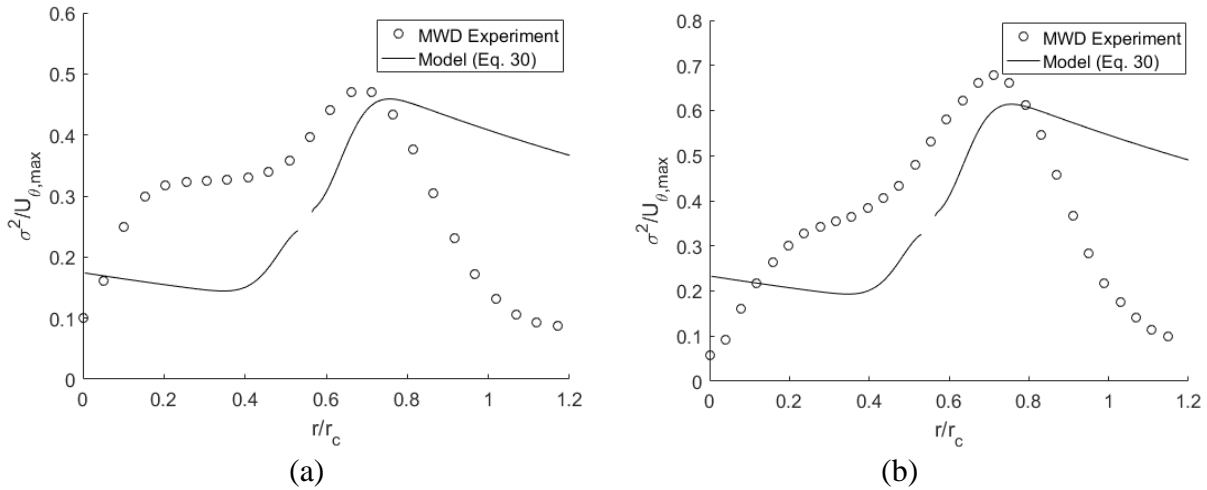


Figure 4. 10: Radial profile of the fluctuating tangential velocity based on sub-vortex dynamics and its comparison with MWD experiment for (a) $S = 0.57$ at $z = 0.6 r_c$ and (b) $S = 0.96$ at $z = 0.4 r_c$.

4.5 Concluding remarks

An analytical model is proposed for tornado-like vortex flows with both single-cell and double-cell structures for a large range of swirl ratios ($0.22 \leq S \leq 0.96$). The model addresses for the first time both the mean and the fluctuating flow fields. The mean flow field is modeled using a

combination of Burgers-Rott model, stagnation flow and boundary layer flow. The fluctuating flow field is simplified to the large fluctuations attributed to vortex wandering and sub-vortex dynamics. The model shows satisfactory agreement with experimental results obtained from two separate experimental facilities. The present model is a step forward in analytically describing the complex tornado-like vortex fields with application in wind engineering and risk analysis.

References

- [1] L. A. Twisdale, Tornado Missile Simulation and Design Methodology, EPRI NP-2005, Electric Power Research Institute, Palo Alto, Calif., Aug., 1981.
- [2] L. A. Twisdale, W. L. Dunn, Probabilistic analysis of tornado wind risks, *Journal of Structural Engineering*, 109 (1983) 468-488.
- [3] Z. Xu and H. Hangan, An Inviscid Solution for Modeling of Tornado-Like Vortices. *Journal of Applied Mechanics* 76 (2009) 03011-5.
- [4] C. J. Baker and M Sterling, Modelling wind fields and debris flight in tornadoes, *Journal of Wind Engineering and Industrial Aerodynamics* 168 (2017) 312-321.
- [5] Y. C. Kim, M. Mastsui, Analytical and empirical models of tornado vortices: A comparative study, *Journal of Wind Engineering & Industrial Aerodynamics* 171 (2017) 230–247.
- [6] M. Karami, L. Carassale, M. Refan, H. Hangan, Coherent structures of tornadolike vortices. In: 5th Joint US-European Fluids Engineering Division Summer Meeting, FEDSM 2018, Montreal, Canada.
- [7] M. Refan, H. Hangan, Characterization of tornado-like flow fields in a new model scale wind testing chamber, *Journal of Wind Engineering and Industrial Aerodynamics* 151 (2016) 107-121.
- [8] M. Refan, H. Hangan, Near surface experimental exploration of tornado vortices, *Journal of Wind Engineering & Industrial Aerodynamics* 175 (2018) 120–135.
- [9] W. Zhang, P. P. Sarkar, Near-ground tornado-like vortex structure resolved by particle image velocimetry (PIV), *Exp Fluids* (2012) 52:479–493.
- [10] V. T. Wood, L. W. White, A new parametric model of vortex tangential-wind profiles: development, testing and verification. *J. Atmos. Sci.* 68 (2011) 990–1006.

- [11] G. H. Vatistas, V. Kozel, W. C. Mih, A simpler model for concentrated vortices. *Exp. Fluid* 11 (1991) 73–76.
- [12] H. Hangan, M. Refan, C. Jubayer, D. Romanic, D. Parvu, J. Lotufo, A. Costache, Novel techniques in Wind Engineering, *Journal of Wind Engineering & Industrial Aerodynamics* 171 (2017) 12-33.
- [13] M. Jiang, R. Machiraju, D. Thompson, 2002. In: Ebert, D., Brunet, P., Navazo, I. (Eds.), *A Novel Approach to Vortex Core Region Detection*. The Eurographics Association, pp. 217–225.
- [14] A. L. Heyes, R. F. Jones, D. A. R. Smith, Wandering of wing-tip vortices. In *International Symposia on Applications of Laser Techniques to Fluid Mechanics*, Lisbon, Portugal, (2004) 1–20.
- [15] R. Ashton, M. Refan, G. V. Iungo, H. Hangan, Wandering corrections from PIV measurements of tornado-like vortices, *J. Wind Enging Industrial Aerody.* 189 (2019) 163-172.
- [16] C. R. Church, J. T. Snow, G. L. Baker, E. M. Baker, E. M. Agee, Characteristics of tornado-like vortices as a function of swirl ratio: a laboratory investigation. *J. Atmos. Sci.* 36 (1979) 1755–1766.
- [17] J. M. Burgers, A mathematical model illustrating the theory of turbulence, *Adv. Appl. Mech.* 1 (1948) 171–199.
- [18] N. Rott, On the viscous core of a line vortex. *Math. Phys.* 9 (1958), 543–553.
- [19] W. Devenport, M. Rife, S. Liapis, G. Follin, The structure and development of a wing-tip vortex. *Journal of Fluid Mechanics*, 312 (1996) 67-106.
- [20] J. Monaghan, J. Humber, Vortex particle methods for periodic channel flow, *J. Comput. Phys.* 107 (1993) 152-159.
- [21] C. N. Sun, E. G. Burdette, R. O. Barnett, Theoretical tornado vertex model for nuclear plant design. *Nucl. Eng. Des.* 44 (1977) 407–411.

Chapter 5

5 Conclusions and recommendations

The scope of the present research is three-folded. First, the three-dimensional structure of tornado-like vortices is re-constructed by extracting coherent structures out of the fluctuating velocity field using proper orthogonal decomposition (POD) technique as well as dynamic POD to provide the temporal evolutions of these coherent structures. The relationship between POD modes and physical mechanisms in tornado-like vortices is interpreted synthetic vortex simulations for various Swirl ratios. Second, statistical analysis of surface pressure fluctuations is also analysed by means of several modal decompositions such as POD, dynamic POD, Independent Component Analysis (ICA), dynamic ICA as well as spectral analysis of the extracted coherent structures. Third and finally, an analytical model is defined for both the mean and, for the first time, for the fluctuating flow field of tornado-like vortices with both single-cell and double-cell structures. The mean flow field is modeled using a combination of Burgers-Rott model and stagnation flow. The fluctuating field is modeled by solving the first order partial differential equation of the fluctuating velocity derived from the vorticity field of experimentally resolved coherent structures. Concluding remarks as well as recommendations for future work are provided at the end of this chapter.

5.1 Summary

Chapter 2 of this thesis is dedicated to the investigation of the dynamics of tornado-like vortices through a set of novel physical experiments and modal analyses for a wide range of swirl ratios ($0.22 \leq S \leq 0.96$). Various physical phenomena such as wandering, vortex breakdown or transition from one-cell to two-cell structures are observed. To investigate the coherent structure of the tornado vortices, two different decomposition methods are applied: (i) proper orthogonal decomposition (POD), also referred to as principle component analysis (PCA) and (ii) a novel dynamic proper orthogonal decomposition (D-POD) to provide time evolutions of the POD modes [1, 2]. To foster the physical interpretation of these POD modes, modal decomposition of a simulated synthetic vortex is also provided. The outcome of this Chapter 2 is the clear definition

of the sub-vortex dynamics (coherent structures) for each vortex regime from single cell before vortex break-down to vortex break down and the formation of double cells.

The following chapter, Chapter 3, presents statistical analysis of surface pressure fluctuations in tornado-like vortices. To overcome POD orthogonality constraint [3-5], an advanced method independent component analysis (ICA) is applied [6-8]. Furthermore, these two methods are generalized in the frequency domain, called dynamic POD and dynamic ICA, to provide the temporal evolutions of coherent structures over the spatial domain [2]. A comparison between modal decomposition techniques and some common statistical techniques is also provided. The outcome of this Chapter 3 is the first modal characterization of the surface pressure field in tornado-like vortices which provides the modal analysis frame for further interpreting bluff body aerodynamics in tornado vortices. Regardless of the reference to tornado-like vortices, the discussion of the present chapter can be helpful in the physical interpretation of swirling flows in general.

In the last paper, Chapter 4, the velocity field of tornado-like vortices with single-cell and double-cell structures is analytically modeled. Both the mean and fluctuating flow fields are considered. The mean flow field is modeled using a combination of Burgers-Rott model and stagnation flow. Modal analysis of experimental observations has shown that the large-scale fluctuating flow field can be attributed to two phenomena: (i) random displacement of the vortex (wandering motion), and (ii) sub-vortex dynamics (coherent structures) which are well-correlated regions in the fluctuating flow field. The wandering motion of the vortex is modeled by a convolution integral approach. The sub-vortex dynamics is modeled by solving the first order partial differential equation of the fluctuating velocity derived from the vorticity field of experimentally resolved coherent structures.

5.2 Conclusions

Based on the overall findings of this thesis, the following major conclusions are stated below. Major findings from velocity field analysis in Chapter 2 are:

- For $S = 0.22$, the mean flow field shows a single vortex with convergent radial flow towards center. However, a divergent radial flow appears in the horizontal PIV planes at lower

heights due to the vortex tilting. The modal analysis, or coherent structures extracted by POD, shows a single vortex subjected to wandering motion. Streamlines in a snapshot of the horizontal PIV plane also reveals a single vortex. Due to the absence of vortex breakdown at this swirl ratio, the coherent structures are quite persistent along the height and the flow looks laminar. The resulting schematics of the mean flow field and the vortex dynamics for this swirl ratio are also suggested.

- For $S = 0.57$, the mean flow field shows a recirculation bubble vortex breakdown accompanied with a divergent radial flow at the vortex center. The POD analysis shows a recirculation bubble with a single spiral rotating around it. Moreover, the coherent structures gradually disappear along the vortex height because of the presence of vortex breakdown. At this swirl ratio, a transition from single spiral to double spiral (or transition from one-cell to two-cell), resembling two intertwined sub-vortices, occurs, but it is very weak in terms of occurrences. Streamlines in a snapshot of the horizontal PIV plane revealing a double spiral pattern confirmed that the number of snapshots showing double spiral is 9 out of 2018 snapshots, and the ensemble average distance between the two sub-vortices is 2.7 cm. The resulting schematics of the mean flow field and the vortex dynamics for this swirl ratio are also suggested.
- For $S = 0.96$, the mean flow field shows that the recirculation bubble is expanded into an annular form with a stagnant area (zero-value velocity) inside the core region. The modal analysis, or coherent structures extracted by POD, shows a recirculation bubble with a double spiral rotating around it. This structure refers also to two-cell structure. Rapid destruction of coherent structure along the vortex height can be observed because of the high turbulence in the flow. Streamlines in a snapshot of the horizontal PIV plane for revealing double spiral pattern confirmed that double spiral occurs more often compared to the $S = 0.57$ case.

Major findings from surface pressure analysis in Chapter 3 are:

- For $S = 0.22$, the pressure field is characterized by a vortex which is subjected to Gaussian random wandering, and spectral analysis shows that wandering motion has a broad band frequency.

- For $S = 0.57$, the pressure field is characterized by a vortex whose size is changing periodically and is also subjected to wandering motion. It is believed that size variation of the vortex is due to the vortex breakdown phenomenon. Spectral analysis shows that peak frequencies of wandering motion become narrower compared to *the* $S = 0.22$ case and the wandering is weaker. Moreover, a dominant frequency is identified for the size variation of the vortex.
- For $S = 0.96$, while the flow field (Chapter 3) contains intermittent double-cell structure, both POD and ICA modes have not extracted this pattern. However, spectral analysis may give a clue to this characteristic of the vortex. It shows that both POD and ICA modes have two intense frequency components which is a unique characteristic for this swirl ratio $S = 0.96$ and is not observed for smaller swirl ratios ($S = 0.22$ and 0.57).
- Spectral analysis shows that modes having the same circumferential shape tend to have similar spectral distribution. This identity, for instance, between dipole POD modes was observable. The coherence function between those modes is very high, while the coherence function between other pairs are smaller. Moreover, the phase angle between them is almost $-\pi/2$, suggesting that those modes are rotating around each other. This rotation is also observable in the animated movie of D-ICA of dipole modes.

Major findings from analytical modeling in Chapter 4 are:

- The mean radial and the mean vertical velocity components can be described by impinging jet flow. The mean tangential velocity component can be obtained based on a Burgers-Rott model.
- The nature of turbulence characteristics is modeled for the first time. Based on the results of modal analysis from Chapter 2, it was assumed that large scale fluctuating flow field can be attributed to two phenomena: (i) random displacement of the vortex (wandering motion), and (ii) sub-vortex dynamics (coherent structures).
- The wandering motion of the vortex is modeled by a convolution integral approach. The sub-vortex dynamics is modeled by solving the first order partial differential equation of the fluctuating velocity derived from the vorticity field of experimentally resolved coherent structures.

5.3 Recommendation and future work

Despite the past and current progress on the topics related to this thesis, there are still areas for further development and improvement on the current body of knowledge. In this regard, the following recommendations for future work are suggested:

- The underlying mechanism of wandering motion in tornado-like vortices is not discussed yet, and it's not clear if the main source of wandering is attributed to simulators boundary conditions or they relate to vortex instability [9].
- Identification of coherent structures out of full-scale data is of most interest. Comparing coherent structures from full-scale data with laboratory observations might help us to achieve a new fluctuating flow field similarity for tornado vortices.
- Here, the analytical model has been defined for the case of stationary tornado vortices. It is of interest to investigate the effects of translation and roughness on the coherent structures and the modelling of tornado-like vortices.
- To capture a large field of view, PIV has been done with low sampling frequency which prevented us to measure the flow in longitudinal plane. PIV with high sampling frequency using high speed camera and laser in vertical plane could provide detailed information on the vertical velocity component and three-dimensional structure of vortex.

References

- [1] A. Towne, O. T. Schmidt, T. Colonius, Spectral proper orthogonal decomposition and its relationship to dynamic mode decomposition and resolvent analysis, *J. Fluid Mech* 847 (2018) 821-867.
- [2] L. Carassale, M. Marre-Brunenghi, Statistical analysis of wind-induced pressure fields: A methodological perspective, *J. Wind Eng. Ind. Aerodyn.* 99 (2011) 700–710.
- [3] L. Sirovich, Turbulence and the dynamics of coherent structures, *Quarterly of Applied Mathematics*, 45 (3) (1987), 561-590.

- [4] M. Sieber, C. O. Paschereit, K. Oberleithner, Spectral proper orthogonal decomposition, *J. Fluid Mech.* 792 (2016) 798-828.
- [5] P. J. Schmid, Dynamic mode decomposition of numerical and experimental data, *J. Fluid Mech.* 656 (2010) 5–28.
- [6] L. Carassale, M. Brunenghi, Identification of meaningful coherent structures in the wind-induced pressure on a prismatic body, *J. Wind Eng. Ind. Aerodyn.* 104–106 (2012) 216–226.
- [7] L. Carassale, Analysis of aerodynamic pressure measurements by dynamic coherent structures, *Probabilistic Engineering Mechanics* 28 (2012) 66–74.
- [8] X. Gilliam, J. P. Duniak, D. A. Smith, F. Wu, Using projection pursuit and proper orthogonal decomposition to identify independent flow mechanisms. *J. Wind Eng. Ind Aerodyn* 92 (2004) 53–69.
- [9] A. M. Edstrand, T. B. Davis, P. J. Schmid, K. Taira, L. N. Cattafesta, On the mechanism of trailing vortex wandering, *J. Fluid Mech.* (2016), vol. 801.

Appendix A

Xu and Hangan [1] presented a vortex model by combining a jet model with the modified Rankine vortex. A weighted combination of the following equations has been used for comparison:

$$U_r = \left(\frac{1}{z} + \frac{2r}{z^2} \right) e^{-\left(\frac{r}{z}\right)^2} - \frac{1}{r} \quad (\text{A.1})$$

$$U_z = \frac{2}{z} e^{-\left(\frac{r}{z}\right)^2} \quad (\text{A.2})$$

$$U_\theta = 2 S (r_c^2 + 1) \frac{r}{r_c^2 + r^2} \quad (\text{A.3})$$

Recently, Baker and Sterling [2] proposed the following model:

$$U_r = -\frac{4rz}{(1+r^2)(1+z^2)} \quad (\text{A.4})$$

$$U_z = \frac{4 \left(\frac{z_m}{r_m} \right) \ln(1+z^2)}{(1+r^2)^2} \quad (\text{A.5})$$

$$U_\theta = \frac{Kr^{\gamma-1} [\ln(1+z^2)]^{\gamma/2}}{(1+r^2)^{\gamma/2}} \quad (\text{A.6})$$

The velocity components are normalized by maximum radial velocity $U_{r,max}$. r and z are normalized r_m and z_m as the radius and height for which maximum radial velocity occurs. K and γ are empirical constants. Here, it is assumed $\gamma = 2$ and $K = 2 S / \ln(2)$, and $z_m / r_m = 1$.

Vatistas [3] proposed an empirical model for tangential velocity assuming that tangential velocity is only function of radius and vortex has solid-body rotation at the core:

$$U_\theta = \frac{U_{\theta,max} r}{(1+r^{2\beta})^{1/\beta}} \quad (\text{A.7})$$

$$U_r = -2(\beta + 1) \left(\frac{\nu_e}{r_c} \right) \frac{r^{2\beta-1}}{1+r^{2\beta}} \quad (\text{A.8})$$

$$U_z = 4\beta (\beta + 1) \left(\frac{\nu_e}{r_c} \right) (z) \frac{r^{2(\beta-1)}}{(1+r^{2\beta})^2} \quad (\text{A.9})$$

where $U_{\theta,max} = \Gamma / 2\pi r_c$ and β is a power-law index and assumed to be $\beta = 2$. ν_e is eddy viscosity (m^2/s). The radius (r) and height (z) are normalized by core radius (r_c).

Wood and White [4] modified the Vatistas model and proposed the following equation for tangential velocity:

$$U_{\theta} = \eta^{\lambda} U_{\theta,max} \frac{r^c}{(\eta - k + kr^{\lambda})^{\lambda}} \quad (\text{A.10})$$

where λ , η and k are empirical constants ($1 \leq k < \eta, \lambda > 0$) to control the tangential velocity profile. Here, it is assumed $\lambda = 1$, $\eta = 2$, and $k = 1.5$.

References

- [1] Z. Xu and H. Hangan, An Inviscid Solution for Modeling of Tornado-Like Vortices. *Journal of Applied Mechanics* 76 (2009) 03011-5.
- [2] C. J. Baker and M Sterling, Modelling wind fields and debris flight in tornadoes, *Journal of Wind Engineering and Industrial Aerodynamics* 168 (2017) 312-321.
- [3] G. H. Vatistas, V. Kozel, W. C. Mih, A simpler model for concentrated vortices. *Exp. Fluid* 11 (1991) 73–76.
- [4] V. T. Wood, L. W. White, A new parametric model of vortex tangential-wind profiles: development, testing and verification. *J. Atmos. Sci.* 68 (2011) 990–1006.

Curriculum Vitae

Name: Mohammad Karami

Post-secondary Persian Gulf University

Education and Bushehr, Iran

Degrees: 2005-2010 B.Sc.

Isfahan University of Technology

Isfahan, Iran

2010-2013 M.Sc.

The University of Western Ontario

London, Ontario, Canada

2015-2019 Ph.D.

Honours and

Awards: Graduate Research Assistant Fund ,2015-2019

Related Work Teaching Assistant

Experience The University of Western Ontario

2015-2019

Publications:

Journal papers

- **M. Karami**, E. Shirani, M. Jarrahi, H. Peerhossaini, “Mixing mechanisms by time dependent orbits in spatio-temporal chaotic advection”, Journal of Fluids Engineering Transactions of the ASME, FE DOI: 10.1115/1.4027588-2014 (8 Citations).

- **M. Karami**, E. Shirani, A. Avara, “Analysis of entropy generation, pumping power, and tube wall temperature in aqueous suspensions of alumina particles”, *Heat Transfer Research* (Begell house), V. 43, N. 4, pp. 327-342, 2012 (11 Citations).
- Z. Habibi, **M. Karami**, M. Jarrahi, E. Shirani, H. Peerhossaini, “Some observations on the spatiotemporal orbits structure and heat transfer enhancement in pulsating flow”, *International Journal of Thermal Science* (Elsevier) 125 (2018) 428-439.
- **M. Karami**, H. Hangan, L. Carassale, H. Peerhossaini, “Coherent structures in tornado-like vortices”, *Journal of Physics of Fluids* (2019), Selected as Editor’s Pick.
- **M. Karami**, H. Hangan, “Analytical model for tornado-like vortices: mean and fluctuating flow fields”, *Physics of Fluids* (2019), Under Review.
- **M. Karami**, L. Carassale, H. Hangan, “Statistical and modal analysis of surface pressure fluctuations in tornado-like vortices”, *JWEIA* (2019), Under Review.

Conference papers

- **M. Karami**, H. Hangan, L. Carassale, H. Peerhossaini, “Relationship between POD Modes and Physical Mechanisms in Tornado-Like Vortex”, CSME conference at Western University, 2019.
- **M. Karami**, L. Carassale, H. Hangan, M. Refan, “Coherent Structures of Tornado-Like Vortices”, ASME-FEDSM Conference 2018 in Montreal, Canada.
- C. Junayed, C. Jubayer, D. Parvu, D. Romanic, **M. Karami**, H. Hangan, “Parametric characterization of Downburst flows in WindEEE”, ASME-FEDSM Conference 2018 in Montreal, Canada.
- **M. Karami**, H. Hangan, L. Carassale, M. Refan, “An approximate model for large-scale fluctuations in tornado-like vortices”, In-Vento Conference 2018, Italy.
- **M. Karami**, L. Carassale, H. Hangan, H. Peerhossaini, M. Refan, “Internal Flow Structure of Vortex Breakdown”, 1000 Island Conference 2018, Canada
- **M. Karami**, H. Hangan, L. Carassale, H. Peerhossaini, M. Refan, “Mechanism of Wandering Phenomenon in Tornado-Like Vortices”, 1000 Island Conference 2018, Canada
- **M. Karami**, D. Romanic, M. Refan, H. Hangan, “Modeling of Tornado-Like Vortices”, 1000 Island Conference 2017, Canada

- Z. Habibi, **M. Karami**, E. Shirani, M. Jarrahi, H. Peerhossaini, “Heat Transfer Enhancement due to Chaotic Advection of Pulsating Flow in Twisted Duct”, Eurotherm 106, October 2016, Paris, France.
- **M. Karami**, M. Jarrahi, Z. Habibi, E. Shirani, H. Peerhossaini, “Heat transfer in a pulsating twisted-curved flow with constant wall temperature”, ASME 2014 (FEDSM & ICNMM), Illinois, USA (2 Citations).
- **M. Karami**, M. Jarrahi, E. Shirani, H. Peerhossaini, “Mixing enhancement in a chaotic micromixer using pulsating flow”, ASME 2014 (FEDSM & ICNMM), Illinois, USA. (2 Citations)
- A. Avara, **M. Karami**, “Energy and exergy efficiencies in agricultural and utility sectors of Iran compared with other countries”, ICMET Conference, Singapore, Sep. 2010 (5 Citations).